HAL
open science

Etude numérique de la dynamique de poches de cavitation sur une configuration de type Venturi

Camille Gouin

To cite this version:

Camille Gouin. Etude numérique de la dynamique de poches de cavitation sur une configuration de type Venturi. Mécanique des matériaux [physics.class-ph]. HESAM Université, 2021. Français. NNT : 2021HESAE075 . tel-03649094

HAL Id: tel-03649094

https://pastel.hal.science/tel-03649094v1

Submitted on 22 Apr 2022

HAL is a multi-disciplinary open access archive for the deposit and dissemination of scientific research documents, whether they are published or not. The documents may come from teaching and research institutions in France or abroad, or from public or private research centers.

L'archive ouverte pluridisciplinaire **HAL**, est destinée au dépôt et à la diffusion de documents scientifiques de niveau recherche, publiés ou non, émanant des établissements d'enseignement et de recherche français ou étrangers, des laboratoires publics ou privés.

HESAM UNIVERSITÉ

Arts et Métiers Sciences et Technologies

ÉCOLE DOCTORALE SCIENCES ET MÉTIERS DE L'INGÉNIEUR
[Laboratoire Dynfluid - Campus de Paris]

THÈSE

présentée par : **Camille GOUIN**
soutenue le : **20 Décembre 2021**

pour obtenir le grade de : **Docteur d'HESAM Université**

préparée à : **École Nationale Supérieure d'Arts et Métiers**
Spécialité : **Mécanique et Matériaux**

Numerical investigation of sheet cavitation dynamics on a Venturi configuration

THÈSE dirigée par :
[M. ROBINET Jean-Christophe]

et co-dirigée par :
[M. GONCALVES DA SILVA Eric]

Jury

M. Christophe CORRE	Professeur, ECL/LMFA	Président-Rapporteur
M. Matevž DULAR	Professor, University of Ljubljana	Rapporteur
M. Olivier COUTIER-DELGOSHA	Professor, Virginia Tech	Examinateur
M. Jean DECAIX	Assistant Professor, HES-SO Valais	Examinateur
Mme Henda DJERIDI	Professeure, INP Grenoble/LEGI	Examinatrice
M. Carlos JUNQUEIRA-JUNIOR	Ingénieur de recherche, ENSAM Paris	Examinateur
M. Jean-Christophe ROBINET	Professeur, ENSAM Paris	Directeur
M. Eric GONCALVES	Professeur, ENSMA/institut Pprime	Co-directeur

T H È S E

Résumé

Le présent manuscrit de thèse propose une étude de la dynamique de poche de cavitation par la réalisation de simulations numériques. La cavitation est un phénomène qui apparaît dans de nombreuses applications et peut entraîner des problèmes conséquents tels que la détérioration des matériaux, une baisse de rendements ou encore la génération de bruits. Un certain nombre de caractéristiques importantes de l'écoulement, telles que la topologie complexe de la poche de vapeur ainsi que sa dynamique, nécessitent d'être étudiées minutieusement. C'est pourquoi, la dynamique de l'écoulement cavitant, observée dans la géométrie d'un Venturi 3-D, et ses interactions avec les parois latérales sont étudiées numériquement. Dans un premier temps, une validation du code est proposée à partir de cas non-cavitant et cavitant. Puis, des simulations sont conduites en utilisant un solveur mono-fluide compressible de type RANS associé à un modèle non linéaire de turbulence ainsi qu'une équation de transport du taux de présence de la phase vapeur. Une analyse détaillée de l'écoulement cavitant est menée à partir d'outils innovants tels qu'une SPOD (*spectral proper orthogonal decomposition*). Une attention particulière est apportée à l'étude des effets tridimensionnels en comparant les résultats de calculs menés avec et sans parois latérales. Une dynamique tridimensionnelle de la poche de cavitation, non reliée à la présence de parois latérales, est identifiée. Son lien avec les mécanismes fondamentaux impliqués dans la cavitation par poche est discuté. Par la suite, plusieurs méthodes hybrides RANS/LES sont étudiées sur un cas non cavitant possédant une configuration se rapprochant de celle du Venturi. Cette étude a pour but de sélectionner la méthode hybride RANS/LES la plus adéquate à la simulation de la cavitation par poches.

Mots clés : cavitation, modèle RANS, modèle RANS/LES, mélange 1-fluide, écoulement compressible, SPOD

Abstract

The present PhD thesis aims at studying sheet cavitation dynamics by carrying out numerical simulations. This phenomenon appears in many hydraulic applications and can lead to technical issues, such as material degradations, performance reduction or noise generation. Some significant outcomes, such as the complex topology of three-dimensional cavitation pockets and their associated dynamics, need to be carefully visited. Therefore, the dynamics of partial cavitation developing in a 3-D Venturi geometry and the interaction with sidewalls are numerically investigated in the current work. In the first instance, software validation is proposed on non-cavitating and cavitating cases. Then, simulations are performed using a one-fluid compressible Reynolds-Averaged Navier–Stokes (RANS) solver associated with a non-linear turbulence model and a void ratio transport-equation model. A detailed analysis of this cavitating flow is carried out using innovative tools such as Spectral Proper Orthogonal Decompositions (SPOD). Particular attention is paid to the study of 3-D effects by comparing numerical results obtained with sidewalls and periodic conditions. A three-dimensional dynamics of the sheet cavitation, unrelated to the presence of sidewalls, is identified. The link between the mechanisms involved in sheet cavitation, such as the re-entrant jet and the vapour pocket behaviour, is discussed. The effects of the cavity dynamics on the flow are also identified. Thereafter, a range of Hybrid RANS/LES methods is investigated on a non-cavitating case with a similar configuration to the cavitating Venturi flow one. This study intends to select an acceptable hybrid RANS/LES method for sheet cavitation simulation using a better-resolved approach.

Keywords: cavitation, RANS model, RANS/LES model, 1-fluid mixture, compressible flow, SPOD

Contents

Résumé **3**

Abstract **5**

List of Tables **13**

List of Figures **19**

Introduction **21**

1 Context - State of the art **25**

1.1 Sheet cavitation in experimental studies 26

1.1.1 Sheet cavitation regime classification 27

1.1.2 Break off mechanisms 28

1.1.3 Cavity and re-entrant jet characteristics 31

1.1.4 3-D effects and re-entrant jet 32

1.1.5 Frequency analysis of sheet cavitation dynamics 33

1.1.6 Sheet cavitation effects on the flow and the surrounding area 35

1.2 Sheet cavitation in numerical works 36

1.2.1 One-fluid mixture and cavitation model 36

1.2.1.1 Homogeneous Equilibrium Model 36

1.2.1.2 Transport Equation Model 37

1.2.1.2.1 Models based on the Rayleigh Plesset equation 37
1.2.1.2.2 Models based on mixture pressure formulation 39
1.2.1.2.3 Models based on Gibbs free energy 40
1.2.1.2.4 Models based on the divergence of the velocity 40
1.2.1.2.5 Summary 41
1.2.2 Turbulence modelling 41
1.2.2.1 Inviscid 41
1.2.2.2 Reynolds-Averaged Navier Stokes (RANS) 41
1.2.2.3 Modified RANS 43
1.2.2.4 Large-Eddy Simulation (LES) 44
1.2.2.5 Hybrid RANS/LES 46
1.2.2.6 Summary 47

2 Governing equations **49**
2.1 The 1-fluid homogeneous approach 50
2.2 The compressible RANS equations 50
2.2.1 Mixture hypotheses 52
2.2.2 Turbulence modelling 52
2.2.2.1 Spalart-Allmaras model 53
2.2.2.2 $k - \ell$ of Smith model 53
2.2.2.3 Eddy viscosity correction 54
2.3 The hybrid RANS/LES equations 55
2.3.1 Delayed-Detached Eddy Simulation (DDES) 56
2.3.2 Definition of a $k - \ell$ DES model 57
2.3.3 Zonal Detached Eddy Simulation (ZDES) 59
2.3.3.1 ZDES type III 60

2.4 The four-equation cavitation model 61
2.4.1 Void ratio transport equation 61
2.4.2 Equations of state 62

3 Numerical strategy **65**
3.1 Numerical methods 65
3.1.1 System of equations 65
3.1.2 Time integration 67
3.1.2.1 Dual time-stepping integration 67
3.1.2.2 Global time-stepping 67
3.1.2.2.1 Explicit 68
3.1.2.2.2 Implicit 68
3.1.3 Spatial discretisation 68
3.1.3.1 Second order Jameson-Schmidt-Turkel 68
3.1.3.2 Third-order Jameson-Schmidt-Turkel 69
3.1.3.3 Dissipation modification of Jameson-Schmidt-Turkel schemes 69
3.1.4 Low Mach number preconditioning 70
3.1.5 Boundary conditions 71
3.1.5.1 Wall function 71
3.1.5.2 Inlet and outlet boundaries 72
3.1.5.2.1 Characteristic relations 72
3.1.5.3 Turbulent field 72
3.1.6 Source term 73
3.2 Software caviflow 73
3.2.1 Code development 73
3.2.2 Scalability study 74

3.3 Non-cavitating flow validation 76
3.3.1 RANS 2-D hump flow simulation 77
3.3.2 RANS 3D hump simulation 82
3.4 2-D cavitating flow study using RANS 84
3.4.1 Numerical centered scheme selection 84
3.4.2 Turbulence model selection 86

4 URANS simulation of a sheet cavitation flow within a 4° divergence angle Venturi configuration 89

4.1 Venturi configuration and comparison 89
4.1.1 Case set up 90
4.1.2 Comparison with experimental data 91
4.1.2.1 Velocity and void ratio profiles 91
4.1.2.2 Wall pressure profiles 93
4.2 Global behaviour 94
4.2.1 Time-averaged data analysis 94
4.2.2 Dynamic analysis 96
4.3 Re-entrant jet 102
4.4 Modal decomposition analysis 104
4.5 Discussion 109
4.6 Conclusion 111

5 Hybrid RANS/LES for sheet cavitation simulations 113

5.1 Hybrid RANS/LES method selection with NASA hump 114
5.1.1 Forcing hybrid formulation 114
5.1.2 DDES 115
5.1.3 DES $k - \ell$ 117

5.1.4 ZDES type III 118

5.1.5 Summary 120

5.2 Hybrid RANS/LES method for sheet cavitation flow within the venturi configuration . 121

5.2.1 Detached Eddy Simulation with $k - \ell$ 122

5.2.2 Delayed Detached-Eddy Simulation (DDES) 123

5.2.3 Zonal Detached-Eddy Simulation (ZDES) Type III 125

5.2.4 Summary 126

Conclusion **127**

5.3 Conclusion 127

5.4 Perspectives 129

Appendix **131**

Résumé des travaux de thèse **133**

Bibliography **151**

List of Tables

1.1 Dominant corrected Strouhal number St_σ extracted in sheet cavitation experimental studies. 34

1.2 Dominant Strouhal number St_∞ extracted in sheet cavitation experimental studies. . . 35

2.1 Coefficients of the Spalart-Allmaras model 53

2.2 Coefficients of the $k - \ell$ model 54

3.1 Butcher's table for SSPRK3 68

3.2 Weak stability study configuration. 74

3.3 Strong scalability study configuration. 76

3.4 Flow separation and reattachment location for the experimental and the 2-D numerical results. 78

4.1 Geometric dimensions. 90

4.2 Parameters of the cavitation model. 91

List of Figures

1 Pressure-temperature diagram (Goncalves, 2015) 22

1.1 Schematic description of a break off cycle by de Lange et al. (1994) de Lange *et al.* (1994). 29

1.2 Schematic description of a break off caused by two different mechanisms by Ganesh (2015) Ganesh (2015): the re-entrant jet at the left and the shock wave at the right. . 30

1.3 Schematic view, by de Lange and de Bruin (1997) de Lange & de Bruin (1997), of the velocity reflection generating the re-entrant jet. 33

3.1 Weak scalability study with 512000 cells per core. 75

3.2 Strong scalability study. 76

3.3 NASA hump mesh and geometry. 77

3.4 Visualisation of the streamwise velocity with a contour $u^* = 0$ for the computation using Spalart-Allmaras model. 78

3.5 Velocity profiles extracted at eight streamwise locations from the experiment, two computational results using the CFL3D software and the results of the current computation with Spalart-Allmaras. 79

3.6 Velocity profiles extracted at eight streamwise locations from the experiment, two computational results using the CFL3D software and the results of the current computation with $k - \ell$. 79

3.7 Velocity profiles extracted at eight streamwise locations from the experiment, two computational results using the CFL3D software and the results of the current computation with $k - \ell$ using the wall function. 80

3.8 Cp profile extracted along the streamwise axis from the experiment, two computational results using the CFL3D software and the results of the current computation with Spalart-Allmaras. 81

3.9 Cp profile extracted extracted along the streamwise axis from the experiment, two computational results using the CFL3D software and the results of the current computation with $k - \ell$. 81

3.10 Cp profile extracted along the streamwise axis from the experiment, two computational results using the CFL3D software and the results of the current computation with $k - \ell$ using the wall function. 82

3.11 Velocity profiles extracted at eight streamwise locations from the experiment, two computational results using the CFL3D software and the 3-D results of the current computation with $k - \ell$ using the wall function. 83

3.12 Cp profile extracted along the streamwise axis from the experiment, two computational results using the CFL3D software and the 3-D results of the current computation with $k - \ell$ using the wall function. 83

3.13 Time-averaged comparison between experiment at midspan and numerical 2-D results using second-order Jameson-Schmidt-Turkel (JST) scheme and third-order Jameson-Schmidt-Turkel (JST3) scheme for void ratio (left) and velocity (right) at stations S1 (top) and S2 (bottom). 85

3.14 Time-averaged comparison between experiment at midspan and numerical 2-D results using second-order Jameson-Schmidt-Turkel (JST) scheme and third-order Jameson-Schmidt-Turkel (JST3) scheme for void ratio (left) and velocity (right) at stations S3 (top) and S4 (bottom). 86

3.15 Time-averaged comparison between experiment at midspan and numerical 2-D results with $k - \ell$ and Spalart-Allmaras turbulence model for void ratio (left) and velocity (right) at stations S1 (top) and S2 (bottom). 87

3.16 Time-averaged comparison between experiment at midspan and numerical 2-D results with $k - \ell$ and Spalart-Allmaras turbulence model for void ratio (left) and velocity (right) at stations S3 (top) and S4 (bottom). 88

4.1 Schematic view of the Venturi used in the computation. 90

4.2 Mesh generation of the 3-D case represented with one visible mesh point out of three in the y and z directions. 90

4.3 Time-averaged comparison at midspan between experiment, 2-D, 3-D and 3-D periodic for void ratio (left) and velocity (right) at stations S1 (top) and S2 (bottom). 92

4.4 Time-averaged comparison at midspan between experiment, 2-D, 3-D and 3-D periodic for void ratio (left) and velocity (right) at stations S3 (top) and S4 (bottom). 93

4.5 Time-averaged comparison between experiment, 2-D, 3-D and 3-D periodic for wall pressure and wall pressure RMS over wall pressure. 94

4.6 Volume rendering of the time-averaged void ratio: (a) for the Venturi with sidewalls; (b) for the Venturi with side periodic boundary conditions 95

4.7 Volume rendering of the time-averaged streamwise velocity : (a) for the Venturi with sidewalls; (b) for the Venturi with side periodic boundary conditions 96

4.8 Time evolution of the attached cavity with snapshots separated by $\Delta t = 4.58\ 10^{-3}\ s$ with a volume rendering; (b)-(g) Snapshots extracted at different time represented in the void ratio signal (a). 97

4.9 Snapshot of the Q^* criterion contour of 0.5 with flow direction velocity u^* display compared to the vapour pocket positioning suggested by the $\alpha = 0.5$ contour (dark). 98

4.10 Volume rendering of the RMS fluctuation of the spanwise velocity v. 99

4.11 PSD maps along spanwise axis at $x^* = 0.64$ and at a vertical distance $z_p^* = 0.032$ from the bottom wall : (a) for the void ratio α; (b) for the spanwise velocity v. 99

4.12 PSD map for α along longitudinal axis at $y^* = L_y^*/4$ and at a vertical distance $z_p^* = 0.032$ from the bottom wall. 100

4.13 PSD maps for spanwise velocity v along longitudinal axis at a vertical distance $z_p^* = 0.032$ from the bottom wall : (a) at $y^* = L_y^*/8$; (b) at $y^* = L_y^*/2$. 100

4.14 Temporal evolution of the flow direction velocity u and the void ratio α at $x^* = 0.64$ along both sidewalls (one in red, the other in blue) for the case with sidewalls. 101

4.15 PSD maps of the periodic case along longitudinal axis at the mid-width and at a vertical distance $z_p^* = 0.032$ from the bottom wall : (a) for the void ratio α; (b) for the spanwise velocity v. 102

4.16 Dynamics of the re-entrant jet regarding the vapour cavity : (a) void ratio over time at $x^* = 0.8$ and $y^* = 3L_y^*/4$ for the case with sidewalls; (a)-(f): Snapshots with timestep $\Delta t = 4.58 \times 10^{-3} s$ of $\alpha = 0.5$ (purple) and $u^* = -0.1\ m.s^{-1}$ (yellow) contours. 103

4.17 Time evolution of the flow direction velocity u and the void ratio α at $x^* = 0.64$ and $y^* = L_y/4$ for the case with sidewalls. 104

4.18 SPOD spectrums representing energy gain over Strouhal number : (a) for the sidewalls case; (b) for the periodic case. The black to grey scale represents the most energetic mode to the less energetic one for each Strouhal number. 106

4.19 Volume rendering of the dominant mode of the SPOD for ρ at $St = 1.09$; $\rightarrow$: Time evolution behavior; (a) for the case with sidewalls; (b) for the case with periodic side boundaries. 107

4.20 Volume rendering of the dominant mode of the SPOD for u at $St = 1.09$; $\rightarrow$: Time evolution behaviour; (a) for the case with sidewalls; (b) for the case with periodic side boundaries. 108

4.21 Volume rendering of the dominant mode of the SPOD for v at $St = 1.09$; $\rightarrow$: Time evolution behaviour; (a) for the case with sidewalls; (b) for the case with periodic side boundaries. 108

4.22 Volume rendering of the dominant mode of the SPOD for w at $St = 1.09$; $\rightarrow$: Time evolution behaviour; (a) for the case with sidewalls; (b) for the case with periodic side boundaries. 108

5.1 Switch of the between the RANS (= 0) and the LES (= 1) areas for the DDES model on the midspan slice of 3-D NASA hump configuration. 115

5.2 Velocity profiles extracted at eight streamwise locations of the NASA hump from the experiment and DDES computation. 116

5.3 Velocity fluctuation profiles extracted at six streamwise locations of the NASA hump from the experiment and DDES computation. 117

5.4 Switch between the RANS (= 0), interface (= 1) and the LES (= 2) areas for the Type III ZDES model on the midspan slice of 3-D NASA hump configuration. 118

5.5 Velocity profiles extracted at eight streamwise locations of the NASA hump from the experiment and Type III ZDES computation. 119

5.6 Velocity fluctuation profiles extracted at six streamwise locations of the NASA hump from the experiment and Type III ZDES computation. 119

5.7 Snapshot of the turbulent viscosity over viscosity on the midspan slice of 3-D NASA hump configuration; (a) for the DDES model, (b) for the Type III ZDES model. . . . 120

5.8 Snapshot of the Venturi flow computed with the $k-\ell$ DES model. The 0.5 α contour is depicted in transparency and the midspan slice displays the switch between the RANS (= 0) and the LES (= 1) models. 122

5.9 Snapshot of the Venturi flow computed with the $k-\ell$ DES model. The 0.5 α contour is depicted in transparency and the midspan slice displays the streamwise velocity u^*. 123

5.10 Snapshot of the Venturi flow computed with the DDES model. The 0.5 α contour is depicted in transparency and the midspan slice displays the switch between the RANS (= 0) and the LES (= 1) models. 124

5.11 Snapshot of the Venturi flow computed with the DDES model. The 0.5 α contour is depicted in transparency and the midspan slice displays the streamwise velocity u^*. . . 124

5.12 Snapshot of the Venturi flow computed with the ZDES model. The 0.5 α contour is depicted in transparency and the midspan slice displays the switch between the RANS (= 0) and the LES (= 1) models. 125

5.13 Snapshot of the Venturi flow computed with the ZDES model. The 0.5 α contour is depicted in transparency and the midspan slice displays the streamwise velocity u^*. . . 126

14 Phénomène de la cavitation représenté sur un diagramme pression-température pour l'eau133

Introduction

The present PhD thesis was part of an ANR (Agence Nationale de la Recherche) project on the cavitating flow simulation using adapted numerical tools. The DynFluid laboratory hosted this research work in collaboration with the Pprime Institute.

Cavitation refers to a phase change from liquid to gas caused by a pressure fluctuation and assumed to be isothermal for cold water, as seen in the diagram of Fig. 1. In hydrodynamic, the increase of the velocity of a flow leads to a pressure decrease and, when it reaches a threshold called the saturation vapour pressure, a phase change is triggered. The single-phase flow is thus transformed to a two-phase flow in which properties linked to the phase change, such as the mass, momentum and energy transfers, are considered. Then, when a gas structure is exposed to higher pressure areas due to a flow advection or a velocity change, it caves in and returns to its liquid phase. The collapse can generate high-pressure waves, which could lead to detrimental effects on its surroundings. In some cases, the energy concentration of the bubble implosion is so high that it can even emit light. This phenomenon is called sonoluminescence.

The cavitation can be classified into several categories. The first type is the most common one, called bubble cavitation. It appears at cavitation inception, and the bubbles migrate into the flow without being regrouped between each other. Conversely, when the bubbles conglomerate, it forms another type of cavitation called sheet cavitation. The gas pocket is generally formed and attached along a wall. The third type of cavitation is shear cavitation which appears locally in shear layer areas. Finally, tip-vortex cavitation can be created in the wake of a foil tip where the pressure locally collapses and generates filaments of bubbles.

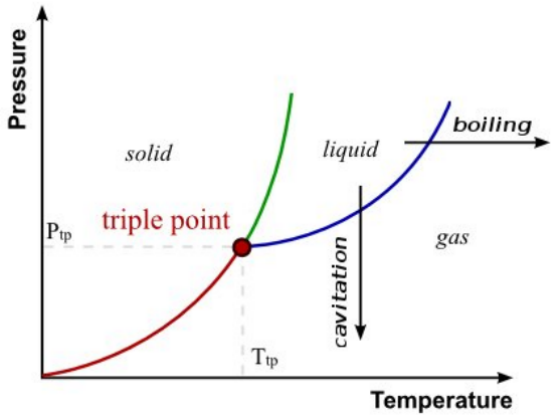

Figure 1: Pressure-temperature diagram (Goncalves, 2015)

Cavitation is usually observed in flows within pumps, valves, turbines or propellers. It causes significant damages or performance drops in many applications and some of them listed here:

- The bubble collapse creates both a liquid micro-jet and an intense water-hammer shock, which collide with walls and erodes the material,
- In turbomachinery, in addition to the performance drop, cavitation can lead to load change and vibration of the apparatus,
- Flow rate fluctuations can be observed through pumps or valves due to cavitation,
- The appearance of cavitation around submarine propellers generates noises and could reveal its location.

Nonetheless, cavitation can be set up intentionally in some applications. The erosion process can be controlled and deployed as a cleaning method. The supercavitation, which consists of creating a vapour pocket to cover en entire device, can be employed to reduce the drag of underwater bodies such as a torpedo. Cavitation is also triggered by ultrasound waves for medical purposes such as kidney stones destruction or cataract surgery. The interest in carrying out cavitation simulation is thus justified by the numerous applications where the phenomenon occurs.

The present work focuses on the sheet cavitation phenomenon, which is usually observed along with foils or venturis. A vapour pocket is formed and is attached around the leading edge. The cavity

presents an unsteady behaviour, and the dynamics depend on many parameters such as the incidence angle, the inflow velocity or the geometry. In some configurations, the flow dynamics can lead to the shedding of vapour structures into the flow. The formation of such vapour pockets has a significant impact on the flow downstream and on the material.

Cavitation modelling is a major issue to understand and control the phenomenon. The complexity of cavitation leads to difficulties to build models consistent with all the physical behaviour observed in multiple applications. In addition to the two-phase flow simulation, the phase change has to be considered with the mass transfer and thermodynamic effects. Moreover, the speed of the sound variation during the phase change leads to the presence of a large range of Mach number and compressible effects into the flow. Shock waves, created by the collapse of the gas structures, are also identified in the two-phase flow. Therefore, the generation of software built with an adequate cavitation model is a challenging perspective.

The current manuscript is structured in several points, from state of the art to dynamics analysis of numerical results of sheet cavitation simulations. First, the context of the study is introduced with experimental observations and the description of the phenomenon. It is followed by a review of the main numerical works depending on the selected cavitation model and the turbulence modelling. Then, the governing equations are built depending on key assumptions, such as considering the two-phase flow as a mixture flow. The choice of the cavitation and turbulence models are justified in the chapter. Thereafter, the in-house software formulation is described in detail and, a validation based on non-cavitating and cavitating flows is proposed to evaluate the software development. Furthermore, a study of quasi-stable cavity dynamics observed in a flow within a Venturi configuration is carried out. Numerical results are compared with experimental data, and dynamic analyses are performed to identify any dominant mechanisms within the flow. To that end, Power Spectral Density maps or Spectral Proper Orthogonal Decomposition are computed and analysed. Lastly, the use of Hybrid RANS/LES methods is investigated to determine such methods' contribution to sheet cavitation flow simulations.

Chapter 1

Context - State of the art

Contents

1.1 Sheet cavitation in experimental studies 26
1.1.1 Sheet cavitation regime classification 27
1.1.2 Break off mechanisms 28
1.1.3 Cavity and re-entrant jet characteristics 31
1.1.4 3-D effects and re-entrant jet 32
1.1.5 Frequency analysis of sheet cavitation dynamics 33
1.1.6 Sheet cavitation effects on the flow and the surrounding area 35
1.2 Sheet cavitation in numerical works 36
1.2.1 One-fluid mixture and cavitation model 36
1.2.2 Turbulence modelling 41

Before presenting a review of sheet cavitation observations in experimental and numerical studies, a non-dimensional parameter called the cavitation number σ, has to be introduced to describe cavitating flows :

$$\sigma = \frac{p - P_{vap}(T)}{0.5\rho u^2}, \tag{1.1}$$

where P_{vap} stands for the vaporisation pressure, ρ the density and u the velocity of the considering mixture. The pressure p could be selected as the inlet pressure or another characteristic pressure of the flow. The cavitation number is then used to characterize different cavitation regimes.

Two different classes of cavitation appear in low-pressure areas along walls. The first one is the bubble cavitation which consists of the formations of vapour bubbles growing in the low-pressure area and collapsing when flowing in higher pressure areas. The second one is a class of large scale cavitation structures called sheet cavitation which occurs when a wake or region of separated flow is filled

with vapour. The onset condition of the bubble or the sheet cavitation is led by flow and geometry configurations. The current section is devoted to the study of sheet cavitation.

1.1 Sheet cavitation in experimental studies

Sheet cavitation is split into two different types of cavitation: the partial cavitation in which the cavity is attached to the wall at its closure and the supercavitation in which the aft of the cavity is closed downstream the trailing edge of the corresponding geometry (Brennen, 1995). Partial cavitation is also characterised by various cavity behaviours. Therefore, Laberteaux & Ceccio (2001) defined two main class of cavities: closed or quasi-stable cavity and open or cloud cavity. The first one is identified by a vapour pocket which keeps a constant or quasi-constant length with no or little sheddings of vapour structures into the flow. The other one is described by an oscillating cavity length with greater vapour structures shedding. Knapp (1955) noticed, in his experiment on a body with hemispherical nose, the presence of a re-entrant jet which is described later by Kawanami *et al.* (1997) as a flow of water, from downstream to upstream, under a fully developed cavity. de Lange (1996) highlighted the re-entrant jet in both cloud and quasi-stable cavitation. However, Gopalan & Katz (2000) suggested that a re-entrant jet is developed only if an adverse pressure gradient is identified. The influence of the pressure gradient on dynamics and the triggering of the re-entrant jet is verified in numerous experimental studies (Laberteaux & Ceccio, 2001; Callenaere *et al.*, 2001; Jahangir *et al.*, 2018; Ganesh, 2015). Another information about the flow around the cavity is that the velocity at the upper interface is parallel to the interface (Foeth *et al.*, 2006). Furthermore, partial cavitation is responsible for unsteady wall pressure, as highlighted by Arndt *et al.* (2000), and even for the formation of pressure waves propagated toward the surrounding area due to the collapse of vapour structures shed and advected by the flow (Stanley *et al.*, 2014; Ganesh, 2015; Jahangir *et al.*, 2018). It is known that the speed of the sound is dropped around phase-change areas (Wallis, 1967) as confirmed by the study of Jahangir *et al.* (2018) on a converging-diverging nozzle which raised a shock velocity of 15 $m.s^{-1}$ into the vapour pocket.

1.1.1 Sheet cavitation regime classification

As previously introduced, sheet cavitation is decomposed in different regimes. The present section proposes a classification and a description associated with each regime regarding observations of experimental studies in the literature. Nonetheless, the boundaries between all the regimes are not clear and highly depending on the cavitation number and the incidence angle variations. First, Le *et al.* (1993*a*) noticed that sheet cavitation regimes are connected to cavity thickness and re-entrant jet development. Thin cavities are associated with weak re-entrant jet and little or no shedding, which corresponds to quasi-stable cavities (Callenaere *et al.*, 2001; Barre *et al.*, 2009; Liu *et al.*, 2020). In this regime, a U-shape of the cavity can be observed (de Lange *et al.*, 1994) due to little sheddings localised only around the midspan. Moreover, as described by de Lange (1996), the rather low velocity of the re-entrant jet leads to the creation of a stagnant layer which causes irregular little shedding of the rear part of the cavity. Similarly, Liu *et al.* (2020) observed cavities within venturi flows with aperiodic tail shedding of less than 30% of the maximum cavity length. The authors also measured the presence of small-intensity pressure waves in the flow.

The cloud cavitation is defined by a thicker cavity and a stronger re-entrant jet as shown by Dular *et al.* (2012) in venturi configurations for which the re-entrant jet velocity for a quasi-stable cavity is estimated to only 60% of the one for cloud cavitation. Furthermore, cloud cavitation is usually linked to a periodic break off of the vapour cavity. Other characteristics are related to cloud cavitation, for example, Coutier-Delgosha *et al.* (2006) noticed a relatively low maximum value of volume fraction of vapour phase in the cavity, around 0.3. During the process, the cavity keeps a quasi constant thickness (Aeschlimann *et al.*, 2013) and a liquid sublayer is always observed (Stanley *et al.*, 2014). High-intensity pressure waves are presents in cloud cavitation (Liu *et al.*, 2020) and play an important role, with the re-entrant jet, in the break off process.

Several studies focused on the conditions of appearance of the different regimes regarding the cavitation number σ. First, Watanabe *et al.* (2001) observed, based on several experimental studies on hydrofoils, that if the cavitation number decreases, the partial cavitation tend to become supercavitation with an increase of the unsteadiness. Later, Brandner *et al.* (2010), from an experimental study

on a cavitating sphere, introduced two modes into the partial cavitation part. For high cavitation number, the inception mode represents the first development of the cavity with little shedding. For intermediate cavitation number, the shedding mode describes the break-off process with a significant influence of the re-entrant jet. Stanley *et al.* (2011) or Ganesh (2015), through flow studies within a cylindrical orifice and a venturi, specified the shedding mode definition by splitting it into a transitory or intermittent shedding part and a break off part. This new classification provides a better overview of the phenomenon regarding the cavitation number. The transitory mode includes cavities with aperiodic sheddings that tend to become periodic by decreasing the cavitation number. Dular *et al.* (2012) identified this transition through the periodicity of the re-entrant jet with irregular sheddings. The break off part represents the periodic streamwise oscillation of the cavity with sheddings of large cloud structures. Following, Liu *et al.* (2020) proposed to split the break off mode, and probably a part of the transitory mode, into three parts depending on the ratio of the shedding position over the maximum cavity length. Tail shedding is defined as a vapour release of less than 30% of the cavity. The release of 30% to 70% of vapour content from the cavity is called central shedding. Finally, the front shedding is represented by a vapour release of more than 70% of the cavity. These three modes appeared in this order by decreasing the cavitation number σ or increasing the incidence angle. However, for low incidence angle, only the tail shedding is observed as for high angle where only central or front sheddings are detected.

1.1.2 Break off mechanisms

The break off regime represents an important part of the sheet cavitation and requires precision on the different mechanisms influencing the process. From the first description of the break off cycle by Knapp (1955), many authors suggested the influence of the re-entrant jet in the process (Le *et al.*, 1993*a*; de Lange *et al.*, 1994; Stutz & Reboud, 1997). Others minimised the part of the re-entrant jet in the triggering of the break off. For example, Avellan & Dupont (1988) suggested, regarding their experimental results on a hydrofoil, that interface instabilities and turbulence transition cause the break off. Nevertheless, Kawanami *et al.* (1997) studied the influence of the re-entrant jet on the break off by putting an obstacle along the wall. The re-entrant jet is then stopped and the break off inhibited. It proves the major importance of the re-entrant jet on the shedding. In most study

as in de Lange *et al.* (1994) or Stutz & Reboud (1997), the break off is described as represented in Fig. 1.1. First, the cavity grows from the leading edge or a small length and reach its maximum size. From this point, a re-entrant jet is formed at the closure of the cavity and grows toward the leading edge. Once the re-entrant jet reaches the vicinity of the leading edge, it moves upwards and collides with the upper interface of the cavity. The rear part of the cavity is then shed and advected downstream. Kubota *et al.* (1989) measured, on a flow over a hydrofoil, that the velocity of advection of the vapour cloud is slower than the flow velocity but it accelerates and slightly goes upward when moving downstream. Furthermore, several experimental studies identified flow vapour structures as stretched vortex like a croissant (Avellan & Dupont, 1988; Kubota *et al.*, 1989) or hairpins (Gopalan & Katz, 2000). Vorticity production caused by the re-entrant jet (Le *et al.*, 1993*a*) or cloud collapse (Gopalan & Katz, 2000) is also detected.

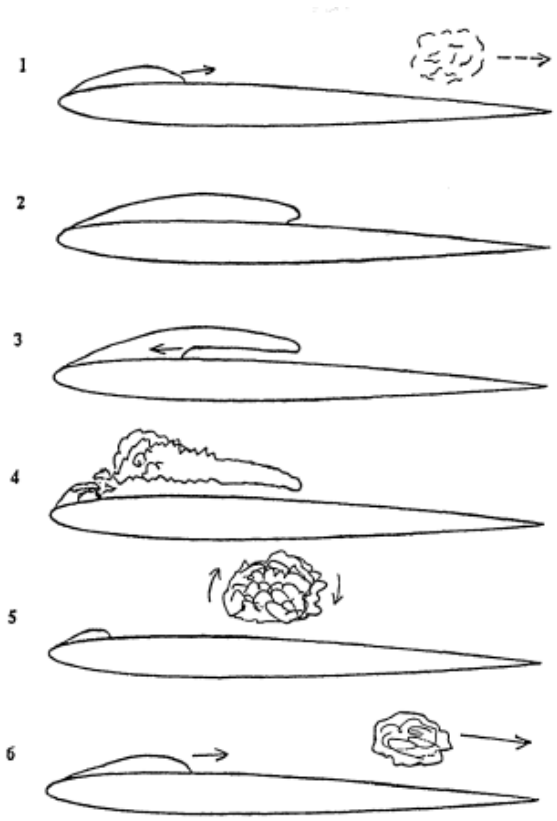

Figure 1.1: Schematic description of a break off cycle by de Lange et al. (1994) de Lange *et al.* (1994).

Later, the role of pressure waves is investigated. Arndt *et al.* (2000) proposed to identify two mechanisms using the parameter $\sigma/2\alpha_i$, where α_i is the incidence angle. Below $\sigma/2\alpha_i = 4$, the re-entrant jet mechanism is supposed to be dominant and, above this threshold, the authors consider that the pressure pulses are the dominant mechanism. Hayashi & Sato (2014), in their work on an axisymmetric converging-diverging nozzle configuration, suggested that the formation of pressure waves during the collapse is linked to the creation of the re-entrant jet. Simultaneously, Stanley *et al.* (2014) studied a flow within a cavitating cylindrical orifice and observed that the re-entrant jet velocity is slower than the velocity of the mechanism driving the break off. Thus, the authors suggested that the break off is caused by travelling pressure waves generated by cloud collapse. This conclusion is confirmed by Ganesh (2015) in an experimental study of venturi flow with an obstacle located at one-third of the cavity length to stop the re-entrant jet. The results showed that the break off is this time not inhibited and thus the mechanism responsible for the break off is not the re-entrant jet. Then, the author identified shock waves propagated upstream as the mechanism causing the break off. Nonetheless, the shock waves are set as a driving mechanism as well as the re-entrant jet: both mechanisms, as shown in Fig. 1.2, are observed depending on the flow configuration.

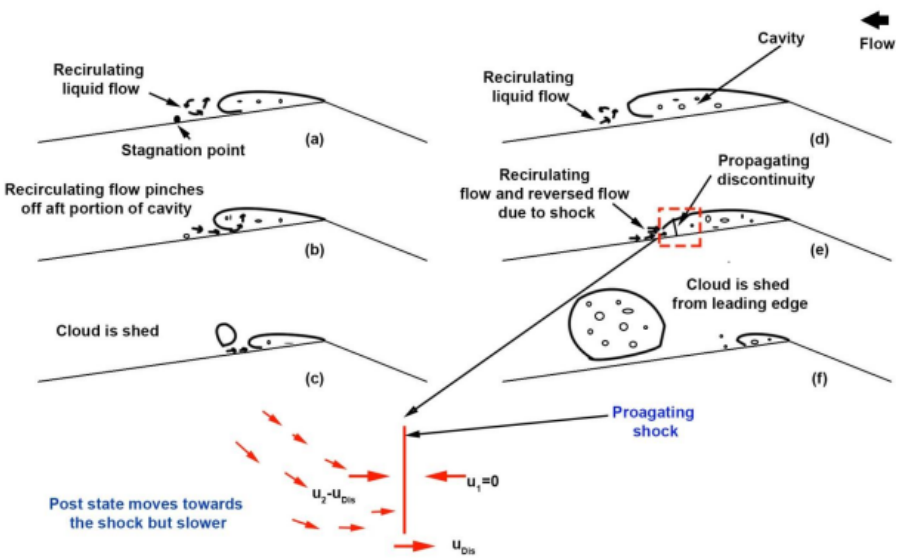

Figure 1.2: Schematic description of a break off caused by two different mechanisms by Ganesh (2015) Ganesh (2015): the re-entrant jet at the left and the shock wave at the right.

Thereafter, investigations are carried out to identify the onset condition of both mechanisms and

highlight the main differences. Ganesh *et al.* (2016) observed a faster growth of the cavity for the shock induced break off than for the re-entrant jet induced one. Moreover, the authors noticed that if the flow stream velocity increases, the shock speed also increases but the maximum mean value of the volume fraction of vapour and the Strouhal number of the oscillation remain constant. The increase of the shock speed is linked to the drop of the speed of the sound velocity. Jahangir *et al.* (2018) proposed a classification of both mechanisms regarding the cavitation number based on an experimental study of a flow within a converging-diverging nozzle configuration. The authors detected that the shock wave induced break off corresponds to a lower cavitation number than the re-entrant jet one. In addition, an interval of cavitation number where both mechanisms are involved in the break off is identified. The shock induced shedding cycle presents a larger cavity length than the re-entrant jet one. In this paper, the re-entrant jet shedding is characterised by the existence of a stagnation point around the cavity closure. In another experimental study on a flow over a hydrofoil, Wu *et al.* (2019) gave another description of the transition between both sheddings from high to low cavitation number:

- a stable cavity begins to shed by the re-entrant jet pinching off the rear part of the cavity,
- cavity length is larger and sheds from the leading edge (re-entrant jet induced),
- pressure pulses from collapse begin to influence the cavity growth and sometimes stop it (one max growth out of two or three),
- propagating bubbly shock waves leads the break off and can interfere with the shedding frequency.

Recently, Pipp *et al.* (2021) and Podbevsek *et al.* (2021) observed a third mechanism inducing the break off. The authors detected, in micro-scale configurations, that the break off is triggered by the appearance of Kelvin-Helmholtz instabilities around the cavity interface. This information could be linked to the previous analysis of Avellan & Dupont (1988). The break off is thus, at present, a complex mechanism that stays, besides all the recent progress, an open thematic to investigate.

1.1.3 Cavity and re-entrant jet characteristics

The cavity and the re-entrant jet present different characteristics depending on the sheet cavitation regime or the influence of external factors. This section gives a non-exhaustive list of physical behaviours, extracted from various experimental observations, to help to correctly understand this

complex phenomenon. First, the cavity shape is affected by numerous external parameters. The cavity length increases if the cavitation number or the incidence angle decreases (Stanley *et al.*, 2011; Liu *et al.*, 2020). The wall surface effects on the cavity development are also observed by Kawakami *et al.* (2008), particularly on the cavitation inception. Recently, Ge *et al.* (2021) observed that a temperature increase of the water up to 55^oC lead to an expansion of the vapour pocket, and, above this threshold, leads back to a decrease. Concerning the stabilisation of the cavity, Sun *et al.* (2019*b*), noticed that the addition of a ventilation rate improves the dynamic stability of the cavity. Dular *et al.* (2012) proved, based on a study on flows within different venturi configurations, that the scale had a particular effect on dynamics. For example, for venturi configuration with a small height, the shedding is not observed even if such shedding is detected on flow within the same geometry with a greater height. Moreover, other effects, such as the gas content in the liquid, influence the shedding frequency of the cavity. Kawakami *et al.* (2008) showed that a decrease of half of the gas content double the shedding frequency.

The behaviour of the re-entrant jet and its velocity measurement depending on the sheet cavitation regime is a complicated topic. The experimental methods gave at first approximate results. Some authors even suggested that the re-entrant jet was of the same magnitude that the stream velocity (de Lange *et al.*, 1994; Kawanami *et al.*, 1997) or equal to nine-tenths of the stream velocity (Le *et al.*, 1993*b*). Stutz & Reboud (1997) suggested that the cloud collapse causes an increase of re-entrant jet velocity. Later, Callenaere *et al.* (2001) extracted, from a cloud cavitation flow within a diverging step, a re-entrant jet velocity of the half of the stream velocity. This information is confirmed by the experimental study on a converging-diverging nozzle led by Hayashi & Sato (2014). Callenaere et al. also estimated the re-entrant jet velocity, linked to a quasi-stable cavity, at three-tenths of the stream velocity. Nevertheless, it has to be noticed that the re-entrant jet velocity seemed to be dependent on the studied geometry and the estimate values have to be taken carefully.

1.1.4 3-D effects and re-entrant jet

The investigation of any 3-D effects linked to the re-entrant jet dynamics is essential to improve the understanding of cavitating flows. In the study of a flow within a hydrofoil, de Lange *et al.* (1994) identified a spanwise component of the re-entrant jet in the quasi-stable cavity regime. Further investigations of de Lange & de Bruin (1997) and Dular *et al.* (2007) confirmed that the re-entrant jet

has a spanwise component if the cavity closure line is inclined. As shown in Fig. 1.3, the re-entrant jet seems to be reflected by the cavity interface, which gives its spanwise component. Moreover, Dular *et al.* (2012) observed, on a venturi configuration, that when the re-entrant jet does not reach the upper interface of the cavity and trigger the middle shedding, it turns to a side and triggers a side shedding in only $25 - 40\%$ of the time. For the rest of the time, the re-entrant jet oscillates. Later, Timoshevskiy *et al.* (2016) detected an alternating shedding from one side to another into a flow over a guide vane. The authors suggested the existence of an oblique mode of sheet cavity oscillation associated with spanwise instabilities. At the same time, Prothin *et al.* (2016) performed a Dynamic Mode Decomposition (DMD) analysis on the results of an experimental study of a flow over a hydrofoil. 3-D effects due to re-entrant jet instability or shock wave are then detected. The authors suggested a link with small-scale structures propagating orthogonally to the flow. It has to be noticed that in other configurations, such as the experimental investigation of Che *et al.* (2019), symmetrically side-entrant jets are detected and influence the cloud shedding when both jets collide. Hence, several experimental investigations highlighted 3-D effects of cavitating flows associate with a spanwise re-entrant jet component and sometimes spanwise oscillations.

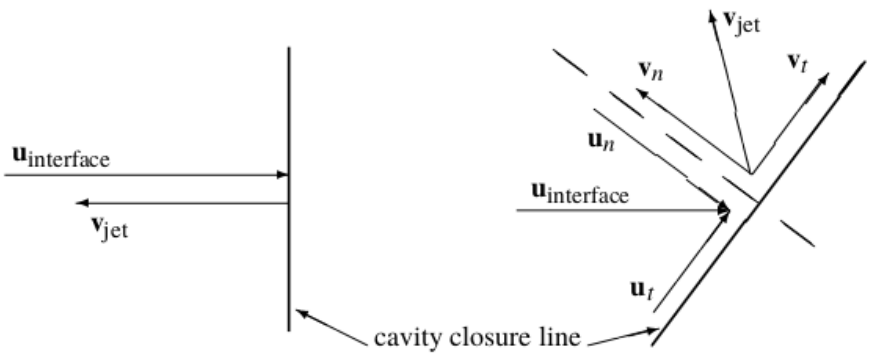

Figure 1.3: Schematic view, by de Lange and de Bruin (1997) de Lange & de Bruin (1997), of the velocity reflection generating the re-entrant jet.

1.1.5 Frequency analysis of sheet cavitation dynamics

The current section is devoted to the frequency analysis of cavitating flows in experimental works. To this end, a Strouhal number has to be defined to compare the results of diverse configurations and to identify the flow mechanisms responsible for dynamics. Dular & Bachert (2009) summarized

previous experimental studies on cavitating hydrofoils and proposed a Strouhal number definition to unify the analysis. The Strouhal number is described as a ratio between the extracted frequency and a characteristic frequency f_{char} based on a characteristic velocity and a characteristic length:

$$f_{char} = \frac{u_{char}}{L_{char}}. \tag{1.2}$$

The selection of the characteristic length is discussed and the choice of a length scale based on the geometry is excluded due to the indirect link with the sheet cavitation phenomenon. The mean cavity length and the mean maximum attached cavity length L_c seem to be better alternatives for the length scale definition. The selection of the characteristic velocity, regarding previous works, is more uncertain. Dular et al. highlighted that the best choice could be the velocity of the re-entrant jet at the cavity interface. However, the measurement of this velocity in an experimental study is intricated. Therefore, to approximate this velocity, several works proposed to use a corrected free stream velocity $u_\sigma = u_\infty\sqrt{1+\sigma}$. Hence, the authors proposed to use the corrected Strouhal number St_σ:

$$St_\sigma = \frac{L_c f}{u_\infty\sqrt{1+\sigma}}. \tag{1.3}$$

Some studies, as the one carried out on a diverging step by Callenaere *et al.* (2001), proved that this definition is not justified to generally approximate the re-entrant jet velocity. Table 1.1 shows the dominant corrected Strouhal number St_σ extracted from experimental studies.

References	**St$_\sigma$**
de Lange & de Bruin (1997)	0.18
Laberteaux & Ceccio (2001)	0.2
Che *et al.* (2019)	0.2

Table 1.1: Dominant corrected Strouhal number St_σ extracted in sheet cavitation experimental studies.

Nonetheless, the majority of the Strouhal numbers defined in experimental investigations used the free stream velocity as characteristic velocity. The Strouhal number is then defined as:

$$St_\infty = \frac{L_c f}{u_\infty}. \tag{1.4}$$

Table 1.2 presents the dominant Strouhal number St_∞ extracted in the literature.

References	**St$_\infty$**
Le *et al.* (1993*a*)	0.28
de Lange *et al.* (1994)	0.3
de Lange & de Bruin (1997)	0.29
Callenaere *et al.* (2001)	0.2
Coutier-Delgosha *et al.* (2006)	0.25
Foeth *et al.* (2006)	0.19
Ganesh (2015)	0.25-0.3
Prothin *et al.* (2016)	0.15 / 0.25 / 0.33
Jahangir *et al.* (2018)	0.2-0.4
Ge *et al.* (2021)	0.17-0.22

Table 1.2: Dominant Strouhal number St_∞ extracted in sheet cavitation experimental studies.

The more recent experimental analyses highlighted a fluctuation of the Strouhal number depending on the cavitation number and the configuration. A closer investigation in the selection of the characteristic variables could be carried out to improve the understanding of the underlying mechanism.

1.1.6 Sheet cavitation effects on the flow and the surrounding area

The main issues of the formation of sheet cavitation are the pressure load, vibrations, noise, performance decrease or erosion. Knapp (1955) identified damages caused by pressure pulse around the cavity area. Later, Reisman *et al.* (1998) confirmed this observation and linked the damages to bubbly shock waves. Le *et al.* (1993*b*) highlighted that erosion is worst in cloud cavitation flow than quasi-stable cavity flow. Moreover, in the cloud cavitation regime, Liu *et al.* (2020) observed periodicity in the wall static pressure fluctuation. It shows the link between cloud shedding and high-intensity pressure waves. Another problem commonly identified in cavitation is the noise production, as observed by de Lange (1996).

Further experimental studies, as the one carried out by Brandner *et al.* (2010), underlined the acceleration of the transition to turbulence induced by sheet cavitation. Laminar cells are initially observed around the leading edge, where the cavity is attached, and are destabilized by Kelvin-Helmholtz instabilities in the overlying layer which trigger the transition. Furthermore, the authors observed in the flow over a sphere, that vortex shedding occurs at a lower Reynolds number in cavitating flow than in single-phase flow.

1.2 Sheet cavitation in numerical works

There are several ways to simulate two-phase flows. The choice of a two-fluid model, in the case of sheet cavitation simulation, can lead to unaffordable computational costs and difficulties related to the interface tracking with the creation and the destruction of vapour pockets or the transfer terms computation due to the phase change. Therefore, a one-fluid homogeneous approach is generally selected for computation. The current section is devoted to present an overview of cavitation models and turbulence models used in numerical works based on a one-fluid mixture method. Various cavitating flow simulations are presented in the following. A particular emphasis is laid on flow within venturi geometries.

1.2.1 One-fluid mixture and cavitation model

The one-fluid homogeneous approach, selected in many studies, imposes hypothesis over thermodynamic and kinematic equilibrium between the liquid and vapour phases (Merkle *et al.*, 1998). The flow is considered as a mixture and the phases are assumed to share the same pressure, velocity and temperature. In some numerical studies, a non-condensable gas is even considered in addition to the vapour and liquid phases. Furthermore, two main families are often used: the Homogeneous Equilibrium Model (HEM) and the Transport Equation Model (TEM) or Homogeneous Relaxation Model (HRM). The present section gives an outline of the ensuing cavitation models.

1.2.1.1 Homogeneous Equilibrium Model

The HEM is composed of classical conservative equations with a suitable equation of state for the liquid-vapour mixture. These models defined the volume fraction of the vapour phase using the mixture density and the mass fluxes are not explicitly computed but depended on the state law shape. Therefore, the selection of the equation of state and some parameters, such as the minimum speed of the sound c_{min}, highly impacts the description of the phase change areas.

Arndt *et al.* (2000) defined a barotropic equation of state which is linear in the liquid phase and non-linear below a pressure threshold. Coutier-Delgosha *et al.* (2003, 2007) selected a barotropic equation of state joining the Tait equation for the liquid phase and the perfect gas equation for vapour.

The connection is controlled by the definition of the minimum speed of the sound. Other close models are defined by Chen *et al.* (2006) or also Schnerr *et al.* (2008). In the last one, the connection between the perfect gas and the Tait equation is described by a system of equations based on the Clausius–Clapeyron relation and a convex combination of the saturation densities of both phases. A similar system is solved in the work of Budich *et al.* (2018) and Trummler *et al.* (2020, 2021). In the work of Goncalves & Patella (2009), Goncalvès & Decaix (2012) and Decaix & Goncalves (2013), pure phases are described by the stiffened gas equation of state and linked by a sinusoidal barotropic equation using the minimum speed of the sound as a parameter. Another example of the use of HEM is the work of Hickel *et al.* (2011) in which the equation of state corresponds to a modified Tait equation.

Nevertheless, difficulties to compute high-velocity flows in the two-phase area and the underestimation of the mass flow rate for HEM are highlighted by Downar-Zapolski *et al.* (1996).

1.2.1.2 Transport Equation Model

The TEM is composed of classical conservative equations coupled with a transport equation for the void ratio or volum fraction of vapour. This method is the most represented one in the literature. The main difference between these cavitation models occurs in the choice of the source term including the modelling of the mass transfer. Its formulation is mostly based on the Rayleigh Plesset equation, on the mixture pressure, on Gibbs free energy or on the divergence of the velocity. A non-exhaustive list of the different expression is presented below.

1.2.1.2.1 Models based on the Rayleigh Plesset equation The source term of the transport equation is built using an approach based on the Rayleigh-Plesset equation. This equation describes the dynamic evolution of a spherical bubble in a liquid. In the present models, a link is created between the vapour cloud dynamics and the bubble dynamics. The vapour cloud dynamics is then computed using the mixture pressure, as shown in the equation below:

$$\left|\frac{\partial R}{\partial t}\right| \approx \sqrt{\frac{2}{3}\frac{|P_{vap} - p_m|}{\rho_l}}, \tag{1.5}$$

where $\left|\frac{\partial R}{\partial t}\right|$ represents the radius evolution of a bubble. In the following models, the mass transfer is considered as proportionnal to the radius evolution.

- Schnerr & Sauer (2001) proposed a model where the void ratio α is linked to the bubble radius R:

$$\alpha = \frac{V_{vap}}{V_{vap} + V_{liq}} = \frac{n_0 \frac{4}{3}\pi R^3}{1 + n_0 \frac{4}{3}\pi R^3} \tag{1.6}$$

  Moreover, a vapour bubble density n_0 has to be selected by the user to complete the model. The mass transfer is then estimated by developing the void ratio transport equation using Eq.(1.6). The model is also used in the study of Ji *et al.* (2013*a*) and more recently of Cheng *et al.* (2019), Kadivar *et al.* (2019), Arabnejad *et al.* (2019) and Sun *et al.* (2020).

- Singhal *et al.* (2002) developed another model in which a non-condensable gas is considered in addition to vapour and liquid. A formula depending on the phase mass fractions and two adaptable constants is used, based on the Rayleigh-Plesset equation. A pressure threshold, corresponding to the vaporisation pressure, is established to compute the mass transfer term. Nevertheless, Ducoin et al. (2012) Ducoin *et al.* (2012) observed in a comparative study of cavitation models, that this model does not show the best agreement with experimental data on the computation of a flow around a hydrofoil. Later, Dittakavi *et al.* (2010), Park & Rhee (2013) and Egerer *et al.* (2014) also used the current model.

- The model created by Zwart *et al.* (2004) is one of the most commonly used cavitation models due to its implementation into ANSYS softwares. Again, a pressure threshold is set up to differentiate the vaporisation and condensation in the mass flow rate. This term is then calculated based on the selection of the radius of a nucleation site, the nucleation site volume fraction and two empirical constants. However, the model is used under the assumption of no bubbles interactions in the vaporisation state. The Zwart model is used in the literature by Huang *et al.* (2014), Peng *et al.* (2016), Sedlar *et al.* (2016), Geng & Escaler (2018), Long *et al.* (2018), Chen *et al.* (2019) and Hidalgo *et al.* (2019).

As specified in the work of Coutier-Delgosha *et al.* (2007), the Rayleigh-Plesset equation is built to describe the radius evolution of a single spherical bubble in a pressure field. This description does not agree with the evolution of a vapour cloud which is composed of many vapour bubbles interacting with each other and do not remain spherical.

1.2.1.2.2 Models based on mixture pressure formulation Another way to build the source term of the transport equation is based on the kinetic theory of gas. Theoretical works with perfect gas hypothesis combined with experimental observations led to the formulation of the Hertz-Knudsen equation for the mass transfer:

$$\dot{m} = \frac{\sigma_e}{\sqrt{2\pi r_e}} \left(\frac{P_{vap}(T_l)}{\sqrt{T_l}} - \frac{p_v(T_v)}{\sqrt{T_v}} \right), \tag{1.7}$$

where r_e stands for the water gas constant and σ_e for the evaporation coefficient (empiric). The following models describe the mass transfer using a similar formula. The formulation of the temperature is sometimes neglected due to a thermal equilibrium hypothesis during the phase change. However, a relaxation time, representing the thermodynamic equilibrium time, can be used.

- Merkle *et al.* (1998) introduced a model, with a thermal equilibrium hypothesis, based on a transport equation of the vapour mass fraction x_v with the source term $-\frac{x_v}{\tau_v}$. The relaxation time τ_v is then described depending on the vaporisation pressure P_{vap}, the pressure difference regarding the threshold, an empirical constant k_e and characteristic quantities (U_{ref},τ_{ref}):

$$\frac{1}{\tau_v} = \begin{cases} 0 & \text{if } p_m < P_{vap} \\ \frac{1}{k_e \tau_{ref}} \frac{|p_m - P_{vap}|}{0.5 \rho_m U_{ref}^2}| & \text{if } p_m > P_{vap} \end{cases} \tag{1.8}$$

  Ducoin *et al.* (2012) recommends this model in comparison with Rayleigh-Plesset based ones.

- Kunz *et al.* (2000) suggested a model similar to the Merkle model. However, the transport equation is written for the liquid volume fraction and, for the liquid to vapour transformation, a simplified form of the Ginzburg-Landau potential is used for the mass transfer rate:

$$\dot{m} = \frac{C_e \rho_v}{\tau_\infty} \left((\alpha_l - \alpha_{ng})^2 (1 - \alpha_l - \alpha_{ng}) + \frac{\alpha_l \min[0, p_m - P_{vap}]}{1/2 \rho_l U_\infty^2} \right), \tag{1.9}$$

  where C_e is an empirical constant and τ_∞ a relaxation time. A non-condensable gas, represented by α_{ng}, is added to the formulation and could be neglected depending on the model hypothesis. The model is successfully used by Lindau *et al.* (2002). The cavitation model development of other works is also based on this model, like the ones of Shin *et al.* (2004) and Dittakavi *et al.* (2010). Senocak & Shyy (2004) also developed a Kunz based model where interface velocities are considered for the mass transfer estimation.

- Saito *et al.* (2007) proposed a model with a source term based on the Hertz-Knudsen equation Eq.(1.7):

$$\dot{m} = \begin{cases} C_e \alpha^2 (1-\alpha)^2 \frac{\rho_l}{\rho_v} \frac{P_{vap}-p_m}{\sqrt{2\pi r_e T_s}} & \text{if } p_m < P_{vap} \\ C_e \alpha^2 (1-\alpha)^2 \frac{P_{vap}-p_m}{\sqrt{2\pi r_e T_s}} & \text{if } p_m > P_{vap} \end{cases} \tag{1.10}$$

  where C_e is an empirical constant and T_s the saturation temperature. This cavitation model is adopted in the work of Gnanaskandan & Mahesh (2015, 2016*a*,*b*) and later in the study of Brandao *et al.* (2019) and Bhatt & Mahesh (2020) in which the results showed a great interpretation of sheet cavitation problems.

1.2.1.2.3 Models based on Gibbs free energy Saurel *et al.* (2008) proposed a model based on a five-equation formulation that includes a source term for the mass $\dot{m}$ and the heat Q transfer:

$$\dot{m} = \nu \rho_m (g_l - g_v) \quad \text{and} \quad Q = H_e (T_l - T_v),$$

where g stands for the Gibbs free energy and H_e a heat exchange coefficient.

1.2.1.2.4 Models based on the divergence of the velocity The mass transfer can be assumed to be proportional to the divergence velocity: the condensation is associated with compression of the fluid and the vaporisation with a stretching of the fluid. Therefore, the mass transfer term can be written as:

$$\dot{m} = Z \ \mathrm{div}(\mathbf{u}), \tag{1.11}$$

where Z is a coefficient to be determined. Goncalvès (2013) or Goncalvès & Charrière (2014) proposed a formulation of Z based on the Wallis speed of the sound c_{Wallis} and the mixture speed of the sound c_m:

$$\dot{m} = \frac{\rho_l \rho_v}{\rho_l - \rho_v} \left(1 - \frac{c_m^2}{c_{Wallis}^2} \right) \mathrm{div}(\mathbf{u}), \tag{1.12}$$

where c_{Wallis} is the propagation velocity of acoustic waves without mass transfer Wallis (1967). The choice of the equation of state directly impacts the formulation due to the change in the calculation of mixture speed of the sound. Thereafter, Charrière *et al.* (2015), Charrière & Goncalvès (2017) and Goncalves & Zeidan (2017, 2018) used with success this model in their works for different sheet cavitation cases.

1.2.1.2.5 Summary Besides the discrepancy of methods used to model cavitation with a transport equation, it has to be noticed that the majority of them gave relatively good results. There is no consensus in the literature for the cavitation model selection. It is not possible to emphasize the best one among all the diversity of this non-exhaustive list of models. Nonetheless, cavitation models based on constants selection or defined without considering thermodynamic effects could lead to difficulties to correctly replicate the physical phenomenon.

1.2.2 Turbulence modelling

Experimental studies highlighted the impact of vapour pockets or clouds on flow turbulence. Therefore, the selection of the turbulence model in numerical works has an important concern for cavitating flow simulation. The current section presents an overview of the different methods used for turbulence modelling in the literature.

1.2.2.1 Inviscid

Some authors chose to consider an inviscid flow for sheet cavitation simulation. Shin *et al.* (2004) found a correct agreement with experimental work on a flow within a Venturi. Later, Schnerr *et al.* (2008) or Budich *et al.* (2018) made this assumption to focus on inertial effect and proved its dominant role into the flow. The authors were able to capture the correct flow dynamics with the capture of shock waves and the same Strouhal number as the one observed in experiments. Nevertheless, the void ratio extraction is slightly overestimated at some points compared with experimental results. Saurel *et al.* (2016) succeded to reproduced the flow dynamics within a Venturi configuration as observed through the Strouhal number extraction and the mean cavity length compared to the experimental values. Other studies on cavitation simulation are based on the Euler equations, as the one carried out by Goncalves & Zeidan (2017, 2018). The authors chose to neglect the viscosity to focus their work on thermal effects and study different numerical scheme applied to cavitating flow.

1.2.2.2 Reynolds-Averaged Navier Stokes (RANS)

One of the most popular methods for turbulence modelling is RANS simulations. The range of turbulence models available for the estimation of the Reynolds stress gives the opportunity of computing a large diversity of cases using the appropriate model. First numerical results, using $k - \epsilon$ model, on

sheet cavitation flow showed an overestimation of the time-averaged void ratio and an underestimation of the re-entrant jet, as observed by Kunz *et al.* (2000) on ogives forebody with cylindrical afterbody or by Lindau *et al.* (2002) and Senocak & Shyy (2004) on Venturi flows. The same observation is underlined, with $k - \omega$ and Spalart-Allmaras models, by Goncalves & Patella (2009) or also with Baldwin-Lomax model by Saito *et al.* (2007) even if the numerical results showed reasonable agreement with experiments regarding the dynamics.

Reboud *et al.* (1998*a*) suggested that these turbulence models overestimate the eddy viscosity around two-phase areas and proposed an eddy viscosity correction that can be applied to any models. Coutier-Delgosha *et al.* (2003) noticed an improvement of the re-entrant jet capture with this correction applied on a $k-\epsilon$ model for a flow within a Venturi. Moreover, a good agreement with the experiment is found for the cavity length and the dynamics behaviour. The same observation with the same choice of model is made by Zwart *et al.* (2004). Many other models are used combined with the Reboud limiter as the RNG $k - \epsilon$ model selected by Chen *et al.* (2006) and Zhou & Wang (2008) on flows around hydrofoils. Both found reasonable agreement with experimental results and well-predicted flow behaviours like the periodic vortex shedding. However, Zhou et al. underlined discrepancies in the pressure estimation. Ji *et al.* (2014) and Peng *et al.* (2016) selected the same model for calculation of flows around a twisted hydrofoil. The results reproduced cavitation patterns with U-type structures and their evolution with primary and secondary vapour clouds sheddings highlighted by experimental observations. Close results on the twisted hydrofoil are obtained by Park & Rhee (2013) but with a lower quality of prediction for the vapour pocket shape, which is again explained by the overprediction of eddy viscosity in absence of limiter. The $k - \omega$ SST model with Reboud correction is also selected in numerical works as in Ducoin *et al.* (2012) or in Geng & Escaler (2018) on flows around hydrofoils. In the last study, a comparison with $k - \epsilon$ RNG and $k - \epsilon$ showed that $k - \omega$ SST better fit with experimental data but needed a more refined mesh at walls. Zhang *et al.* (2021) proposed a new version of the Reboud correction based on empirical constants applied with $k - \omega$ SST. Nonetheless, it represented only a little improvement and required a set-up for each model and cases. Goncalvès & Decaix (2012) underlined that using the Reboud correction, the $k - \ell$ model of Smith better-described flow within Venturi flows than the $k - \epsilon$ and the $k - \omega$ SST models. Goncalvès & Charrière (2014) also underlined the reasonable agreement with experiments for simulations on Venturi flows using the

Spalart-Allmaras model and the Reboud correction. Later, Charrière *et al.* (2015) and Charrière & Goncalvès (2017) used the $k-\ell$ model with Reboud correction on two different Venturi configurations. For the most dynamics flow, the comparison with experimental results showed a slight overestimation of void ratio but a relatively good agreement with the observation of pressure waves and pocket oscillations.

1.2.2.3 Modified RANS

More recently, several methods based on RANS formulation are used for sheet cavitation simulations. Ji *et al.* (2013*b*) proposed a Partial Averaged Navier Stokes (PANS) formulation, derived from $k-\epsilon$ model with only a coefficient modification, for flow simulation around a twisted hydrofoil. The numerical results agree fairly well with experimental observation for dynamics frequency extraction. Nonetheless, the results are not or slightly improved by the use of PANS instead of RANS methods. Kadivar *et al.* (2019) selected the same method for flow simulation around a hydrofoil to study the effect of Cylindrical Cavitating-bubble Generators on the flow. The authors observed a reasonable agreement with experimental data for the lift coefficient and highlighted the limitation of the instability development.

Another modification of the RANS implementation is the Scale-Adaptive Simulation (SAS), as the one used by Decaix & Goncalves (2013) on a Venturi configuration in which a satisfactory match between experiment and numerical results is found for time-averaged parameters using the $k-\ell$ model. A cross-flow in the recirculating area is also identified as observed in some experiments. Sedlar *et al.* (2016) and Hidalgo *et al.* (2019) chose the SST method using the $k-\omega$ model for computation of flows around a hydrofoil. In the first one, an improvement of turbulent frequency extraction and side-wall effects identification is underlined, compared to LES-WALE results. However, lower quality results are obtained for the description of vortical structures in the rear part of the hydrofoil. In the other case, the authors presented better results with SAS compared to ILES and a sufficient prediction of oscillation and pocket length. Sun *et al.* (2019*a*) used a Filter-Based Method (FBM) on RANS equations for a ventilated hydrofoil flow simulation. The authors found a reasonable agreement with experiments for break-off description, cavity growth and pressure but did not present a quantitative comparison for flow quantities.

1.2.2.4 Large-Eddy Simulation (LES)

The second most used method is called Large-Eddy Simulation (LES) and it consists of a spatial filter method of the small turbulent scales in the simulation. A Subgrid-Scale (SGS) model is used to model the smaller scales. The study of Arndt *et al.* (2000) was one of the first LES simulations of sheet cavitation configuration. The Smagorinsky subgrid scale model is selected for a flow computation around a hydrofoil. The simulation showed promising results for this time regarding the dynamics behaviour of the flow.

Later, Dittakavi *et al.* (2010) performed a cavitating flow simulation within a Venturi using the dynamic Smagorinsky model. However, no direct comparisons with experimental data are proposed. The dynamic Smagorinsky model is also used, combined with a shock-capturing method, in studies carried out by Gnanaskandan & Mahesh (2015, 2016*a*,*b*). In the case of a flow around a cylinder, their work showed different cavitation regimes and the sheet cavitation effects on the flow compared with non-cavitating ones. The other studied case is the Venturi flow simulation. The results presented a good agreement with experimental data regarding time-averaged flow parameters and underlined an improvement compared to Spalart-Allmaras RANS simulation results. The authors highlighted the unsteadiness of the flow by observing differences between the mean value of the void ratio and its most probable value. Pressure waves and the dominant role of adverse pressure gradient for re-entrant jet development are also identified. Brandao *et al.* (2019) pursued their work using the same turbulence model on a flow simulation around a cylinder for a range of cavitation numbers and Reynolds numbers. The study underlined that, based on the different cavitation regimes observation, the shedding of the cavity is triggered by shock waves that condense the vapour pocket. The Rankine–Hugoniot jump condition is selected to identify the shock speed. The authors also notified that the use of non-condensable gas implies the generation of lower pressure behind the shock. The investigation of the venturi flow simulation and the cavitation regimes, from incipient to periodic shedding, is updated by Bhatt & Mahesh (2020). A excellent agreement with experimental results (X-ray measurement of mean void ratio) is found for the transitory and periodic shedding regimes. Nonetheless, a void ratio overestimation is detected for incipient cavitation. Moreover, the instantaneous evolution of the void fraction field, the bubbly shock propagation speed and the shedding frequency showed a perfect agreement with the experiments. The selected numerical formulation permitted to capture both re-

entrant jet induced and shock induced regimes. In the transitory regime, a higher adverse pressure gradient is observed and supports the formation of the re-entrant jet. It is suggested that the overall low pressure in the cavity closure leads to reduce the speed of the sound and increase the medium compressibility. This effect promotes the generation of shock waves in the periodic regime. An analyse with Rankine-Hugoniot jump condition is proposed and highlighted that supersonic Mach numbers are mostly identified at the cavity closure (not inside the cavity where the velocity is low).

Hickel *et al.* (2011) proposed an Adaptive Local Deconvolution Method (ALDM) for flow simulation within a micro-channel with a step. It consists of an implicit formulation of LES in which the numerical scheme and the SGS model are directly coupled. The numerical results are in good agreement with available experimental data. Other computations are carried out using the same method as in the study of Egerer *et al.* (2014) on a flow through a generic throttle geometry. A quantitative comparison with experimental data of a cavitating turbulent mixing layer shows that mean velocity and vapour volume fraction are reproduced within the limits of experimental uncertainties. Furthermore, a mean flow field analysis underlined the presence of streamwise vortices not directly presumed from the experimental results. It illustrates the influence of LES computations complementing the experiment. Orley *et al.* (2015) or Trummler *et al.* (2020, 2021) also presented the last results using ALDM for flows within a nozzle. A good agreement with experiments is found for the dynamics. It is shown by the identification of shock induced shedding and re-entrant jet induced shedding at high cavitation number or the capture of a re-entrant jet in both shedding types. Moreover, the authors highlighted that the re-entrant jet formation is related to the pressure peak induced by the collapse of the detached cloud. Another study based on an implicit LES method, in which the numerical dissipation mimics the effect of small scale instead of SGS model, is proposed by Arabnejad *et al.* (2019) on a flow around a hydrofoil. A qualitative comparison with experiments showed that two sheddings are identified with two types of re-entrant jet: one from the leading edge and the other from the tail of the cavity.

Dumond *et al.* (2013) introduced the Monotone Integrated Large Eddy Simulation (MILES) for venturi flow and fluidic diode simulations. Correct results for pressure and void ratio are presented but discrepancies are identified for the velocity around the cavity. Ji *et al.* (2013*a*) worked on the Wall-Adapting Local Eddy-viscosity (WALE) model for flows simulation around a twisted hydrofoil.

The cavity growth, the break-off cycle and the collapse downstream the pocket agreed fairly well with experimental observations as well as the shedding frequency and the capture of U-shape vortices. Lots of authors used the WALE model for LES simulation. Huang *et al.* (2014) identified, on a flow around a hydrofoil, similar periodic behaviour between simulations and experiments. Nonetheless, an overprediction of the void ratio is raised. Sedlar *et al.* (2016) found correct results for the description of vortical structures in the rear part of a hydrofoil but also an overprediction of the oscillation frequency and an underestimation of sidewall effects. Long *et al.* (2018) noticed, on a flow around a twisted hydrofoil, a reasonable agreement with experiments for Strouhal number and time-averaged lift and identified the U-type structures linked to the primary and the secondary shedding. Chen *et al.* (2019) observed that the re-entrant jet is not the triggering mechanism for shedding in the case of highly turbulent flow around a hydrofoil. The authors added that the stream is always laminarised at the leading edge but identified downstream fluctuations of vortical waves in the spanwise direction. Sun *et al.* (2020) computed a flow around a ventilated hydrofoil (ventilation at the leading edge of the hydrofoil). The study suggested that the ventilation leads to an increase of the shedding frequency, a collapse of the pressure peak and transforms large-scale eddies into small-scale vortices. Nevertheless, in some cases, the WALE method is limited as previously shown in the work of Hidalgo *et al.* (2019) in comparison with SAS or Hybrid RANS/LES methods.

1.2.2.5 Hybrid RANS/LES

Hybrid RANS/LES is a bridging method between RANS and LES which is used in studies of cavitating flow simulation. A switch on a turbulence length is introduced to locally select the turbulence method. Kinzel *et al.* (2007) suggested that the implementation of the Detached-eddy Simulation (DES) approach could add the ability to capture a much broader spectrum of the turbulent scales, cavity dynamics, and better predict a range of cavitating flows. Later, Bensow (2011) performed a Delayed DES (DDES) simulation around a twisted hydrofoil. It corresponds to an improvement of the DES formulation based on the Spalart-Allmaras model with a delaying function for the switch into the boundary layer. The results presented a good agreement with experiments but showed fewer structures compared with the LES results.

Decaix & Goncalves (2013) proposed a DES formulation based on the Spalart-Allmaras RANS model to investigate the dynamics of a Venturi flow. The authors identified a cross-flow in the recirculating area as observed later in experiments. Sedlar *et al.* (2016) used a similar method based on the $k-\omega$ SST RANS formulation for flow simulation around hydrofoils. A good prediction of the turbulent frequency and sidewall effects is noticed. It presents an improvement compared to LES-WALE simulation results. However, the vortical structures in the rear part of the hydrofoil are better described by the LES-WALE method. More recently, Cheng *et al.* (2019) computed flow simulations around a sphere at different cavitation number using the DDES formulation of Spalart. The results showed a single frequency mode for high cavitation number and a dual-frequency mode for low value in which the low frequency corresponds to the natural flow frequency while the high frequency represents the dynamics evolution of cavitation. The study did not propose any comparisons with experiments.

1.2.2.6 Summary

The turbulence modelling in sheet cavitation is processed using different methods regarding the literature. The resolution of inviscid equations does not allow the identification of any flow structures but seems to be sufficient for the shock dynamics capture. RANS simulation with a limiter presents correct agreement with experimental data regarding time-average flow variables (pocket shape and length, re-entrant-jet ...) and dominant dynamics frequency extraction. Modified RANS methods show similar results and no major improvement compared to RANS. LES simulation allows a better physics analysis of the flow due to higher resolution. Nevertheless, the choice of the grid is of prior importance. In the case of a too coarse grid, the under resolution could lead to major discrepancies. Moreover, the user should keep in mind that strong hypotheses selected for the mixture flow limit the precision of the simulation. The two-phase smaller scale effects are also neglected in all LES studies. The addition of a "sub-bubble" scale model to the SGS model could be a solution to include the effect of two-phase smaller scale on the flow, as developed by Lakehal *et al.* (2002). Hybrid RANS/LES simulation can be seen as a good compromise but requires particular attention on the grid generation and the use of shielding functions. Finally, the lack of quantitative experimental data, such as turbulent quantities, in sheet cavitation is a limiting factor for the improvement of adequate turbulence models. The majority of the models employed in the literature are validated using qualitative comparison with experiments.

Chapter 2

Governing equations

Contents

2.1 The 1-fluid homogeneous approach **50**
2.2 The compressible RANS equations **50**
2.2.1 Mixture hypotheses 52
2.2.2 Turbulence modelling 52
2.3 The hybrid RANS/LES equations **55**
2.3.1 Delayed-Detached Eddy Simulation (DDES) 56
2.3.2 Definition of a $k-\ell$ DES model 57
2.3.3 Zonal Detached Eddy Simulation (ZDES) 59
2.4 The four-equation cavitation model **61**
2.4.1 Void ratio transport equation 61
2.4.2 Equations of state 62

The resolution of a two-phase system consists of calculating for each phase k:

- the density ρ_k,
- the three components of the velocity $u_{k,j}$,
- the total energy E_k decomposed as the sum of internal energy e_k and kinetic energy :

$$E_k = e_k + \frac{1}{2}u_k^2$$

Thus, the system presents five unknowns per phase calculated for each fluid by:

- two conservative equations for the mass and the energy,

· three conservative equations for the momentum, projected on the three directions j.

The system of equations introduces two additional thermodynamic variables : the phase pressure p_k and the phase temperature T_k. To determine both, the models use equations of state based on the conservative variables. Hence, each model embeds :

· a state law for the phase pressure p_k,

· an equation linking the phase temperature T_k to the internal phase energy e_k.

2.1 The 1-fluid homogeneous approach

There are several ways to simulate two-phase flows. The most straightforward one is to use a two-fluid model. Nevertheless, in the case of sheet cavitation simulation, this choice would lead to unaffordable computational costs and difficulties related to the interface tracking with the creation and the destruction of vapour pockets or the transfer terms computation due to the phase change. Therefore, a one-fluid homogeneous approach is selected to define the two-phase flow, which corresponds to the physical description of a vapour phase dispersed into the liquid phase. To that end, the two phase system is simplified by introducing hypotheses about the two-phase flow in regards to the phenomena which the simulation reproduced.

2.2 The compressible RANS equations

In order to model the creation and the dynamics of sheet cavities with a reasonable computational cost, it has been chosen to consider the two-phase flow as a homogeneous mixture. The fraction of presence α_k for a given k phase is defined between 0 and 1 such as $\sum_k \alpha_k = 1$. Furthermore, it is first intended to decompose flow variables as an averaged part $\overline{(\cdot)}$, and a fluctuated one $(\cdot)'$:

$$u = \overline{u} + u', \tag{2.1}$$

to solve equations of averaged quantities. It corresponds to the resolution of the Reynolds Averaged Navier-Stokes (RANS) system of equations if one considers a time-averaging. However, it is practical in a computational point of view for compressible flows, such as a cavitating flow, to use time-averaged

density and pressure (Reynolds averaged) and a temporal mean weighted by the mass for the other flow variables (Favre mean):

$$\tilde{u}_i = \frac{\overline{\rho u_i}}{\overline{\rho}} \ ; \ \tilde{T} = \frac{\overline{\rho T}}{\overline{\rho}} \ ; \ \tilde{e} = \frac{\overline{\rho e}}{\overline{\rho}} \ ; \ \tilde{E} = \frac{\overline{\rho E}}{\overline{\rho}} = \tilde{e} + \frac{\tilde{u}_i \tilde{u}_i}{2} + \frac{\widetilde{u_i'' u_i''}}{2}. \tag{2.2}$$

Then, the following decompositions can be defined:

$$u_i = \tilde{u}_i + u_i'' \ ; \ \rho = \overline{\rho} + \rho' \ ; \ p = \overline{p} + p' \ ; \tag{2.3}$$

$$T = \tilde{T} + T'' \ ; \ e = \tilde{e} + e''. \tag{2.4}$$

When considering a two-phase flow simulation, time-averaged variables for each phase k are computed based on the time of presence τ_k of the phase k and no longer on the global time τ, hence:

$$\rho_k = \overline{\overline{\rho}}_k + \rho_k'' \ ; \ u_{k,i} = \tilde{u}_{k,i} + u_{k,i}'' = \frac{\overline{\overline{\rho_k u_{k,i}}}}{\overline{\overline{\rho_k}}} + u_{k,i}''. \tag{2.5}$$

The same decomposition is applied for all the variables of each phase k. Then, the mixture variables are considered as defined from the phasic variables and the fraction of presence α_k:

- the mixture density $\rho_m = \sum_k \alpha_k \overline{\overline{\rho}}_k$,
- the mixture pressure $p_m = \sum_k \alpha_k \overline{\overline{p}}_k$,
- the mixture internal energy $\rho_m e_m = \sum_k \alpha_k \overline{\overline{\rho_k e_k}}$,
- the mixture velocity (mass center velocity) $\rho_m u_{m,i} = \sum_k \alpha_k \overline{\overline{\rho}}_k \tilde{u}_{k,i}$,
- the mixture dynamic viscosity $\nu_m = \sum_k \alpha_k \nu_k$
- the mixture viscous stress tensor $\sigma_{m,ij} = \overline{\overline{\mu}}_m \left[\frac{\partial \tilde{u}_{m,i}}{\partial x_j} + \frac{\partial \tilde{u}_{m,j}}{\partial x_i} - \frac{2}{3} \frac{\partial u_{m,n}}{\partial x_n} \delta_{ij} \right]$,
- the mixture thermal conductivity $\lambda_m = \sum_k \alpha_k \lambda_k$,
- the mixture temperature assuming the thermal equilibrium at the interface $T_m = \overline{\overline{T}}_k$,
- the mixture heat flow $q_{m,i} = \lambda_m \frac{\partial T_m}{\partial x_i}$.

2.2.1 Mixture hypotheses

Several equilibrium hypotheses between phases could be set within the mixture, depending on the model selection. First, the thermodynamic equilibrium is considered, which involves the equality of pressure and temperature between both phases:

$$p_l = p_v = p_m, \tag{2.6}$$

$$T_l = T_v = T_m. \tag{2.7}$$

The mixture pressure p_m and temperature T_m are defined using particular equations of state for cavitation introduced later in the manuscript. The homogeneous mixture hypothesis implies no sliding velocity between both phases, and the normal velocities are considered equal as it is mean quantities. Thus, the phase velocities are both assumed equal to the mixture velocity $\boldsymbol{u}_m$:

$$\boldsymbol{u}_l = \boldsymbol{u}_v = \boldsymbol{u}_m. \tag{2.8}$$

All these hypotheses simplify the definition of the system of conservative equations. Quantities such as momentum or energy transfers are neglected. Hence, the system of averaged conservative equations for a homogeneous mixture is:

$$\begin{cases} \dfrac{\partial \rho_m}{\partial t} + \dfrac{\partial \rho_m u_{m,j}}{\partial x_j} = 0 \\ \dfrac{\partial \rho_m u_{m,i}}{\partial t} + \dfrac{\partial \rho_m \, u_{m,i} u_{m,j}}{\partial x_j} = -\dfrac{\partial p_m}{\partial x_i} + \dfrac{\partial \sigma_{m,ij} + \tau_{m,ij}}{\partial x_j} \\ \dfrac{\partial \rho_m \left(E_m + k_m\right)}{\partial t} + \dfrac{\partial \left[\rho_m \left(E_m + k_m\right) + p_m\right] u_{m,j}}{\partial x_j} = \dfrac{\partial \left(\sigma_{m,ij} + \tau_{m,ij}\right) u_{m,j}}{\partial x_j} \\ \qquad\qquad - \dfrac{\partial q_{m,j}}{\partial x_j} - \dfrac{\partial q^t_{m,j}}{\partial x_j} \end{cases} \tag{2.9}$$

2.2.2 Turbulence modelling

The mixture turbulent stress tensor τ_m and the turbulent heat flux vector q^t_m are formulated using the Boussinesq relation and the Fourier law, respectively defined as:

$$\tau_{m,ij} = \mu_{tm} \left[\frac{\partial u_{m,i}}{\partial x_j} + \frac{\partial u_{m,j}}{\partial x_i} - \frac{2}{3} \frac{\partial u_{m,n}}{\partial x_n} \delta_{ij} \right] - \frac{2}{3} \rho_m k_m \delta_{ij} \, , \tag{2.10}$$

$$q^t_{m,j} = \lambda_{tm} \frac{\partial T_m}{\partial x_j} \approx \frac{\mu_{tm} C_{pm}}{Pr_t} \frac{\partial T_m}{\partial x_j} \, , \tag{2.11}$$

with turbulent Prandtl number $Pr_t = 1$ and k_m the mixture turbulent kinetic energy. The mixture eddy viscosity μ_{tm} is then computed using one of the following turbulence models.

2.2.2.1 Spalart-Allmaras model

Spalart & Allmaras (1992, 1994) developed a one-equation model composed of transport equation of a modified eddy viscosity: $\nu_{tm} = f_{v1}\widetilde{\nu}$. In conservative form this equation is expressed:

$$\begin{aligned}\frac{\partial \bar{\rho}\widetilde{\nu}}{\partial t} + \frac{\partial}{\partial x_k}\left[\bar{\rho}\widetilde{u}_k\widetilde{\nu} - \frac{1}{\sigma}\left(\mu + \bar{\rho}\widetilde{\nu}\right)\frac{\partial \widetilde{\nu}}{\partial x_k}\right] &= c_{b1}\left(1 - f_{t2}\right)\widetilde{S}\bar{\rho}\widetilde{\nu} + \frac{c_{b2}}{\sigma}\frac{\partial \bar{\rho}\widetilde{\nu}}{\partial x_k}\frac{\partial \widetilde{\nu}}{\partial x_k} \\ &\quad - \left(c_{\omega 1}f_{\omega} - \frac{c_{b1}}{\kappa^2}f_{t2}\right)\bar{\rho}\frac{\widetilde{\nu}^2}{d^2}\end{aligned} \tag{2.12}$$

- $f_{\nu 1}$ is a viscous damping term calculated as $f_{\nu 1} = \dfrac{\chi^3}{\chi^3 + c_{\nu 1}^3}$ where $\chi = \widetilde{\nu}/\nu$,

- $P_{\nu} = c_{b1}\left(1 - f_{t2}\right)\widetilde{S}\bar{\rho}\widetilde{\nu}$ represents eddy viscosity production term with $\widetilde{S} = S + \frac{\widetilde{\nu}}{\kappa^2 d^2}f_{\nu 2}$ where $S = \sqrt{2\tilde{S}_{ij}\tilde{S}_{ij}}$, $\tilde{S}_{ij} = \frac{1}{2}\left(\frac{\partial \tilde{u}_i}{\partial x_j} - \frac{\partial \tilde{u}_j}{\partial x_i}\right)$ and d is the wall distance. This expression introduces two other damping functions: $f_{\nu 2} = 1 - \frac{\chi}{1+\chi f_{\nu 1}}$ and $f_{t2} = c_{t3}.\exp\left(-c_{t4}\chi^2\right)$

- $D_{\nu} = \left(c_{\omega 1}f_{\omega} - \frac{c_{b1}}{\kappa^2}f_{t2}\right)\bar{\rho}\frac{\widetilde{\nu}^2}{d^2}$ describes the diffusion of the eddy viscosity and introduces $f_{\omega} = g\left(\frac{1+c_{\omega 3}^6}{g^6+c_{\omega 3}^6}\right)^{1/6}$, $g = r + c_{\omega 2}\left(r^6 - r\right)$, $r = \frac{\widetilde{\nu}}{\widetilde{S}\kappa^2 d^2}$ and $c_{\omega 1} = \frac{c_{b1}}{\kappa^2} + \frac{(1+c_{b2})}{\sigma}$

The algebraic values of the model parameters introduced by this model are presented in Table 2.1.

Table 2.1: Coefficients of the Spalart-Allmaras model

c_{b1}	c_{b2}	σ	κ	$c_{\omega 2}$	$c_{\omega 3}$	$c_{\nu 1}$	c_{t3}	c_{t4}
0,1335	0,622	$\frac{2}{3}$	0,41	0,3	2	7,1	1,1	2

2.2.2.2 $k - \ell$ of Smith model

The model is composed of a transport equation of the turbulent kinetic energy k, and another one of the turbulent length ℓ whose formulation is proposed by Smith (1990, 1994) based on the model of

Rotta:

$$\frac{\partial \bar{\rho} k}{\partial t} + \frac{\partial}{\partial x_j}\left[\bar{\rho}\widetilde{u}_j k - \left(\mu + \frac{\mu_t}{\sigma_k}\right)\frac{\partial k}{\partial x_j}\right] = \bar{\rho} P_k - \frac{\bar{\rho}(2k)^{3/2}}{B_1 \ell} - 2\mu \frac{\partial \sqrt{k}}{\partial x_j}\frac{\partial \sqrt{k}}{\partial x_j} \tag{2.13}$$

$$\begin{aligned}\frac{\partial \bar{\rho} \ell}{\partial t} + \frac{\partial}{\partial x_j}\left[\bar{\rho}\widetilde{u}_j \ell - \left(\mu + \frac{\mu_t}{\sigma_\ell}\right)\frac{\partial \ell}{\partial x_j}\right] &= (2 - E_2)\frac{\bar{\rho}\sqrt{2k}}{B_1}\left[1 - \left(\frac{\ell}{\kappa d}\right)^2\right] \\ &\quad - \frac{1}{\ell}\left(\frac{\mu_t}{\sigma_\ell}\right)\frac{\partial \ell}{\partial x_j}\frac{\partial \ell}{\partial x_j}\left(\frac{\ell}{\kappa d}\right)^2 + \bar{\rho}\ell\frac{\partial \widetilde{u}_j}{\partial x_j} \\ &\quad + \frac{2}{k}\left(\frac{\mu_t}{\sigma_\ell}\right)\frac{\partial k}{\partial x_j}\frac{\partial \ell}{\partial x_j}\end{aligned} \tag{2.14}$$

The eddy viscosity calculation introduces a damping function f_μ:

$$\mu_{tm} = \mu \chi f_\mu = \rho \frac{(2k)^{1/2}\ell}{B_1^{1/3}} f_\mu \tag{2.15}$$

with:

$$\chi = \rho \frac{(2k)^{1/2}\ell}{\mu B_1^{1/3}}, \quad f_\mu = \left(\frac{C_1^4 f_1 + C_2^2\chi^2 + \chi^4}{C_1^4 + C_2^2\chi^2 + \chi^4}\right)^{1/4} \quad \text{and} \quad f_1 = exp\left[-50\left(\frac{\ell}{\kappa d}\right)^2\right]. \tag{2.16}$$

The variable d represents the wall distance, and the parameters of the model are given in Table 2.2:

Table 2.2: Coefficients of the $k - \ell$ model

κ	B_1	E_2	C_1	C_2	σ_k	σ_ℓ
0,41	18	1,2	25,2	2	1,43	1,43

2.2.2.3 Eddy viscosity correction

A limiter term is applied to the calculation of the turbulent viscosity property of mixture fluid, μ_{tm}. The correction is motivated by previous results (Reboud *et al.*, 1998*a*; Decaix & Goncalves, 2012), which indicate an overestimation of such a quantity for the two-phase flow configurations of interest. For the $k_m - \ell_m$ model, the limitation is computed using a function over ρ_m and is here written as :

$$\mu_{tm} = f(\rho_m) C_\mu^{1/4}\sqrt{k_m}\ell_m, \tag{2.17}$$

$$f(\rho_m) = \rho_v + \left(\frac{\rho_v - \rho_m}{\rho_v - \rho_l}\right)^n (\rho_l - \rho_v), \tag{2.18}$$

where ρ_v and ρ_l stand for the saturation vapour and liquid density, respectively. For the Spalart-Allmaras model, the eq. (13) is replaced by:

$$\mu_{tm} = f(\rho_m) f_{v1} \tilde{\nu} \tag{2.19}$$

The limitation is controlled by the parameter $n >> 1$, specified in the numerical validation section. Furthermore, the work of Dandois (2014) indicates the possibility of non-physical flow results related to an overestimation of the turbulent viscosity in corners. Hence, the Quadratic Constitutive Relation (QCR) correction (Spalart, 2000) is applied to the Reynolds stress tensor:

$$\tau_{m,ij}^{QCR} = \tau_{m,ij} - c_{nl1}(O_{ik}\tau_{m,jk} + O_{jk}\tau_{m,ik}) \,, \tag{2.20}$$

where $c_{nl1} = 0.3$ is an empirical constant and O_{ik} is the normalised rotation tensor:

$$O_{ik} = \frac{\dfrac{\partial u_i}{\partial x_k} - \dfrac{\partial u_k}{\partial x_i}}{\sqrt{\dfrac{\partial u_n}{\partial x_p}\dfrac{\partial u_p}{\partial x_n}}} \,, \tag{2.21}$$

The formulation is first developed for the Spalart-Allmaras turbulence model. However, the author assumed that this correction could be applied to the other RANS turbulence models.

2.3 The hybrid RANS/LES equations

Hybrid RANS/LES methods are introduced to increase the accuracy of the results of simulations while keeping an affordable computational time. These methods are built initially to use the RANS formulation around walls, which are the more resource consuming areas in the case of a full Large-Eddy Simulation (LES). Therefore, the hybrid approach uses either the RANS or the LES solving approach on a switch function defined with a characteristic length. Once this length is defined for the LES formulation, it acts as the LES spatial filter, which is the scale threshold between the resolved and the modelled parts of the energy spectrum. Hence, the LES method is developed to solve the large scales and model or dissipate the small ones. In the case of modelling the effect of the small scales, a subgrid-scale model is selected. The switch between the RANS type solver and the LES one can be introduced using diverse approaches by modifying the dissipation rate term of the RANS turbulence model. The LES set of equations used in present work is based in the System I formulation of Vreman

et al. (1995) (Garnier *et al.*, 2009) in which the double correlation term is simplified, *i.e*

$$\tilde{e} = \frac{\overline{p}}{(\gamma - 1)} + \frac{1}{2}\overline{\rho}\widetilde{u_i u_j} \approx \frac{\overline{p}}{(\gamma - 1)} + \frac{1}{2}\overline{\rho}\tilde{u}_i\tilde{u}_j \,. \tag{2.22}$$

Moreover, only the terms of the System I formulation that present a significant importance on DNS test cases (Vreman *et al.*, 1995) are considered in the present work.

2.3.1 Delayed-Detached Eddy Simulation (DDES)

Spalart *et al.* (1997) presented a hybrid formulation called Detached Eddy Simulation (DES) based on the Spalart-Allmaras one-equation RANS turbulence model. The characteristic turbulence length of the model is the wall distance d_W. The article proposed the introduction of a switch on this length and replace it by:

$$\tilde{d} = \min(d_W, C_{DES}\Delta), \tag{2.23}$$

where $C_{DES} = 0.65$ for Spalart-Allmaras (Spalart *et al.*, 1997) and the subgrid length scale Δ (which controls which wavelengths can be resolved as well as the eddy viscosity level) is $\Delta = \Delta_{max} = \max(\Delta x, \Delta y, \Delta z)$. The switch from the wall distance to the LES length transforms the turbulence equation to the Smagorinsky subgrid-scale model. Thus, the LES resolution is employed far from walls, and the RANS Spalart-Allmaras is used close to walls. Moreover, the LES length, which depends on the mesh definition, gives the level of resolution of the computation in the LES areas. Later, Spalart *et al.* (2006) improved DES method introducing a delayed function f_d into the turbulent length computation:

$$\tilde{d} = d_W - f_d \max(0, d_W - C_{DES}\Delta). \tag{2.24}$$

The blending function f_d is defined to "shield the boundary layer" by delaying the LES function.

$$f_d = 1 - tanh([8r_d]^3), \tag{2.25}$$

with the parameter r_d:

$$r_d = \frac{\mu_t + \mu}{\sqrt{U_{i,j}U_{i,j}}\kappa^2 d_W^2}. \tag{2.26}$$

Both f_d and r_d are defined and calibrated for the Spalart-Allmaras model.

Deck (2011) presented an evolution to the DDES used in type II of the ZDES formulation. The author proposed a modification in the definition of the subgrid length scale Δ_{new}:

$$\Delta_{new} = (0.5 + sign(0.5, f_d - f_{d0}))\Delta_{max} + (0.5 - sign(0.5, f_d - f_{d0}))\Delta_\omega \tag{2.27}$$

where $\Delta_\omega = \sqrt{\frac{\sum_i^{N_f} |\boldsymbol{\omega}.\boldsymbol{\mathcal{S}_i}|}{2||\boldsymbol{\omega}||}}$, N_f the number of faces, $\mathcal{S}_i$ the oriented surface and $f_{d0} = 0.8$, which corresponds to the optimal value measured in a flat plate case ($f_{d0} \in [0.75; 0.99]$). In that formulation, f_d is used to determine which length scale is selected above and below f_{d0}. The computation of the new subgrid length Δ_{new} involves the velocity and the eddy viscosity fields in addition to the mesh dimension.

A correction of RANS damping term behaviour is studied by Spalart *et al.* (2006) or Mockett (2009):

$$L_{LES} = C_{DES}\Psi\Delta. \tag{2.28}$$

This damping term Ψ is developed as follows for the Spalart-Allmaras model :

$$\Psi_{SA} = \min\left(100; \frac{1 - \frac{C_{b1}}{C_{w1}\kappa f_w^*}[f_{t2} + (1 - f_{t2})f_{v2}]}{f_{v1}\max(10^{-10}; 1 - f_{t2})}\right), \tag{2.29}$$

where f_w^* is the asymptotic value of f_w for high eddy viscosity value. In addition, the parameter r_d is modified :

$$r_d = \frac{\mu_t + \mu}{\kappa^2 d^2 \max(10^{-10}; \sqrt{U_{i,j}U_{i,j}})}. \tag{2.30}$$

With the Edwards correction:

$$\Psi_{SAE} = \min\left(100; \left(\frac{\max(f_{v1}; 10^{-10})}{\max(\chi; 10^{-10})} + f_{v1}^2\right)^{-1}\right), \tag{2.31}$$

Moreover, it has to be noticed that the transition term f_{t2} of the Spalart-Allmaras model 2.2.2.1 is set to zero in the case of hybrid RANS/LES formulation as observed in some studies (Deck, 2011; Sagaut *et al.*, 2013).

2.3.2 Definition of a $k - \ell$ DES model

The $k - \ell$ model of Smith is the RANS model that presents the best results in the current study. Therefore, it is pertinent to select a hybrid RANS/LES method based on this model. Nonetheless, no references have been found about any $k - \ell$ DES model. Hence, a model inspired by the $k - \omega$ formulation is proposed below.

According to the DES formulation of the $k - \omega$ model described by Strelets (2001) and Menter & Kuntz (2004), the dissipative term ϵ of the kinetic energy transport equation, is defined as :

$$\epsilon = \frac{k^{3/2}}{L_t} F_{DES}, \tag{2.32}$$

where F_{DES} is the switch function between the RANS and the LES formulation:

$$F_{DES} = \max(\frac{L_t}{C_{DES}\Delta}(1 - F_s); 1). \tag{2.33}$$

The function F_s is a shield function for the boundary layer and could be selected in different ways. F_s could be defined as the blending function f_{DDES} used in DDES or one of the shielding functions of the SST model :

$$F_1 = \tanh\left(\max\left(\frac{L_t}{d_W}; \frac{500\nu}{d_W^2\omega}\right)^2\right) \quad \text{or} \quad F_2 = \tanh\left(\max\left(2\frac{L_t}{d_W}; \frac{500\nu}{d_W^2\omega}\right)^2\right). \tag{2.34}$$

Then, the definition of the appropriate turbulent length L_t is necessary to describe the model. For $k-\omega$, the turbulent length is $L_t = \sqrt{k}/\beta^*\omega$. By analogy, the term F_{DES} is defined in the $k-\ell$ model, with $L_t = B_1\ell/2^{3/2}$, by :

$$F_{DES} = \max\left(\frac{B_1\ell}{2^{3/2}C_{DES}\Delta}(1 - F_s); 1\right), \tag{2.35}$$

where F_s is developed as f_{DDES}, F_1 or F_2:

$$f_{DDES} = tanh\left(\left[8\frac{\mu_t + \mu}{\sqrt{U_{i,j}U_{i,j}}\kappa^2 d_W^2}\right]^3\right), \tag{2.36}$$

$$F_1 = \tanh\left(\max\left(\frac{B_1\ell}{2\sqrt{2}d_W}; \frac{500\nu\ell}{\sqrt{k}d_W^2}\right)^2\right), \tag{2.37}$$

$$F_2 = \tanh\left(\max\left(\frac{B_1\ell}{\sqrt{2}d_W}; \frac{500\nu\ell}{\sqrt{k}d_W^2}\right)^2\right). \tag{2.38}$$

The F_1 and F_2 functions are defined to be ≈ 1 into the boundary layer and 0 elsewhere. The second part of the maximum ensures that both functions do not get near to the value of 0 into the viscous sublayer.

Hence, the dissipation term can be written, for the $k-\ell$ model, as:

$$\epsilon = \frac{(2k)^{3/2}}{B_1\ell}\max\left(\frac{B_1\ell}{2^{3/2}C_{DES}\Delta}(1 - F_s); 1\right), \tag{2.39}$$

The turbulent viscosity ν_t calculation depends as well on the switch between RANS and LES :

$$\nu_t = \begin{cases} \frac{(2k)^{1/2}\ell}{B_1^{1/3}} f_\mu^{RANS} & \text{for the RANS part,} \\ \frac{4\sqrt{k}C_{DES}\Delta}{B_1^{4/3}} f_\mu^{LES} & \text{for the LES part.} \end{cases} \tag{2.40}$$

It has to be noticed that the farther from the wall it is, the closer to 1 f_μ is. The turbulent viscosity is then written , in the LES part (Chaouat & Schiestel, 2007), as :

$$\nu_t \simeq \frac{4C_{DES}\sqrt{k}\Delta}{B_1^{4/3}} \simeq c_\mu \sqrt{k}\Delta. \tag{2.41}$$

Therefore, C_{DES} can be approximated by :

$$C_{DES} \simeq \frac{c_\mu B_1^{4/3}}{4} \simeq 0.59, \tag{2.42}$$

with $c_\mu \simeq 0.05$ as described by Yoshizawa & Horiuti (1985).

2.3.3 Zonal Detached Eddy Simulation (ZDES)

The third hybrid method studied in the present is the Zonal Detached Eddy Simulation (ZDES). It includes the definition of RANS zones by the user and is based on the Spalart-Allmaras model. Deck (2011) introduced a label *ides* which locally defines RANS resolution areas and DES resolution areas:

$$ides(n) = \begin{cases} 0 & \text{for the RANS simulation,} \\ 1 & \text{for the DES simulation.} \end{cases}$$

The ZDES formulation is inspired by the DES and the DDES from Spalart but differs for the LES length scale definition. Three types of length scale definitions are presented:

- **Type I** is close to the DES formulation but using Δ_ω instead of Δ_{max}:

$$\tilde{d}_I = \min(d_W, C_{DES}\Delta_\omega) \tag{2.43}$$

- **Type II** is close to the DDES formulation but using the Δ_{new}, previously defined, instead of Δ_{max}:

$$\tilde{d}_{II} = d_W - f_d \max(0, d_W - C_{DES}\Delta_{new}) \tag{2.44}$$

- **Type III** differs from the other ones by defining a RANS resolution area along the wall up to a selected distance δ.

$$\tilde{d}_{III} = \begin{cases} d_W & \text{if} \quad d_W < d_W^{int} \\ \min(d_W, C_{DES}\Delta_\omega) & \text{otherwise} \end{cases} \tag{2.45}$$

The type I was not selected for the study, and the type II was previously introduced as an improvement of the DDES. The type III is presented in the following section.

2.3.3.1 ZDES type III

Renard & Deck (2015) and Vaquero *et al.* (2021) proposed a complete formulation for the use of the type III ZDES. The major improvement is the addition of an interface function f_i to smooth the change of the characteristic turbulent length and thus the turbulent viscosity around the switch area. To that end, the turbulent length is computed using the following formula:

$$\tilde{d}_{III} = (1 - f_i)d_W + f_i \min(d_W, C_{DES}\Delta_\omega). \tag{2.46}$$

The interface function should be defined between 0 and 1 on a restricted area corresponding to the switch zone. Furthermore, f_i is defined as 0 in the full RANS areas and 1 in full LES areas. Renard & Deck (2015) highlighted the necessity of the definition of a function with continuous wall-normal derivatives. Therefore, a parameter ξ is defined between -1 and 1 in the interface zone:

$$\xi = \frac{d_W - d_W^{int}}{0.1 d_W^{int}}. \tag{2.47}$$

The interface zone then lies between $0.9 d_W^{int}$ and $1.1 d_W^{int}$. Hence, the whole interface function is described as:

$$f_i(\xi) = \begin{cases} 0 & \text{if} \quad \xi \leq -1 \\ \dfrac{1}{1 + \exp\left(\frac{-6\xi}{1-\xi^2}\right)} & \text{if} \quad -1 < \xi < 1 \\ 1 & \text{if} \quad \xi \geq 1 \end{cases} \tag{2.48}$$

Moreover, the formulation of the model is based on the Spalart-Allmaras formulation (Sec. 2.2.2.1). The turbulent viscosity is modified to take into account the switch between RANS and LES:

$$\nu_t = \tilde{\nu} f_{\nu 1}^{III} \quad \text{with} \quad f_{\nu 1}^{III} = (1 - f_i) f_{\nu 1} + f_i. \tag{2.49}$$

The $\tilde{S}$ term in the eddy viscosity production P_ν is changed to

$$\tilde{S}^{III} = S + \frac{\tilde{\nu}}{\kappa^2 d_{III}^2} f_{\nu 2}^{III} \quad \text{with} \quad f_{\nu 2}^{III} = (1 - f_i) f_{\nu 2}, \tag{2.50}$$

and in the diffusion term D_ν, function f_ω is adjusted to

$$f_\omega^{III} = (1 - f_i) f_\omega + f_i. \tag{2.51}$$

2.4 The four-equation cavitation model

The void ratio α is defined as the averaged fraction of presence for the vapour phase. As introduced in Chapter 1, numerous formulations were studied for sheet cavitation simulation. In the present, the four-equation system is selected with the cavitation model developed by Goncalvès (2013).

2.4.1 Void ratio transport equation

The void ratio transport equation directly calculates the void ratio, which is considered a quantity convected by the flow and whose production and destruction processes are modelled by the source term. The first step of developing of this transport equation is to combine the conservative mass equations of the vapour phase

$$\frac{\partial \alpha \rho_v}{\partial t} + \frac{\partial \alpha \rho_v u_{v,j}}{\partial x_j} = \dot{m},$$

and the liquid phase

$$\frac{\partial (1-\alpha)\rho_l}{\partial t} + \frac{\partial (1-\alpha)\rho_l u_{l,j}}{\partial x_j} = -\dot{m}, \tag{2.52}$$

where $\dot{m}$ is the mass flow rate from the liquid phase to the vapour phase. Then, applying the hypotheses of thermodynamic equilibrium and a homogeneous mixture gives the following transport equation of the void ratio.

$$\frac{\partial \alpha}{\partial t} + u_{m,j}\frac{\partial \alpha}{\partial x_j} = K\frac{\partial u_{m,j}}{\partial x_j} + \frac{\dot{m}}{\rho_I}\,. \tag{2.53}$$

The development of the transport equation is presented with more details in Appendix A. The mass flow rate $\dot{m}$ can be assumed to be proportional to the divergence velocity: the condensation is associated with compression of the fluid and the vaporisation with a stretching of the fluid. Goncalvès (2013) proposed the following formulation linked to the choice of the equation of state:

$$\dot{m} = \frac{\rho_l \rho_v}{\rho_l - \rho_v}\left(1 - \frac{c_m^2}{c_{Wallis}^2}\right)\frac{\partial u_{m,j}}{\partial x_j}\,. \tag{2.54}$$

The calculation is based on the Wallis speed of sound c_{Wallis}, which is expressed as a weighted harmonic mean of each one of the two flow phases speed of the sound Wallis (1967):

$$\frac{1}{\rho_m c_{Wallis}} = \frac{\alpha}{\rho_v c_v^2} + \frac{(1-\alpha)}{\rho_l c_l^2}\,, \tag{2.55}$$

where c_k stands for the pure phase speed of sound. Moreover, the interface density ρ_I and the constant K are respectively defined as

$$\rho_I = \frac{\dfrac{\rho_l c_l^2}{1-\alpha} + \dfrac{\rho_v c_v^2}{\alpha}}{\dfrac{c_l^2}{1-\alpha} + \dfrac{c_v^2}{\alpha}} \quad \text{and} \quad K = \frac{\rho_l c_l^2 - \rho_v c_v^2}{\dfrac{\rho_v c_v^2}{\alpha} + \dfrac{\rho_l c_l^2}{1-\alpha}} \,. \tag{2.56}$$

2.4.2 Equations of state

Two different equations of state (EOS) are used for the system closure depending on a pressure threshold. The stiffened gas EOS above the threshold defines the mixture pressure and temperature, corresponding to the liquid part. In contrast, sinusoidal EOS are applied below, corresponding to the part with vapour appearance (Charrière *et al.*, 2015). The threshold is calculated from the vaporisation pressure P^{vap} and a delta pressure based on a chosen parameter c_{min}, the minimal speed of sound in the mixture:

$$\Delta p_m = \left(\frac{\rho_l - \rho_v}{2}\right) c_{min}^2 \frac{\pi}{2}. \tag{2.57}$$

The selection of c_{min} is based on the study of Charrière (2015) and set to 0.472 $m.s^{-1}$. This parameter allows the activation in advance of the phase change to smooth the density gradient around the interface. The density jump between the liquid and the vapour is stiff for a mixture problem. Thus, the mixture pressure is computed according to the relation :

$$\begin{cases} p_{SG} & \text{if} \quad p_m \geq P^{vap} + \Delta p \\ p_{sinus} & \text{otherwise}\,, \end{cases} \tag{2.58}$$

with p_{SG} and p_{sinus} the pressure respectively defined by the stiffened gas EOS and the sinusoidal EOS:

$$p_{SG}(\rho_m, e_m) = (\gamma_m - 1)\rho_k(e_m - \hat{q}_m) - \gamma_m p_{m,\infty}\,, \tag{2.59}$$

$$p_{sinus}(\alpha) = P_{vap} + \left(\frac{\rho_l - \rho_v}{2}\right) c_{min}^2 \arcsin(1-2\alpha)\,, \tag{2.60}$$

where the mixture energy of formation $\rho_m \hat{q}_m = \alpha\rho_v\hat{q}_v + (1-\alpha)\rho_l\hat{q}_l$ is calculated from $\hat{q}_v$ and $\hat{q}_l$, which stand respectively to the vapour and the liquid energies of formation. The mixture temperature is set equally above and below the pressure threshold :

$$T_m(\rho_m, e_m) = \frac{h_m(\alpha) - \hat{q}_m(\alpha)}{C_{p_m}(\alpha)} = \frac{e_m(\alpha) + p_m(\alpha)/\rho_m(\alpha) - \hat{q}_m(\alpha)}{C_{p_m}(\alpha)}\,, \tag{2.61}$$

where h_m and e_m are the specific mixture enthalpy and internal energy, respectively. The thermal capacity of the mixture C_{p_m} is defined with C_{p_v} and C_{p_l}, which stand for the thermal capacity of the vapour and the liquid, respectively,

$$\rho_m C_{p_m}(\alpha) = \alpha \rho_v C_{p_v} + (1-\alpha)\rho_l C_{p_l} \,. \tag{2.62}$$

The mixture speed of sound c_m is processed following the same approach. Above the pressure threshold, the Wallis speed of sound, Eq. (2.55), is considered, while below the threshold, the speed of sound is computed using the sinusoidal EOS, Eq. 2.63. The reader can find more details on the study of the speed of sound development performed by Charrière (2015). For the current case, the phase change does not affect the temperature of the mixture. Therefore, the phase enthalpy h_k and phase density ρ_k are defined as constants for a reference temperature T_{ref}.

$$c_m^2 = (\gamma_m - 1)\frac{\rho_v \rho_l (h_v^{ref} - h_l^{ref})}{\rho_m(\rho_l - \rho_v)} + \frac{A\, c_{min}^2}{\sqrt{1-(A(1-2\alpha))^2}} \,. \tag{2.63}$$

The phase enthalpy is $h_k^{ref} = C_{p_k} T_{ref} + q_k$. The A coefficient is added to guarantee the velocity fitting with Wallis speed of sound above the pressure threshold. In Goncalves & Patella (2009), it is shown that $A = 1$ is singular regarding the speed of the sound of the liquid phase. Furthermore, to assure the continuity of the speed of the sound, A has to be close to one. Therefore, A is set to 0.9999.

Chapter 3

Numerical strategy

Contents

3.1 Numerical methods **65**
3.1.1 System of equations 65
3.1.2 Time integration 67
3.1.3 Spatial discretisation 68
3.1.4 Low Mach number preconditioning 70
3.1.5 Boundary conditions 71
3.1.6 Source term 73
3.2 Software caviflow **73**
3.2.1 Code development 73
3.2.2 Scalability study 74
3.3 Non-cavitating flow validation **76**
3.3.1 RANS 2-D hump flow simulation 77
3.3.2 RANS 3D hump simulation 82
3.4 2-D cavitating flow study using RANS **84**
3.4.1 Numerical centered scheme selection 84
3.4.2 Turbulence model selection 86

3.1 Numerical methods

3.1.1 System of equations

For the sake of simplicity, the present chapter does not represent the averaged proprieties using the $\overline{(\cdot)}$ and $\tilde{(\cdot)}$ notation as previously described. However, the reader must keep in mind that the formulation here presented is well filtered and the variables are written using Favre and Reynolds averages.

The global system is the four-equation model coupled with the turbulence model:

$$\frac{\partial \boldsymbol{w}}{\partial t} + \boldsymbol{\nabla} \cdot [\boldsymbol{F}_c(\boldsymbol{w}) - \boldsymbol{F}_v(\boldsymbol{w})] = \boldsymbol{S}(\boldsymbol{w}), \tag{3.1}$$

with

$$\boldsymbol{w} = \begin{pmatrix} \rho_m \\ \rho_m u_{m,i} \\ \rho_m E_m \\ \alpha \\ \rho_m \psi_k \end{pmatrix}, \ \boldsymbol{F}_v = \begin{pmatrix} 0 \\ \sigma_{m,ij} + \tau_{m,ij} \\ (\sigma_{m,ij} + \tau_{m,ij}) u_{m,j} - q_{m,j} - q^t_{m,j} \\ 0 \\ \left(\mu_m + \dfrac{\mu^t_m}{\sigma_{\psi_k}}\right) \dfrac{\partial \psi_k}{\partial x_j} \end{pmatrix},$$

$$\boldsymbol{F}_c = \begin{pmatrix} \rho_m u_{m,j} \\ \rho_m u_{m,i} u_{m,j} + p_m \\ \rho_m E_m + p_m \\ \alpha u_{m,j} \\ \rho_m \psi_k u_{m,j} \end{pmatrix}, \ \boldsymbol{S} = \begin{pmatrix} 0 \\ 0 \\ 0 \\ (K + \alpha) \dfrac{\partial u_{m,j}}{\partial x_j} + \dfrac{\dot{m}}{\rho_I} \\ C_{\psi_k} \end{pmatrix}.$$

The variable ψ_k depends on the choice of the turbulence model of k equations. The turbulent source terms C_{ψ_k} and the constant σ_{ψ_k} also relies on this model.

The numerical solution of the system Eq. (3.1) is based on the finite volume method. It consists of dividing the 3-D computational domain into cells and computing the vector $\boldsymbol{w}$ in each cell by integrating over the cell volume. To this end, the variables are considered as defined in the centre of the cell. The formulation is simplified to a surface integration using the Green-Ostrogradski theorem (or Gauss theorem):

$$\int_{\mathcal{V}} \frac{\partial \boldsymbol{F}_c(\boldsymbol{w})}{\partial x_j} d\mathcal{V} = \int_{\mathcal{S}} \boldsymbol{F}_c(\boldsymbol{w}) n_j d\mathcal{S}, \tag{3.2}$$

where n_j is the surface normal in the direction j. The choice of an explicit discretisation of Eq. (3.1) leads to the computation of $\boldsymbol{w}$ at time t^{n+1} using the numerical fluxes at time t^n. Nonetheless, in an implicit approach, the numerical fluxes are considered at time t^{n+1} and it requires a linearization that generates a band matrix on the left hand side of the system of equations. The solution of such a linear system is more expensive than the explicit approach. An iterative matrix-free method can be employed to reduce the computational costs of the implicit scheme.

3.1.2 Time integration

Two time-marching schemes are used to compute the unsteady flow. One is based on a two-step implicit formulation called dual time-stepping, and the other is an explicit formulation using a global time step.

3.1.2.1 Dual time-stepping integration

Implicit methods are usually used to save computational time by using a greater time step than explicit methods. That is why the dual time-stepping method was first selected for the computation of sheet cavitation problems. This approach consists of creating a steady-state problem at each physical time step Δt. Therefore, an artificial time τ is introduced within each physical time step. First, a second-order discretisation in time is applied to the implicit scheme. Then, the artificial time derivative term is added to the system. Hence, the switch from one physical iteration to another requires the resolution of the steady-state system by iterating over the artificial time step. The dual time-stepping numerical discretisation is then:

$$\frac{\boldsymbol{w}_{i,j}^{n,m+1} - \boldsymbol{w}_{i,j}^{n,m}}{\Delta\tau} + \frac{3\boldsymbol{w}_{i,j}^{n,m+1} - 4\boldsymbol{w}_{i,j}^{n} + \boldsymbol{w}_{i,j}^{n-1}}{2\Delta t} + \left(\frac{\delta_1(\boldsymbol{F}_{c_x} - \boldsymbol{F}_{v_x})}{\delta_x} + \frac{\delta_2(\boldsymbol{F}_{c_y} - \boldsymbol{F}_{v_y})}{\delta_y}\right)_{i,j}^{n,m+1} = \boldsymbol{S}_{i,j}^{n}. \quad (3.3)$$

This formulation adds to the physical step n over the physical time the sub-steps m of the pseudo time step $\Delta\tau$. Then, the resolution progresses from one physical iteration to another when the stepping process over the artificial time reaches a residue criterion or a limited number of stepping. Nevertheless, a sufficient residue convergence is necessary to assume the reliability of the unsteady solution. It has to be noticed that the artificial time step $\Delta\tau$ is defined locally for each cell.

3.1.2.2 Global time-stepping

A most direct method consists of discretising the time derivative using a global time-stepping formulation. The time step Δt used for the computation is then defined globally. In the present, a third-order Strong Stability Preserving Runge-Kutta method (SSPRK3), described by Spiteri & Ruuth (2002) and Gottlieb (2005), is used as a time-marching scheme. The Butcher's table 3.1 is provided below. It could be used either with an explicit or an implicit approach.

0	0	0	0
1	1	0	0
1/2	1/4	1/4	0
	1/6	1/6	2/3

Table 3.1: Butcher's table for SSPRK3

3.1.2.2.1 Explicit In an explicit formulation, the time step Δt is smaller than for an implicit one. Nevertheless, the computational cost of a time step calculation is rather small. The explicit equation is given by

$$\boldsymbol{w}^{n+1} = \boldsymbol{w}^n + h\left(\frac{1}{6}\boldsymbol{k}_1 + \frac{1}{6}\boldsymbol{k}_2 + \frac{2}{3}\boldsymbol{k}_3\right), \tag{3.4}$$

with

$$\begin{cases} \boldsymbol{k}_1 &= \boldsymbol{F}(t_n, \boldsymbol{w}_n), \\ \boldsymbol{k}_2 &= \boldsymbol{F}(t_n + h, \boldsymbol{w}_n + h\boldsymbol{k}_1), \\ \boldsymbol{k}_3 &= \boldsymbol{F}(t_n + \frac{h}{2}, \boldsymbol{w}_n + \frac{h}{4}(\boldsymbol{k}_1 + \boldsymbol{k}_2)), \end{cases}$$

in which h is the time-step and $\boldsymbol{F}$ represents the numerical fluxes and the source terms of Eq. (3.1).

3.1.2.2.2 Implicit A semi-implicit version of the SSPRK3 scheme is given by:

$$\begin{cases} \boldsymbol{w}_1 &= \boldsymbol{w}_0 + h\boldsymbol{F}(\boldsymbol{w}_1), \\ \boldsymbol{w}_2 &= \frac{3}{4}\boldsymbol{w}_0 + \frac{1}{4}(\boldsymbol{w}_1 + h\boldsymbol{F}(\boldsymbol{w}_2)), \\ \boldsymbol{w}_3 &= \frac{1}{3}\boldsymbol{w}_0 + \frac{2}{3}(\boldsymbol{w}_2 + h\boldsymbol{F}(\boldsymbol{w}_3)). \end{cases}$$

For each Runge-Kutta step, an implicit matrix-free resolution is computed using the line Jacobi method. Nonetheless, the matrix-free formulation implies an accuracy reduction compared to the explicit one.

3.1.3 Spatial discretisation

For stiff problems like sheet cavitation modelled with a 1-fluid method, it is useful to calculate the numerical fluxes using a centered scheme coupled with an artificial dissipative term. Two numerical schemes are selected for the study.

3.1.3.1 Second order Jameson-Schmidt-Turkel

The Jameson-Schmidt-Turkel (JST) scheme is a second-order scheme proposed by Jameson *et al.* (1981). It is composed of a second-order centered scheme and a dissipation term:

$$\boldsymbol{F}_{c_{i+\frac{1}{2},j}} = \frac{1}{2}(\boldsymbol{F}_{c_{i+1,j}} + \boldsymbol{F}_{c_{i,j}}) - D_{1_{i+\frac{1}{2},j}}(\boldsymbol{w}_{i+1,j} - \boldsymbol{w}_{i,j}) \tag{3.5}$$

In this 2-D example, the flux is computed on the interface $i + \frac{1}{2}$ in the x direction. The term D_1 represents the dissipation separated in two parts. The first part is a second-order dissipation based on a pressure sensor η_i and the second part is a four-order dissipation. It can be written, for the current example, as:

$$\begin{aligned} D_{i+1/2,j}(\boldsymbol{w}_{i+1,j} - \boldsymbol{w}_{i,j}) &= \epsilon^{(2)}_{i+1/2,j}\rho(\boldsymbol{A}_{i+1/2,j})(\boldsymbol{w}_{i+1,j} - \boldsymbol{w}_{i,j}) \\ &\quad - \epsilon^{(4)}_{i+1/2,j}\rho(\boldsymbol{A}_{i+1/2,j})(\boldsymbol{w}_{i+2,j} - 3\boldsymbol{w}_{i+1,j} + 3\boldsymbol{w}_{i,j} - \boldsymbol{w}_{i-1,j}), \end{aligned} \quad (3.6)$$

with $\rho(\boldsymbol{A}_{i+1/2,j})$ the spectral radius of the Jacobian matrix $\boldsymbol{A}$. The term $\epsilon^{(2)}_{i+1/2,j}$ is defined with a parameter $k^{(2)} \in [0, 1]$ and the pressure sensor η_i:

$$\begin{aligned} {\epsilon^{(2)}}_{i+\frac{1}{2},j} &= k^{(2)}\max[\eta_i; \eta_{i+1}], \\ \eta_i &= \frac{|p_{i+1} - 2p_i + p_{i-1}|}{p_{i+1} + 2p_i + p_{i-1}}. \end{aligned}$$

This sensor allows triggering the second-order dissipation only around high-pressure gradients. The term $\epsilon^{(4)}_{i+1/2,j}$ is defined with a parameter $k^{(4)} \in [0.008, 0.064]$ and allows to damp small oscillation far from shocks:

$${\epsilon^{(4)}}_{i+\frac{1}{2},j} = \max\left[0, k^{(4)} - \epsilon^2_{i+\frac{1}{2},j}\right]$$

3.1.3.2 Third-order Jameson-Schmidt-Turkel

The second-order centered scheme could be updated to a fourth-order one:

$$\boldsymbol{F}_{c_{i+\frac{1}{2},j}} = \frac{1}{12}(-\boldsymbol{F}_{c_{i+2,j}} + 7\boldsymbol{F}_{c_{i+1,j}} + 7\boldsymbol{F}_{c_{i,j}} - \boldsymbol{F}_{c_{i-1,j}}). \quad (3.7)$$

The global numerical scheme (centered part plus dissipation) is, therefore, a third-order one.

3.1.3.3 Dissipation modification of Jameson-Schmidt-Turkel schemes

In a two-phase flow modelling using a one-fluid flow hypothesis, high-density gradients appear along with the interface between liquid and vapour. A third term is added to the dissipation to prevent computational problems. The same formula that the $\epsilon^{(2)}$ is used but with another sensor $\eta_i^{(I)}$ based on the density:

$$\eta_i^{(I)} = \frac{|\rho_{i+1} - 2\rho_i + \rho_{i-1}|}{\rho_{i+1} + 2\rho_i + \rho_{i-1}}. \quad (3.8)$$

Hence, the dissipation term $\epsilon^{(2)}_{i+1/2,j}$ can be written as the sum of dissipations around shocks and interfaces. Both terms uses their own constant $k^{(2)}$ and $k^{(2)}_I$:

$$\epsilon^{(2)}_{i+1/2,j} = \epsilon^{(2)\ shock}_{i+1/2,j} + \epsilon^{(2)\ interface}_{i+1/2,j},$$

with

$$\begin{aligned} \epsilon^{(2)\ shock}_{i+1/2,j} &= k^{(2)} \max[\nu_i, \nu_{i+1}], \\ \epsilon^{(2)\ interface}_{i+1/2,j} &= k^{(2a)} \max[\nu^{(I)}_i, \nu^{(I)}_{i+1}]. \end{aligned}$$

The term $k^{(2a)}$ is chosen independently to the selection of the constant $k^{(2)}$.

3.1.4 Low Mach number preconditioning

The system of equations is developed considering a compressible hypothesis. However, incompressible areas within the cavitating Venturi flow are identified with low Mach numbers. Therefore, it is necessary to use a low Mach number preconditioning method to deal with numerical errors and stiffness of the equation system. A preconditioning matrix is computed based on the work of Turkel (1987) using a β all-speed flow parameter proportional to the Mach number. The matrix is presented below written for the primitive variable vector $\boldsymbol{w_p} = (p, u, e, \alpha)$:

$$\boldsymbol{P}_p^{-1} = \begin{pmatrix} \frac{1}{\beta^2} & 0 & 0 & 0 \\ 0 & 1 & 0 & 0 \\ 0 & 0 & 1 & 0 \\ 0 & 0 & 0 & 1 \end{pmatrix}.$$

It is then possible to return to the vector of conservative variables using a passing relation. The formulation of the β parameter suggested by Choi & Merkle (1993) is:

$$\beta^2 = \min[\max(M^2, \theta M_\infty^2), 1], \tag{3.9}$$

where M and M_∞ stand for the Mach number and the far-field Mach number, respectively. Thus, no preconditioning is applied when the Mach number is greater than 1 (with $\beta^2 = 1$). In contrast, the preconditioning is applied and controlled using the θ limiter in low Mach areas. In the present, the constant θ is set to 3.

In the case of a dual time stepping formulation, the preconditioning matrix is applied to the artificial time derivative to accelerate the reach of the steady-state. Nevertheless, the preconditioning can be applied only on the dissipation terms to preserve the time discretisation consistency in the case of a global time-stepping resolution. The problem formulation is then kept unchanged.

3.1.5 Boundary conditions

The venturi-type geometry configuration used for the study involves wall and inlet/outlet boundary conditions. Modelling a turbulent flow within a wall requires a very refined mesh to catch the strong velocity gradient in the normal direction to the wall. The computation of such flow implies a substantial computational cost and is not suitable in RANS or Hybrid formulations. Nevertheless, boundary layer development is a well-known problem, and the estimation of the boundary layer profile can be completed using a wall function. Then, the inlet/outlet boundary conditions can be computed using Euler characteristic equations.

3.1.5.1 Wall function

The wall function is defined using two non-dimensional parameters u^+ and y^+:

$$u^+ = \frac{u}{u_\tau} \quad \text{and} \quad y^+ = \frac{y u_\tau}{\nu_w} \quad \text{with } u_\tau = \sqrt{\frac{\tau_w}{\rho_w}}, \tag{3.10}$$

where y is the wall distance, ν_w is the viscosity at the wall, ρ_w the density at the wall and τ_w the wall friction. The velocity profile is then described by the following equations over u^+:

$$\begin{aligned} u^+ &= y^+ && \text{if} \quad y^+ < 11.13, \\ u^+ &= \frac{1}{\kappa} \ln y^+ + 5.25 && \text{if} \quad y^+ > 11.13, \end{aligned} \tag{3.11}$$

with the Von Karman constant $\kappa = 0.41$. The first equation characterises the linear law corresponding to the laminar sublayer, and the second one defines the logarithmic law linked to the turbulent boundary layer. The y^+ value of 11.13 corresponds to the link between both layers. This no-slip boundary condition combined with the adiabatic hypothesis for walls results in normal derivatives of the void ratio, the density and the pressure set to zero at the wall boundary. This function is implemented into the software to compute the wall friction in the first cell in the concerned wall direction. The first step is to compute $u^+y^+ = yu/\nu_w$ and compare the value with the square of the threshold. If u^+y^+ is smaller than it, the linear formulation is used, and the computation of the wall friction is

direct. Nevertheless, in the case of u^+y^+ bigger than the threshold, the calculation of the wall friction requires an initialisation with the linear one followed by an iteration process to approach the correct value using the logarithmic law. The use of the wall function can be summed up as

$$\begin{aligned} \tau_w &= \frac{u\mu_w}{y} & \text{if} \quad u^+y^+ < 11.13^2, \\ \tau_w^{n+1} &= u^2\rho_w \left(\frac{1}{\kappa}\ln(\tfrac{y\sqrt{\rho_w\tau_w^n}}{\mu_w}) + 5.25\right)^{-2} & \text{if} \quad u^+y^+ > 11.13^2, \end{aligned} \tag{3.12}$$

where τ_w^{n+1} is the upgrade of τ_w^n in the iterative process. In the software, the number of steps is set to ten.

3.1.5.2 Inlet and outlet boundaries

3.1.5.2.1 Characteristic relations The treatment of the domain's inlet and outlet boundary conditions is based on the use of the characteristic relations associated with the hyperbolic system of Euler's equations, the description of the method is given by Hirsch (1988, 1990). Then, the system is developed, including the preconditioning:

$$\begin{aligned} -c^2(\rho^b - \rho^s) + (P^b - P^s) &= 0, \\ v^b - v^s &= 0, \\ \rho(\alpha^b - \alpha^s) - K(\rho^b - \rho^s) &= 0, \\ (\lambda_+ - u)(P^b - P^s) + \rho\beta^2c^2(u^b - u^s) &= 0, \\ (\lambda_- - u)(P^b - P^s) + \rho\beta^2c^2(u^b - u^s) &= 0, \end{aligned} \tag{3.13}$$

where b index stands for boundary variables and s index stands for variables computed with the numerical scheme. $\lambda_\pm$ are the highest and the lowest eigenvalues of the preconditioning system. Both the inlet and outlet boundaries are considered subsonic. Therefore, the void ratio α, the phase density ρ_k and the velocity components are imposed at the inlet. Then, the pressure is computed using the characteristic equations. For the outlet boundary, the static pressure is selected while other variables are calculated using this system.

3.1.5.3 Turbulent field

The turbulent quantities used in the selected model have to be set at the boundary. That is why the far-field variables are set for the inlet and the outlet boundaries.

3.1.6 Source term

The source terms processing is divided into two parts. The first one, from the void ratio transport equation, is explicitly computed. The second one, from the turbulence equations, is obtained by an implicit matrix-free formulation.

3.2 Software caviflow

3.2.1 Code development

The *Fortran90* software Caviflow is selected for the current work. It was used in multiple studies carried out by Goncalves, Decaix or Charrière (Goncalvès & Decaix, 2012; Decaix & Goncalves, 2012; Charrière *et al.*, 2015). The software was parallelised right before the beginning of the PhD thesis. After running test cases, problems were identified for which some software corrections and extensions were required to improve the computation accuracy. Only the major software modifications are depicted in the manuscript. A check-up of the MPI communications revealed a memory leak. The communications were then totally re-written using nonblocking communications tools (MPI_ISEND, MIP_IRECV, ...). Hence, the MPI communications are faster than before the modifications.

Furthermore, the software used to allow only one layer of ghost cells around the sub-domains. It presents a problem for the internal interface between sub-domains. The numerical scheme selected for the computation could need to use a larger stencil than one layer cell. Therefore, to prevent an accuracy reduction for high order numerical schemes, the software is adjusted to generate the number of layers requested by the user.

The last adjustment is in the generation of parallel output and restart files, because sequential writing is very time-consuming. Moreover, some useful tools are developed in *Fortran90* or *python* to facilitate the study of the numerical results.

3.2.2 Scalability study

The software performance is presented in the current section through scalability studies for a Venturi flow simulation. First, the results of a weak scalability study are shown in Fig. 3.1 where the ratio t_0/t_i is plotted in relation to the number of cores used for the computation. The term t_i represents the computational time required for a time step calculation with 2^i cores, and t_0 stands for the computational time of a time step in sequential. Table 3.2 displays the study configuration regarding the MPI cutting and the mesh size. The number of cells per processor is kept at the constant number of 512000 cells.

Nx	**Ny**	**Nz**	**Number of cells (in M)**	**Number of cores**
320	40	40	0.512	1
320	80	40	1.024	2
320	80	80	2.048	4
640	80	80	4.096	8
640	160	80	8.192	16
640	160	160	16.384	32
1280	160	160	32.768	64
1280	320	160	65.536	128
1280	320	320	131.072	256
2560	320	320	262.144	512
2560	640	320	524.288	1024

Table 3.2: Weak stability study configuration.

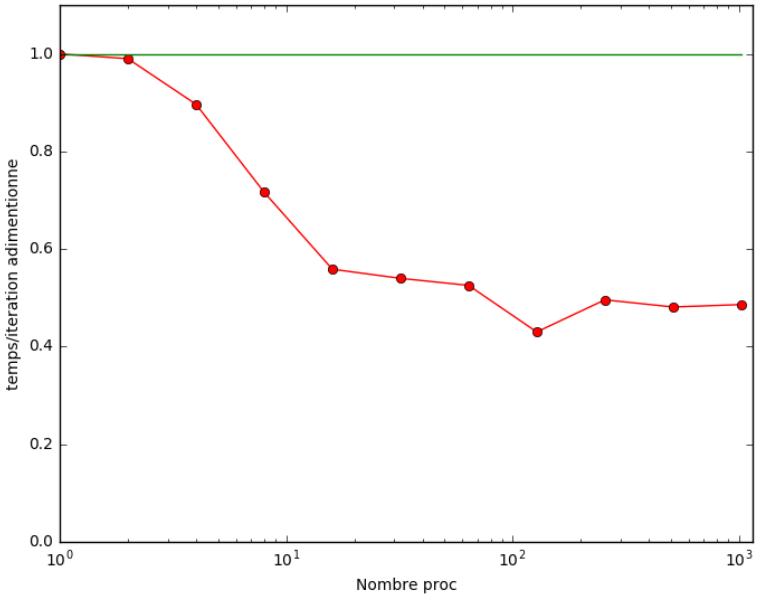

Figure 3.1: Weak scalability study with 512000 cells per core.

The efficiency observed with the weak stability study drops for 4, 8 and 16 cores but steadies around 50% for bigger cases. Despite that the paralleling is not entirely optimal yet, it underlines a correct implementation of the MPI process.

Thereafter, a strong stability study is carried out for three meshes presented in Tab. 3.3. A ratio between the computational time per time step for the minimum number of cores t_0 and the other one for the number of selected cores t_i is introduced It is called the speedup t_0/t_i. Then, the efficiency is defined as the ratio of the speedup and the selected number of cores: $t_0/(t_i 2^i)$. The results are presented in Fig. 3.2, where the speedup is displayed using a logarithmic scale for the sake of visibility. The results of the study show that, despite all the modifications made, the software CAVIFLOW is not fully optimised from a parallel point of view. Nevertheless, the software demonstrates robustness to run on meshes of consequent size with a significant number of processors.

Cas n°	Cas 1	Cas 2	Cas 3
Number of cells (in M)	16.384	65.536	131.072
Minimum number of cores	1	32	64
Maximum number of cores	1024	1024	2048

Table 3.3: Strong scalability study configuration.

All the calculations for this study were carried out on the Occigen computing cluster hosted at CINES. The maximum number of cores per node has been fixed at 16, and the memory per node is imposed at 64GB. For cases 2 and 3, the memory needed to run on small numbers of cores was insufficient, so the point of start of the strong scalability study is set to respectively 32 and 64 cores.

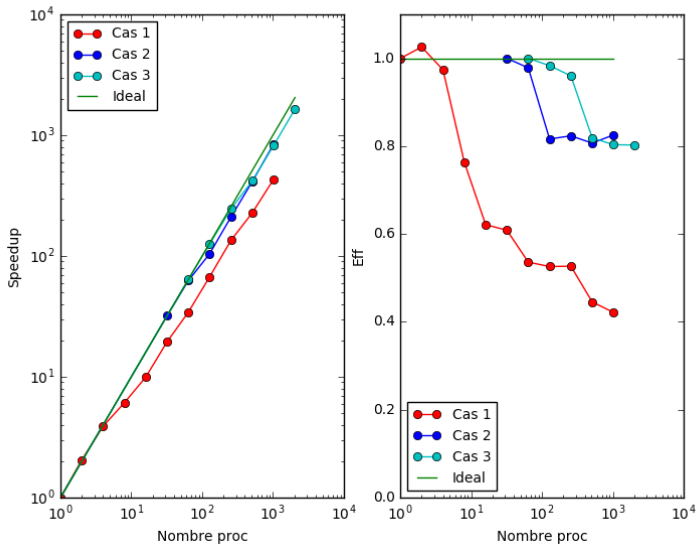

Figure 3.2: Strong scalability study.

3.3 Non-cavitating flow validation

A non-cavitating detached flow simulation is first selected to validate the software. The NASA hump case (`https://turbmodels.larc.nasa.gov/nasahump_val.html`) based on the experiment of Greenblatt *et al.* (2006) is then chosen due to the closeness with the Venturi flow and to the large quantity of available data. The geometry is presented in Fig. 3.3 and corresponds to a non-symmetrical bump with a chord length of $L_{chord} = 0.42m$. The upper wall of the domain is slightly modified (moved

downwards) in the area above the hump in order to compensate the blockage effect of the endplates, as suggested on the NASA website. The farfield velocity is $U_\infty = 34.6 m.s^{-1}$ and the chord Reynolds number is $Re_{chord} = \frac{U_\infty L_{chord}}{\nu} = 9.36 \times 10^5$. The inflow boundary condition is computed based on the velocity profile extracted during the experiment at $x^* = -2.14$, and on the velocity fluctuations for the turbulence quantities: for Spalart-Allmaras with $\tilde{\nu} = \sqrt{2.5} u' \ell_{char}$; for $k - \ell$ with $k = 2.5 u'^2$ and $\ell = \frac{\sqrt{2}\mu_t^{init}}{u'}$, where $\ell_{char} = 0.4\delta_{99}$ is the characteristic length, δ_{99} stands for the boundary layer thickness and $\mu_t^{init} = 10^{-4}$ is the initial turbulent viscosity.

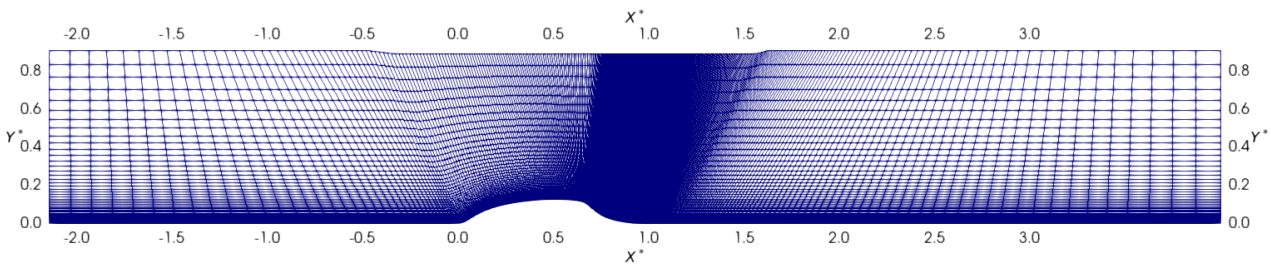

Figure 3.3: NASA hump mesh and geometry.

3.3.1 RANS 2-D hump flow simulation

Firsts computations are carried out using a 2-D configuration with a mesh of 385×109 cells (Fig. 3.3) extracted from the NASA website. The mesh is refined close to the wall in such a way that y^+ is close to 0.1. A second mesh is made to validate the use of the wall function with 385×88 cells for which y^+ is around 15. The experimental data and the available data computed with the CFD code CFL3D are compared with the results of the current simulations. The CFL3D results obtained with the Spalart-Allmaras and the $k - k\ell$ models are selected. Figure 3.4 shows the streamwise velocity field computed with the Spalart-Allmaras model. The flow separation is correctly observed downstream the bump. Table 3.4 gathers the location of the flow separation and the reattachment for the experiment and the numerical simulations. For the separation location, the results of the present computations are in correct agreement with the experiment and the numerical references. The reattachment location obtained with the current computations is even closer to the one observed in the experiment than the one extracted in both numerical references.

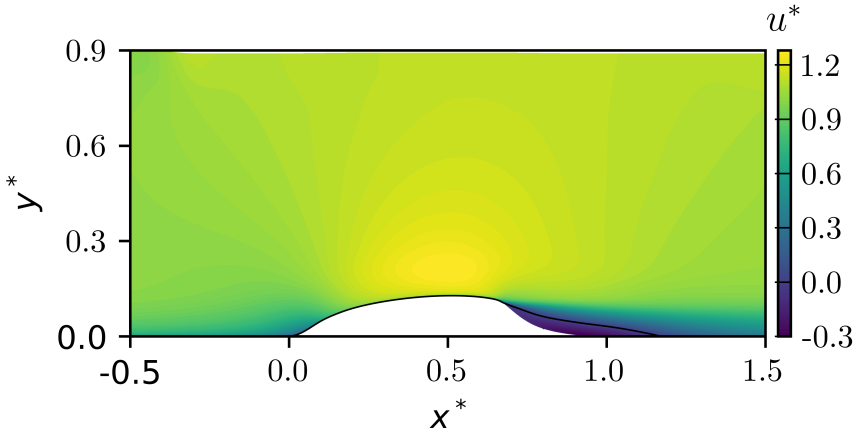

Figure 3.4: Visualisation of the streamwise velocity with a contour $u^* = 0$ for the computation using Spalart-Allmaras model.

Case	**Flow separation** (x/L_{chord})	**Reattachment** (x/L_{chord})
experiment	0.665	1.1
CFL3D Spalart-Allmaras	0.661	1.26 – 1.27
CFL3D $k - k\ell$	0.658	1.24
Spalart-Allmaras	0.659	1.13
Spalart-Allmaras with wall law	0.675	1.17
$k - \ell$	0.659	1.13
$k - \ell$ with wall law	0.669	1.13

Table 3.4: Flow separation and reattachment location for the experimental and the 2-D numerical results.

The velocity profiles are extracted at eight locations upstream, over and downstream the bump to complete the present study. Figures 3.5 and 3.6 present the numerical results using respectively the Spalart-Allmaras and the $k - \ell$ turbulence models. As previously observed, both are in good agreement with the experimental data. The numerical results based on the $k - \ell$ model are closer to the experimental data than those based on the Spalart-Allmaras model. Figure 3.7 shows the data comparison for the case with the wall function previously introduced using the appropriate mesh. The velocity profiles are in great agreement with the experimental data as well. Hence, the use of the wall function combined with the selection of an appropriate mesh does not deteriorate the results.

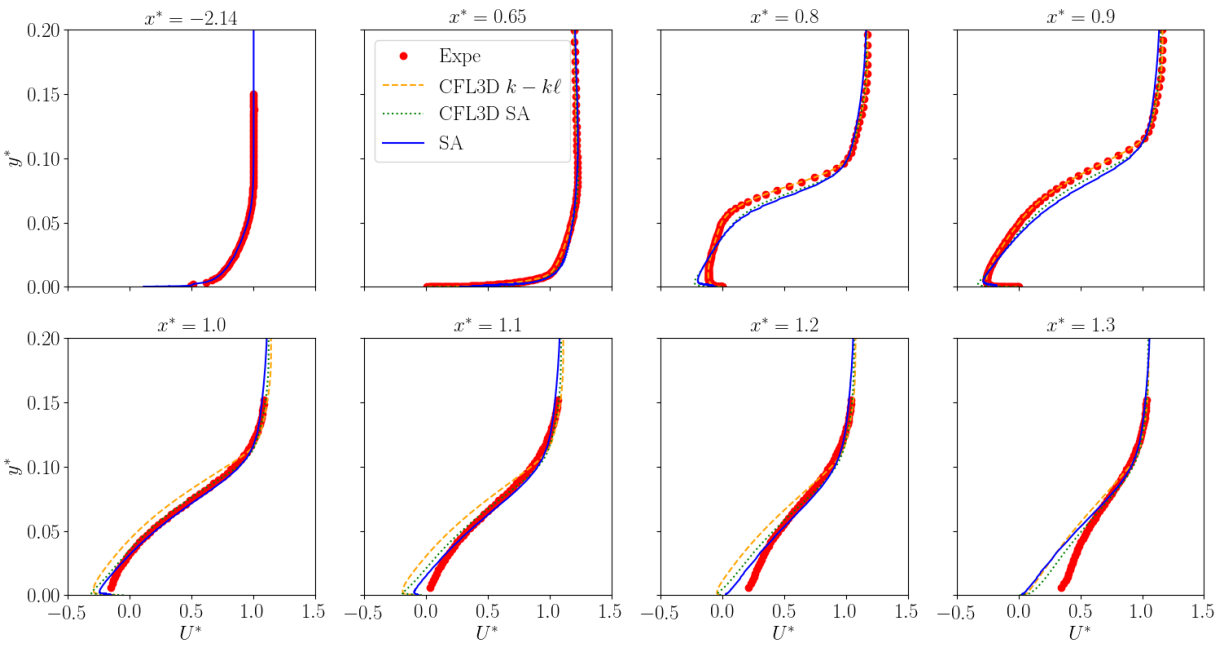

Figure 3.5: Velocity profiles extracted at eight streamwise locations from the experiment, two computational results using the CFL3D software and the results of the current computation with Spalart-Allmaras.

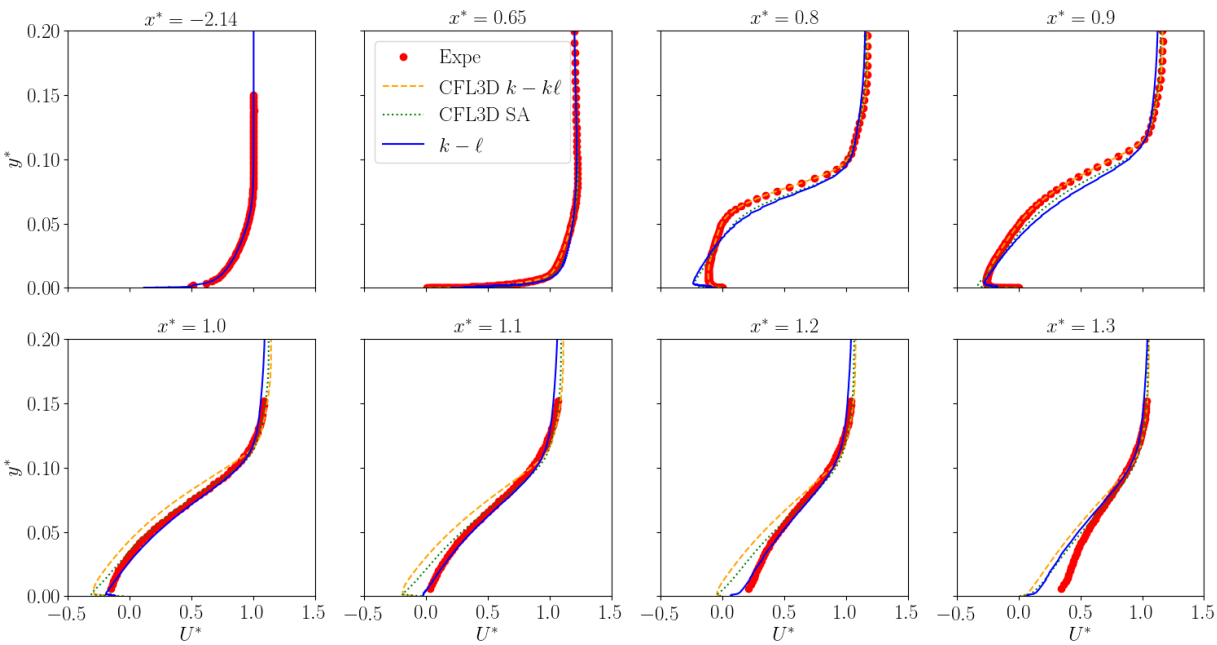

Figure 3.6: Velocity profiles extracted at eight streamwise locations from the experiment, two computational results using the CFL3D software and the results of the current computation with $k - \ell$.

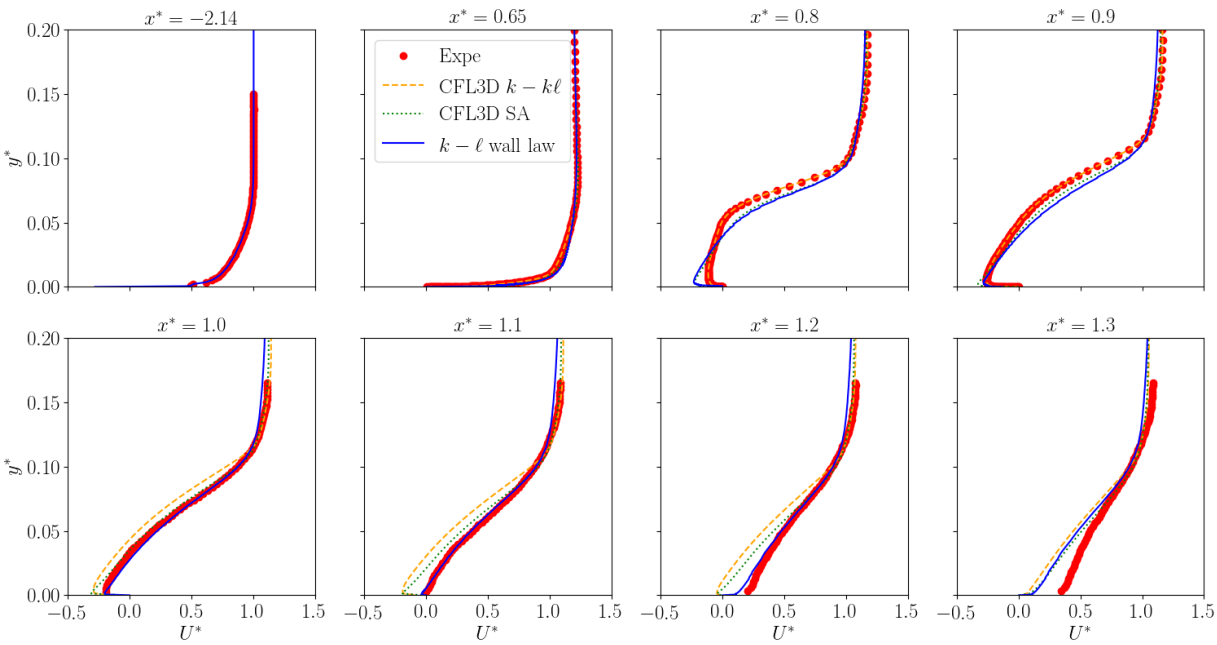

Figure 3.7: Velocity profiles extracted at eight streamwise locations from the experiment, two computational results using the CFL3D software and the results of the current computation with $k - \ell$ using the wall function.

The pressure coefficient is calculated using the formulation:

$$C_P = \frac{p - p_{ref}}{0.5\rho_{ref}u_{ref}^2}, \tag{3.14}$$

where $u_{ref} = 34.6\ m.s^{-1}$, $\rho_{ref} = 1.184\ kg.m^{-3}$ and $p_{ref} = 101324\ Pa$. It is based on the wall pressure extracted from the numerical results along the streamwise direction. Figures 3.8 and 3.9 represent the pressure coefficient along the streamwise axis for computations based respectively on the Spalart-Allmaras and the $k - \ell$ turbulence models. The results are in good accordance with the experiment and the CFL3D computations. Nonetheless, the use of the $k - \ell$ model gives more accurate results for this coefficient. Figure 3.7 depicts the pressure coefficient computed from the simulation with the wall function and the $k - \ell$ model. Once more, the use of the wall function seems not to affect the results.

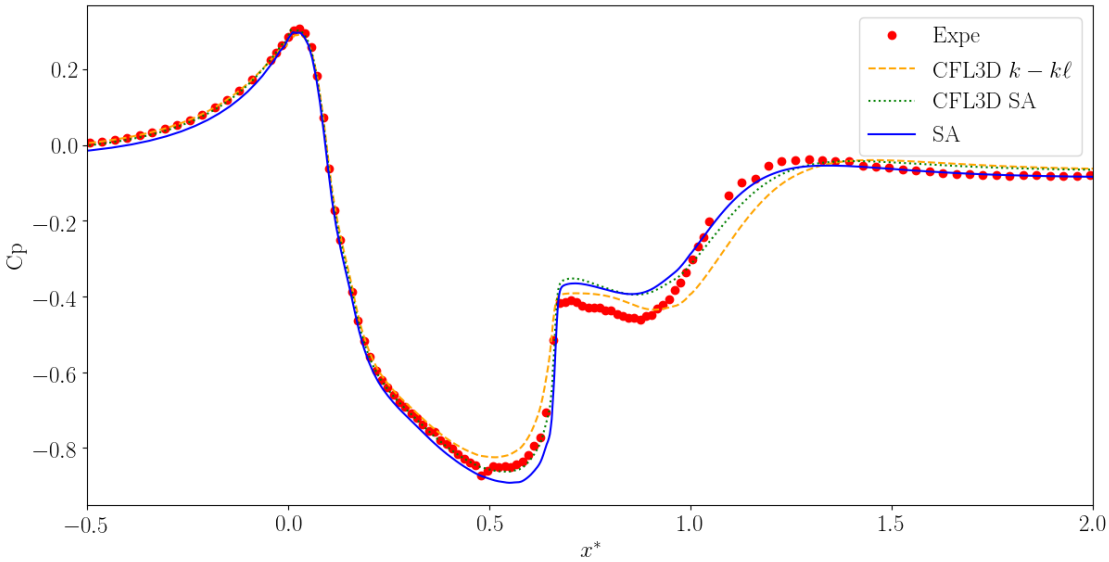

Figure 3.8: Cp profile extracted along the streamwise axis from the experiment, two computational results using the CFL3D software and the results of the current computation with Spalart-Allmaras.

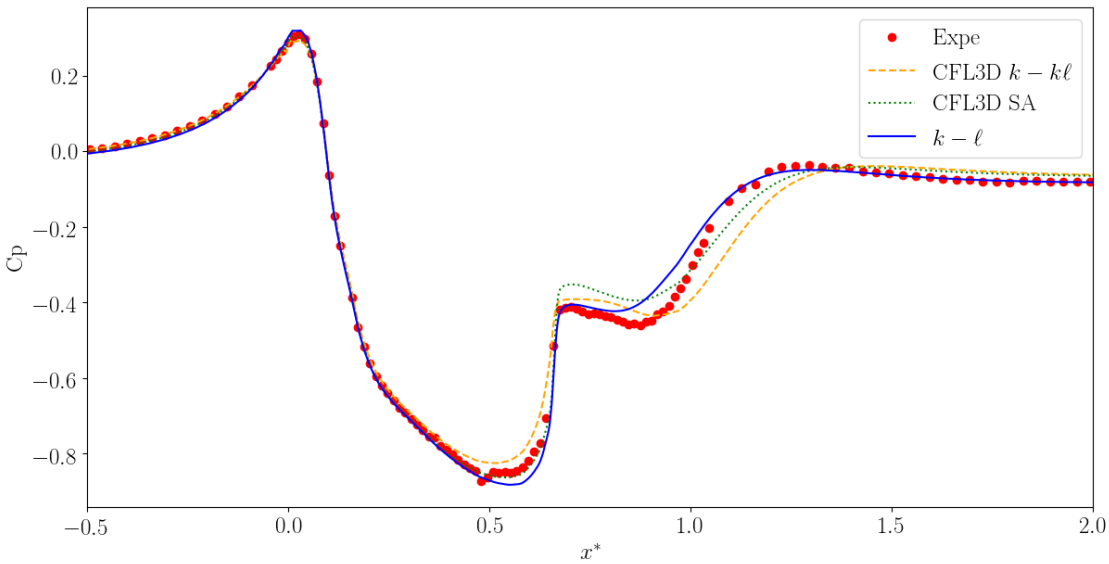

Figure 3.9: Cp profile extracted extracted along the streamwise axis from the experiment, two computational results using the CFL3D software and the results of the current computation with $k-\ell$.

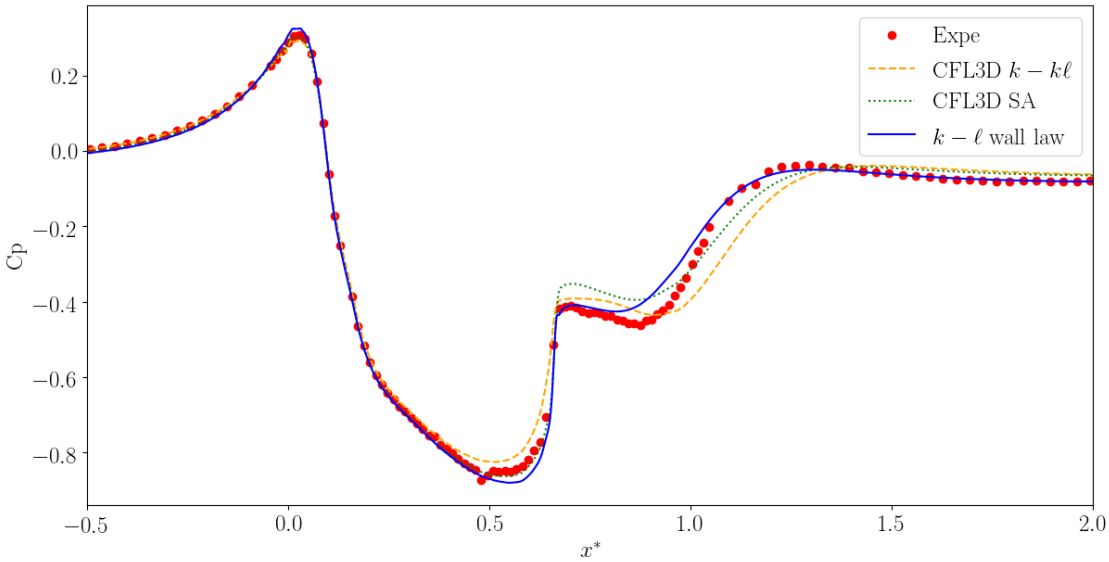

Figure 3.10: Cp profile extracted along the streamwise axis from the experiment, two computational results using the CFL3D software and the results of the current computation with $k-\ell$ using the wall function.

As observed in the 2-D cavitating simulation on the Venturi configuration, the $k-\ell$ model of Smith gives the best results. Therefore, this model is defined as the turbulence model by default for 3-D RANS simulations.

3.3.2 RANS 3D hump simulation

The previous 2-D NASA hump geometry is extended to 3-D by extruding in the spanwise direction up to $0.2L_{chord}$. Periodic boundary conditions are then applied in the spanwise direction. The other boundary conditions are identical to the 2-D case ones. The wall model is employed at the bottom wall, and the grid is built in an appropriately with $y^+ = 15$ at the first cells in the wall-normal direction. The grid is uniformly created in the spanwise direction and refined at locations of interest in the streamwise direction. Figure 3.11 highlights eight velocity profiles upstream, over and downstream the bump. A little discrepancy is identified at $x^* = 0.8$. However, the velocity profiles better fit the experimental data downstream the bump, especially close to the wall at $x^* = 1.1$ and $x^* = 1.2$.

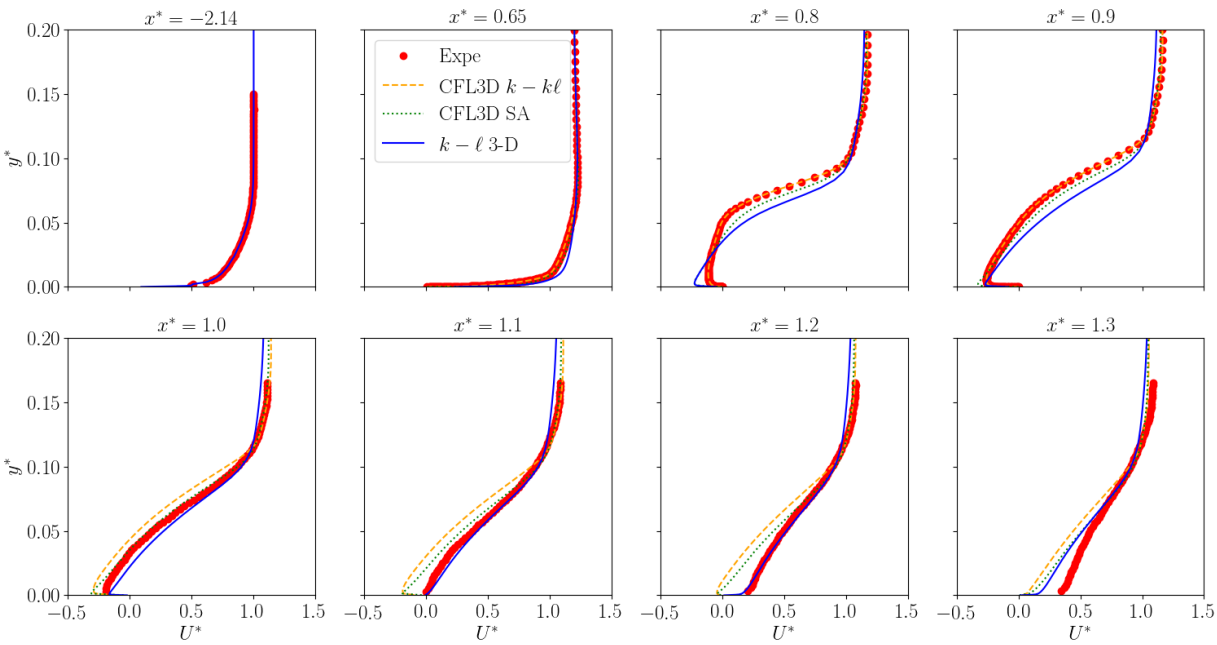

Figure 3.11: Velocity profiles extracted at eight streamwise locations from the experiment, two computational results using the CFL3D software and the 3-D results of the current computation with $k-\ell$ using the wall function.

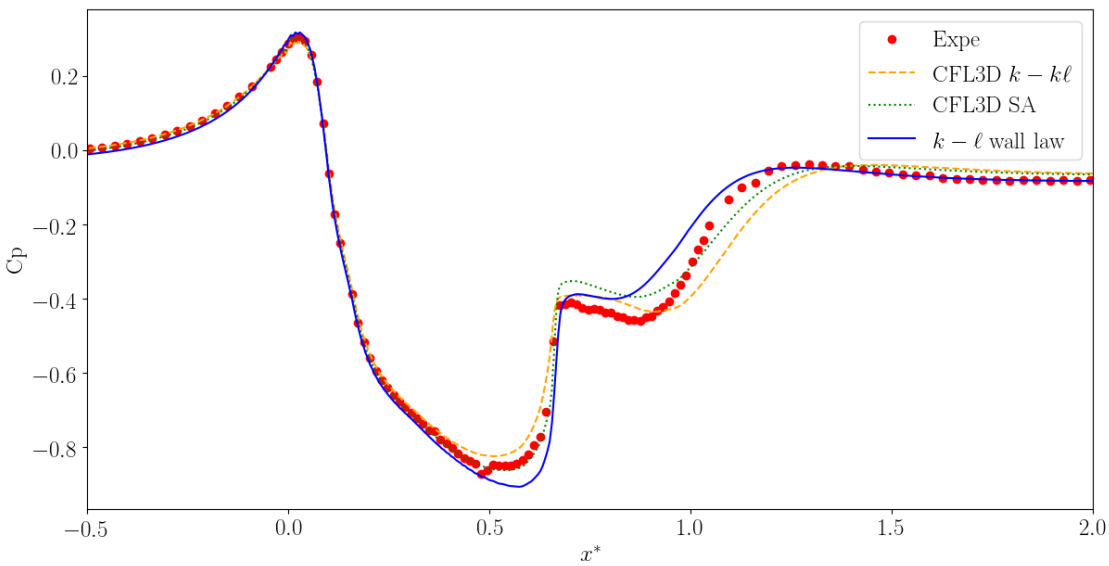

Figure 3.12: Cp profile extracted along the streamwise axis from the experiment, two computational results using the CFL3D software and the 3-D results of the current computation with $k-\ell$ using the wall function.

Figure 3.12 shows the pressure coefficient profile along the longitudinal axis for the 3-D case with a correct agreement with experimental data. Moreover, the detached point is well predicted with the exact location $x^* = 0.665$. Similarly, the re-attached point corresponds to the experimental one at $x^* = 1.1$. The results of the 3-D computation are improved compared to the 2-D computation and are globally in good agreement with the experiment.

3.4 2-D cavitating flow study using RANS

A 2-D Venturi configuration is selected to test different numerical set-up used for sheet cavitation modelling. The geometry is extracted from the one adopted in the experimental study of Barre *et al.* (2009). Unsteady computations using both implicit matrix-free and explicit methods are compared regardings the computational time and the time step. Although the time step is much smaller with the explicit formulation, the computational time for an equivalent physical time computation is almost identical. It is due to the high computational cost per time step with the matrix-free implicit formulation. Moreover, the matrix-free formulation is, by definition, less accurate than the explicit one, which is the chosen method for the unsteady computations.

The choice of the numerical scheme regarding the accuracy order and the turbulence model is discussed in the following.

3.4.1 Numerical centered scheme selection

The development of the Jameson-Schmidt-Turkel scheme at the third-order with the modified dissipation is investigated regarding the classical second-order one. Data are extracted at four locations along the vapour cavity to compare with experimental results. Figures 3.13 and 3.14 present the results extracted at the first two stations and at the last two stations respectively. The comparison is carried out on the void ratio and the streamwise velocity, which both are the most appropriate quantities to study the sheet cavity flow. At station S1, the simulation results using the third-order scheme are slightly closer to the experimental data than those obtained with the second-order scheme for both variables. At location S2, both results differ and can locally better fit than the other one. For the two

last locations S3 and S4, the results computed using both schemes are close and in agreement with the experimental data. Nonetheless, the computation with the third-order scheme slightly better captures both the void ratio and the streamwise velocity. The third-order scheme is thus selected for further computations due to the improvement of the numerical results compared to the second-order one.

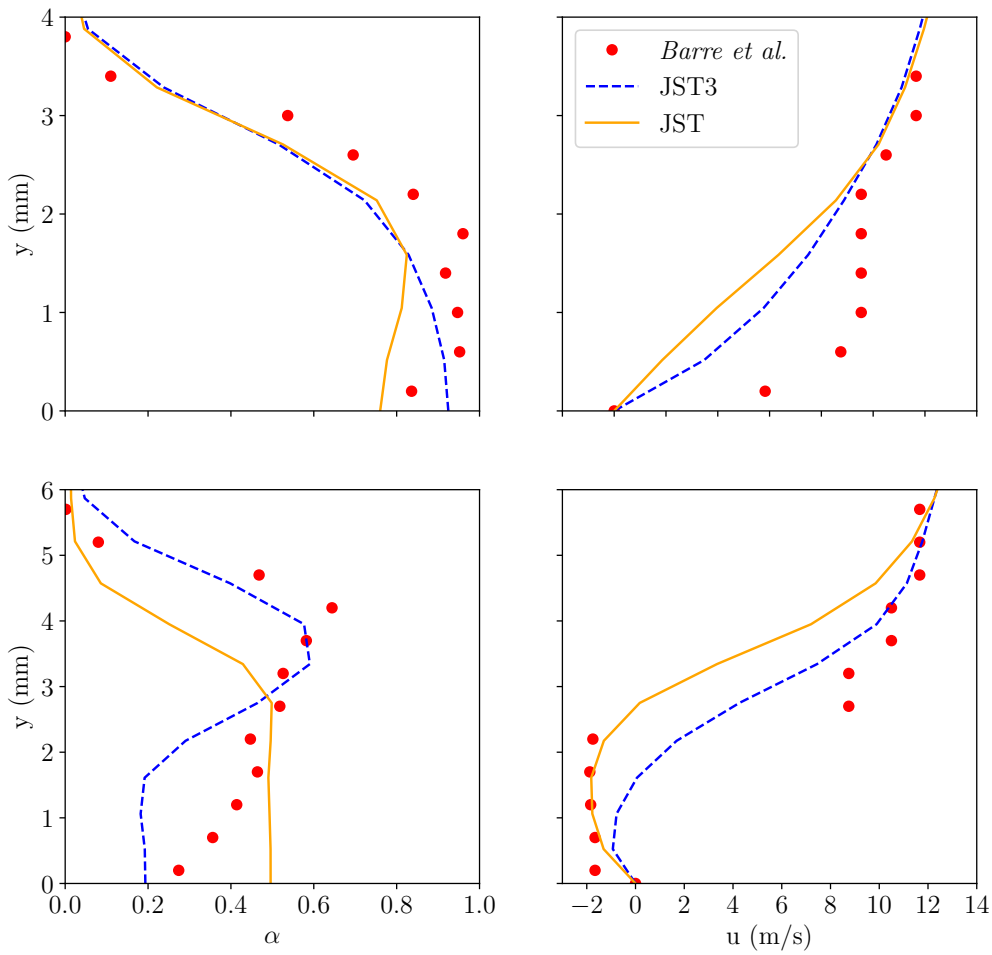

Figure 3.13: Time-averaged comparison between experiment at midspan and numerical 2-D results using second-order Jameson-Schmidt-Turkel (JST) scheme and third-order Jameson-Schmidt-Turkel (JST3) scheme for void ratio (left) and velocity (right) at stations S1 (top) and S2 (bottom).

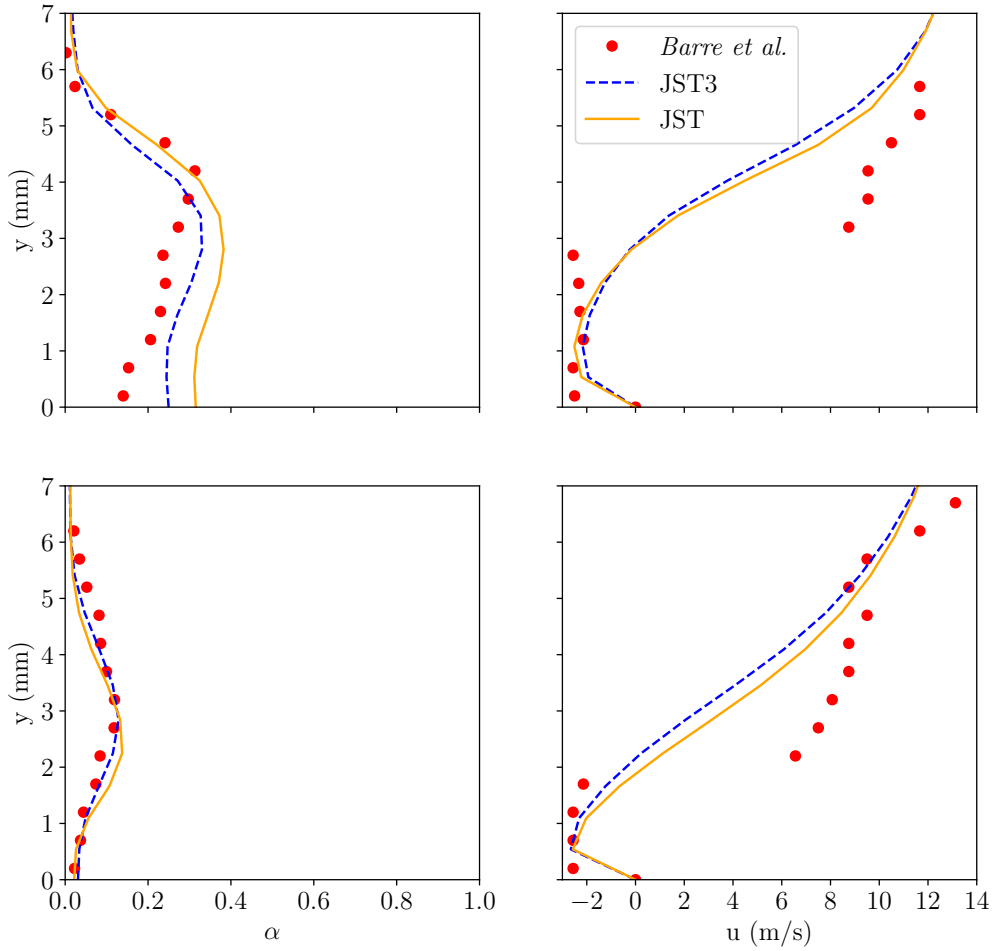

Figure 3.14: Time-averaged comparison between experiment at midspan and numerical 2-D results using second-order Jameson-Schmidt-Turkel (JST) scheme and third-order Jameson-Schmidt-Turkel (JST3) scheme for void ratio (left) and velocity (right) at stations S3 (top) and S4 (bottom).

3.4.2 Turbulence model selection

The choice of the turbulence model was previously investigated by Decaix (2012) and Charrière (2015). Both the Spalart-Allmaras and the $k - \ell$ models presented good results. Nevertheless, a comparative study of these models is carried out to validate the explicit formulation and select the turbulence model for 3-D URANS computations. Figures 3.15 and 3.16 illustrate the comparison of results for both turbulence models and the experiment. Similar profiles are extracted for both simulations at the first two stations S1 and S2, except for the void ratio at S2. It is complicated in this case to identify the model that fits the experimental data best. However, at stations S3 and S4,

the void ratio and velocity profiles of the $k - \ell$ turbulence model are in a better agreement with the experiment than the Spalart-Allmaras ones.

Furthermore, Decaix (2012) and Charrière (2015) employ the implicit formulation for the study of the void ratio and velocity profiles using a range of turbulence models. The use of the explicit formulation in the present, combined with the choice of third-order Jameson-Schmidt-Turkel for the numerical scheme and $k - \ell$ model for turbulence, improves the accuracy of the results compared to those previous studies.

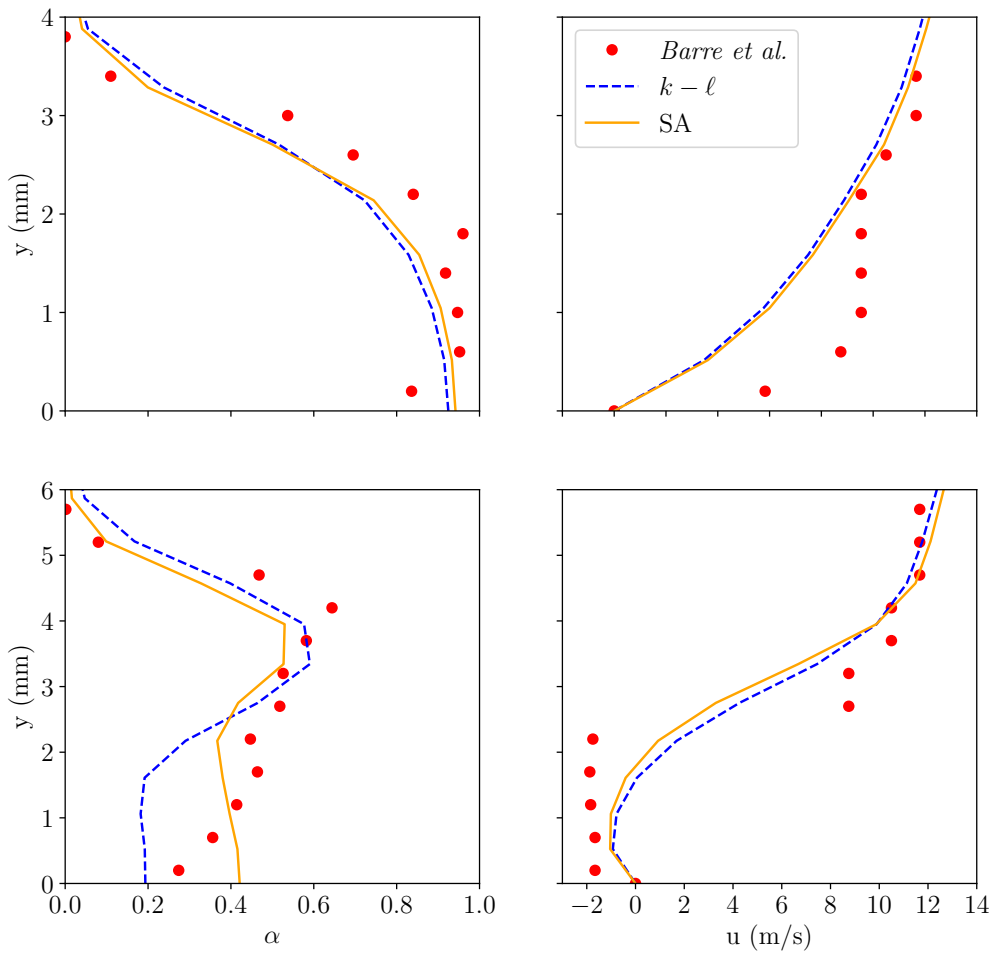

Figure 3.15: Time-averaged comparison between experiment at midspan and numerical 2-D results with $k - \ell$ and Spalart-Allmaras turbulence model for void ratio (left) and velocity (right) at stations S1 (top) and S2 (bottom).

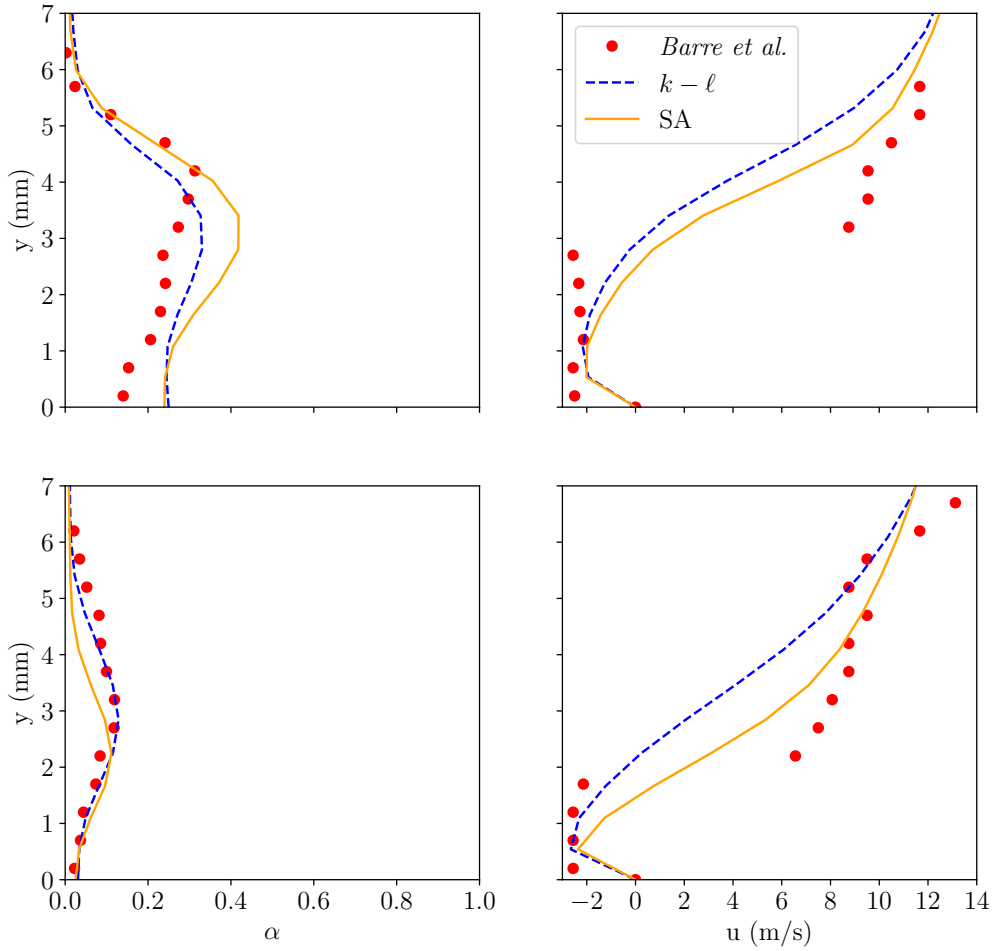

Figure 3.16: Time-averaged comparison between experiment at midspan and numerical 2-D results with $k-\ell$ and Spalart-Allmaras turbulence model for void ratio (left) and velocity (right) at stations S3 (top) and S4 (bottom).

Chapter 4

URANS simulation of a sheet cavitation flow within a 4° divergence angle Venturi configuration

Contents

4.1 Venturi configuration and comparison . . . 89
4.1.1 Case set up . . . 90
4.1.2 Comparison with experimental data . . . 91
4.2 Global behaviour . . . 94
4.2.1 Time-averaged data analysis . . . 94
4.2.2 Dynamic analysis . . . 96
4.3 Re-entrant jet . . . 102
4.4 Modal decomposition analysis . . . 104
4.5 Discussion . . . 109
4.6 Conclusion . . . 111

4.1 Venturi configuration and comparison

The present section is devoted to introduce the studied case and to compare numerical results with experimental data. Previous computations and comparisons with literature using the current cavitation model, for different configurations (expansion tube, underwater explosion with cavitation, compression of a vapour bubble, Venturis, shock tubes, ...), has already been published (Goncalvès, 2013; Goncalvès & Charrière, 2014; Charrière *et al.*, 2015; Goncalves & Zeidan, 2018).

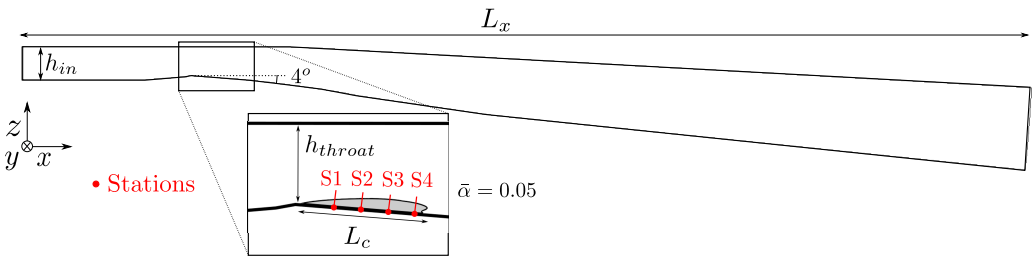

Figure 4.1: Schematic view of the Venturi used in the computation.

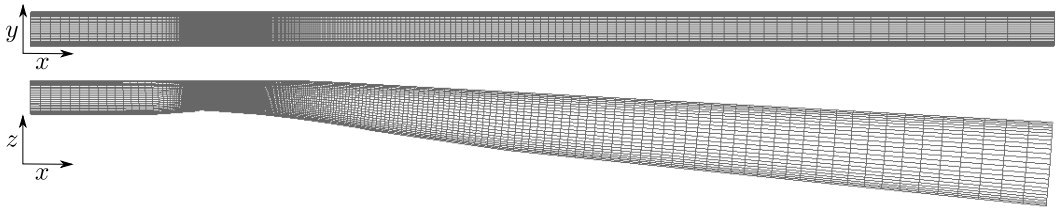

Figure 4.2: Mesh generation of the 3-D case represented with one visible mesh point out of three in the y and z directions.

4.1.1 Case set up

L_x	h_{in}	h_{throat}	L_y
1.512 m	0.05 m	0.0437 m	0.044 m

Table 4.1: Geometric dimensions.

A 4° divergence angle Venturi configuration, as the one used in the experiment of Barre *et al.* (2009), is selected for the study. Figure 4.1 illustrates the Venturi geometry, and Tab. 4.1 indicates flow and sections parameters used in the current case. Probes positioning is calibrated to capture data adjacent to the cavitation pocket at four stations (S1 to S4 in Fig.4.1) located at 20.9 mm, 38.4 mm, 55.8 mm and 73.9 mm from the Venturi throat. The inflow parameters are set as followed: the streamwise velocity $u_{in} = 10.8 m.s^{-1}$, the temperature $T_{in} = 293\ K$, the void ratio $\alpha_{in} = 10^{-10}$, the density $\rho_{in} = 1000.831\ kg.m^{-3}$ and the vaporisation pressure $P_{vap} = 2339\ Pa$. The inflow cavitation number σ_{in} is 0.55 and the inflow Reynolds number is $Re_{in} = \rho_{in} u_{in} h_{in} / \mu_{in} = 5.4 \times 10^5$. The outflow pressure is calibrated to correspond with this cavitation number. The study is focused on one operating point corresponding to the selected experiment set up.

Calculations over the 4° divergent angle Venturi apply 2-D and 3-D computational domains with

340×72 and $340 \times 72 \times 72$ mesh cells represented in Fig.4.2, respectively. The grids are designed in a structured fashion concerning maximum normal distance to the walls of wall-bounded cells, z^+ according to Fig. 4.1 coordinates, between 10 and 15 in the area of interest. The n parameter of the Reboud limiter, from Eq. 2.18, is set to 10 in the 2-D calculation (Goncalvès & Decaix, 2012) and 19 in the 3-D calculation. As observed in other works (Zhou & Wang, 2008; Ducoin *et al.*, 2012; Ji *et al.*, 2014), the choice of n in the 3-D configuration is motivated by an under-prediction of the re-entrant jet development for the k-l model using $n = 10$. For that reason, the n parameter is calibrated to correctly capture the re-entrant jet by comparing with experimental data. The dissipative terms parameters of the extended Jameson-Schmidt-Turkel scheme k_2, k_2^I and k_4 are respectively set to 1.0, 1.5 and 0.045. Furthermore, the time step is fixed to 4.58×10^{-6} s and 2.29×10^{-7} s for the 2-D and 3-D simulations, respectively, and a total of 2.06 s physical time is run for the two numerical studies. Table 4.2 presents the required parameters for the computation of the cavitation model for both phases. Another 3-D computation is carried out on the same geometry with the same parameters except for a twice larger width and periodic side boundary conditions.

	ρ^{sat} (kg/m^3)	γ	p_∞ (Pa)	q (J/kg)	Cp $(J/K\ kg)$
liquid	998.16	1.01	1.211×10^7	-1.142×10^6	4183
vapour	0.0173	1.32	0	1.985×10^6	1883

Table 4.2: Parameters of the cavitation model.

4.1.2 Comparison with experimental data

The numerical results of the in-flow simulation are then compared to the experimental data from Barre *et al.* (2009). This experiment provides measures of time-averaged velocity, void ratio, and wall pressure profiles at stations located in the midspan of the Venturi.

4.1.2.1 Velocity and void ratio profiles

Profiles of time-averaged velocity and time-averaged void ratio from 2-D and both 3-D simulation results are compared with experimental data at different positions in Figs. 4.3 and 4.4. Numerical results have similar behaviour for the first station $S1$. The capture of the re-entrant jet is in a good match with the experiment for the numerical results, apart from the 3-D periodic case at $S2$, since the negative values of the velocity are correctly determined, as observed in the velocity profiles at

the three other stations ($S2$, $S3$ and $S4$). The void ratio profiles are in good accordance for all computations but are in better agreement for the 3-D case with sidewalls, whose results indicate a better representation of the pocket size and shape when compared to the 2-D and 3-D periodic calculations. The 3-D computation with sidewalls correctly captures the physical behaviour of the cavitating flow. Moreover, the time-averaged results of this case are sensibly conformed with the experimental results. Differences between 3-D computations with sidewalls and periodic boundary conditions are discussed later.

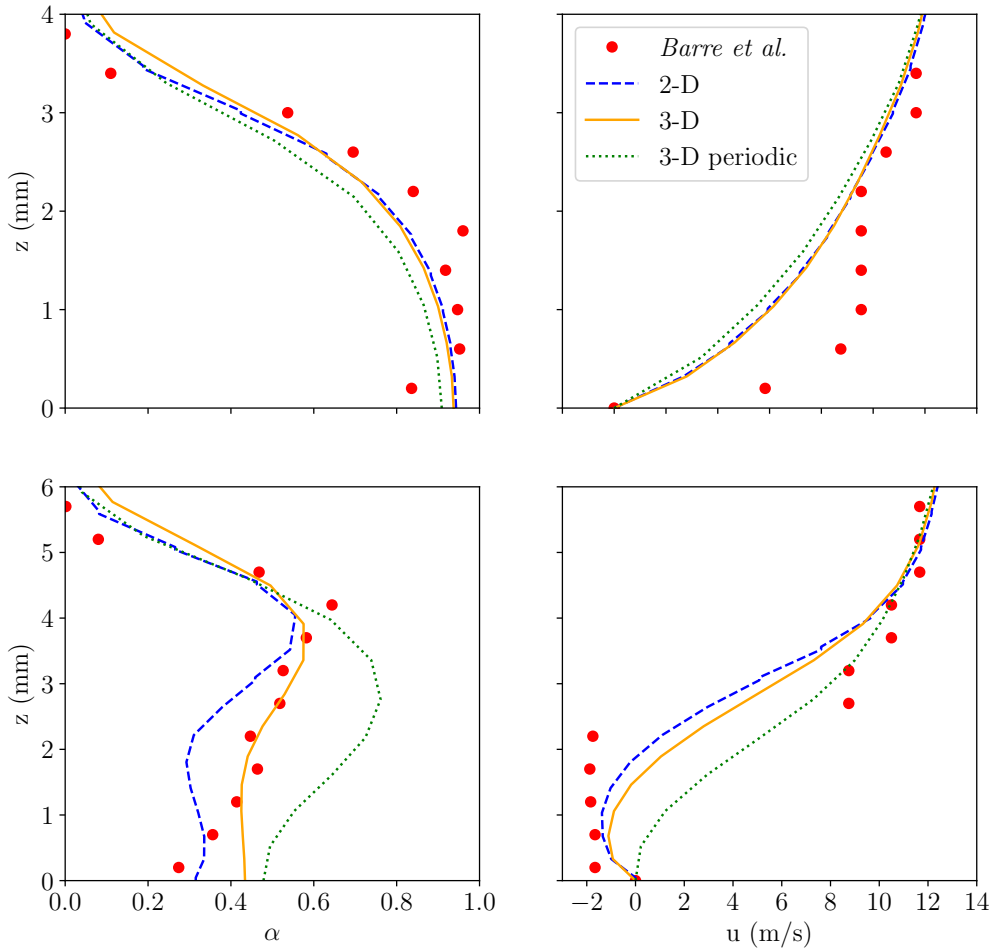

Figure 4.3: Time-averaged comparison at midspan between experiment, 2-D, 3-D and 3-D periodic for void ratio (left) and velocity (right) at stations S1 (top) and S2 (bottom).

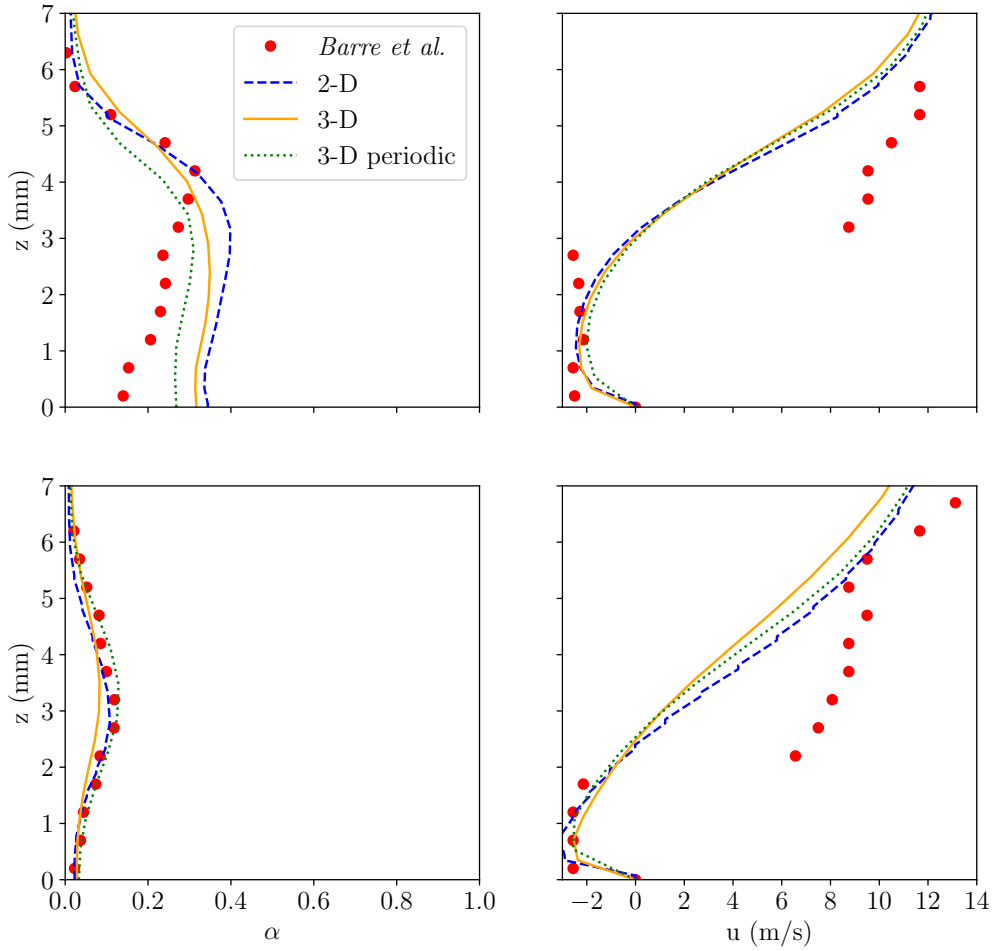

Figure 4.4: Time-averaged comparison at midspan between experiment, 2-D, 3-D and 3-D periodic for void ratio (left) and velocity (right) at stations S3 (top) and S4 (bottom).

4.1.2.2 Wall pressure profiles

The mean wall pressure and pressure fluctuations profiles are extracted from computations and are presented in Fig. 4.5 in comparison with experimental data. The wall pressure profile from the 2-D and 3-D calculations are in good agreement with experimental data along the cavity and reasonably fits the experimental data downstream the cavity. Nevertheless, the root mean square (RMS) fluctuations are slightly underestimated for all cases. Moreover, oscillations detected in the 2-D computation are not observed in 3-D computations.

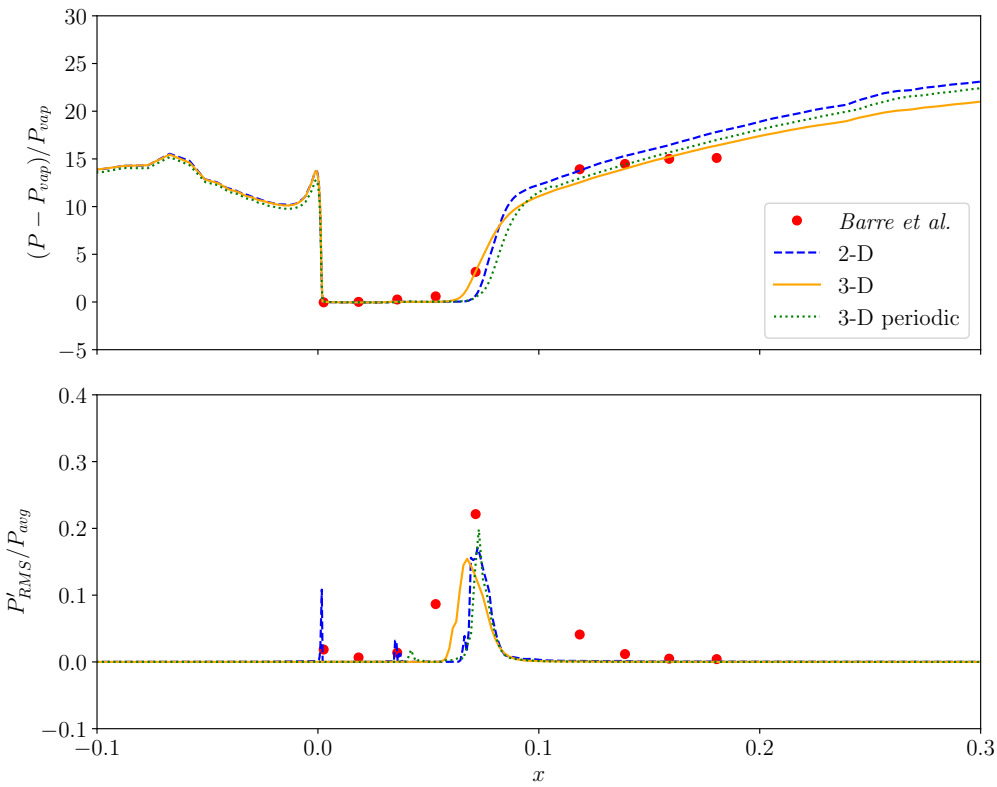

Figure 4.5: Time-averaged comparison between experiment, 2-D, 3-D and 3-D periodic for wall pressure and wall pressure RMS over wall pressure.

4.2 Global behaviour

The current section is dedicated to the first interpretation of numerical results from computations over 3-D configurations with and without sidewalls. A statistical analysis of the calculation data is performed to investigate the time-averaged and dynamical global behaviour of such flow configuration. Data are extracted at a 2.3×10^{-3} s timestep.

4.2.1 Time-averaged data analysis

According to experimental observations of the Venturi (Barre *et al.*, 2009), a weakly fluctuating cavity emerges without any large vapour shedding process. A time-averaged cavity length L_c between 70 and 85 mm, estimated with an α contour of 0.05, is observed in the experiment. Numerical results for the case with sidewalls present a pocket length of $L_c = 78.8$ mm, which is consistent with the experiment. This length is selected to be the characteristic length for the current study. The

maximum value of the time-averaged re-entrant jet velocity is also used as the characteristic velocity, $u_{max}^{jet} = 2.38\ m.s^{-1}$. The selection of these two characteristic variables is motivated by the observation of the cavitating flow behaviour and the identification of the leading mechanism. Moreover, the study of Dular & Bachert (2009) defines the re-entrant jet velocity at the cavity closure and the length of the attached vapour pocket as the most correct values to investigate the cavitating flow over a hydrofoil. The maximum reverse flow is also considered as the characteristic velocity in non-cavitating flows with separation bubble, Hammond & Redekopp (1998) or Rist & Maucher (2002) show the important role of the reverse flow in the triggering of instabilities. The Strouhal number is then defined as :

$$St = \frac{L_c f}{u_{max}^{jet}}. \tag{4.1}$$

In the literature, for sheet to cloud cavitation cases, the Strouhal number is mostly defined with inlet velocity (Gnanaskandan & Mahesh, 2016*b*; Ganesh *et al.*, 2016; Budich *et al.*, 2018). The choice of the characteristic velocity will be justified later by investigating the resulting Strouhal number. Variables with a superscript * in this chapter are dimensionless and are calculated using the characteristic length L_c and characteristic velocity u_{max}^{jet}.

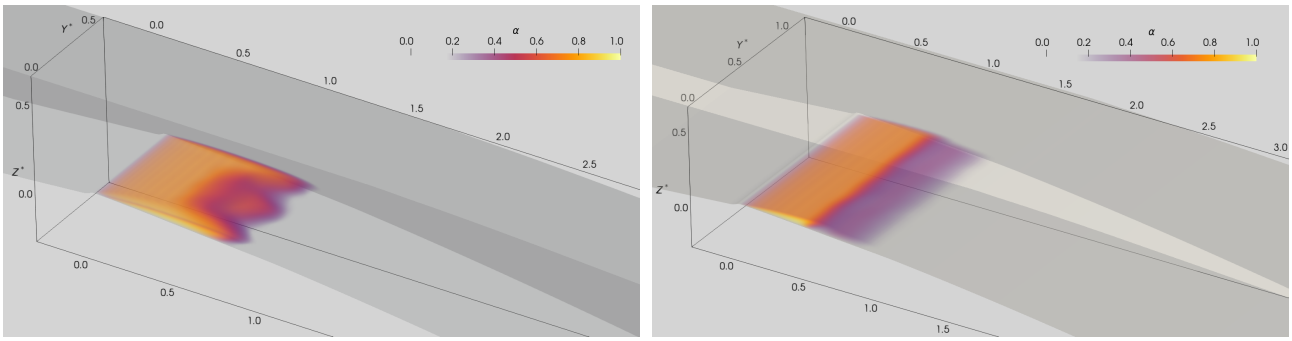

(a) (b)

Figure 4.6: Volume rendering of the time-averaged void ratio: (a) for the Venturi with sidewalls; (b) for the Venturi with side periodic boundary conditions

A symmetrical attached cavity is detected in Fig. 4.6a with a longer cavitation pocket length near sidewalls than near of the midplane of the Venturi. The U-shape of the cavitation pocket is detected as described in many references (Kubota *et al.*, 1989; Peng *et al.*, 2016). The lower amount of void ratio suggests vapour release and/or pocket oscillations around the mid-width. Figure 4.6b presents the cavitation pocket shape for the periodic case. Unlike the case with sidewalls, the cavity length is

constant in all the Venturi width. Then, the observation of the flow direction velocity in Fig. 4.7a and 4.7b underlines the presence of the re-entrant jet along the wall. The jet geometry is symmetric and is not present close to sidewalls whereas it is localised in all the Venturi width for the periodic case. Moreover, for the Venturi with sidewalls, the vertical velocity is also symmetric, while the spanwise velocity is anti-symmetric.

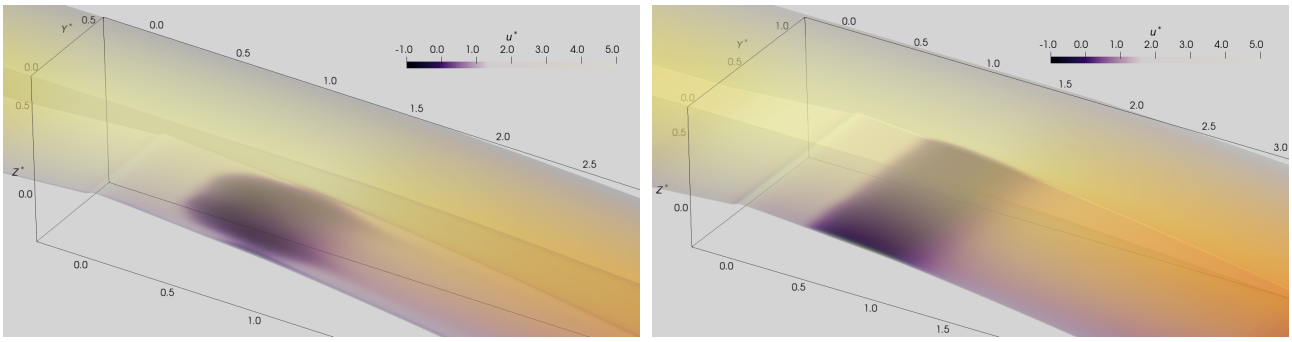

(a) (b)

Figure 4.7: Volume rendering of the time-averaged streamwise velocity : (a) for the Venturi with sidewalls; (b) for the Venturi with side periodic boundary conditions

4.2.2 Dynamic analysis

A study of the flow dynamics is carried out to statistically interpret the behaviour of the cavitation pocket and velocity components over time for configurations with sidewalls and with side periodic boundaries. First, the analysis is focused on the case with sidewalls. Figure 4.8 shows the void ratio α into the flow at six different times. It is worth to notice that the pocket shape is not symmetric and evolves with time. A small high-frequency vapour shedding appears around the cavity closure while the pocket seems to oscillate in the spanwise direction. A statistical analysis is carried out to check any data fluctuations within the Venturi flow. The RMS results over the spanwise velocity v are presented in Fig. 4.10. The highest values of fluctuation are located at the pocket closure, mostly around the mid-width. Therefore, it corroborates the occurrence of a spanwise oscillation of the flow nearby this area.

The Q criterion is then calculated, from the vorticity tensor $\mathbf{\Omega}$ and the strain rate tensor $\mathbf{S}$, using the formula 4.2 to investigate the capture of any vortexes.

$$Q = \frac{1}{2}(|\mathbf{\Omega}|^2 - |\mathbf{S}|^2) > 0, \tag{4.2}$$

with

$$\mathbf{\Omega} = \frac{1}{2}\left(\nabla\mathbf{w} - (\nabla\mathbf{w})^{\mathbf{T}}\right) \quad \text{and} \quad \mathbf{S} = \frac{1}{2}\left(\nabla\mathbf{w} + (\nabla\mathbf{w})^{\mathbf{T}}\right). \tag{4.3}$$

Figure 4.9 presents a non-dimensional Q^* criterion contour compared with the vapour pocket location. It is worth to notice that, besides the use of a URANS formulation, the computation seems to capture a vortex mechanism located right downstream the cavity closure. The structure of the vortex follows the spanwise vapour pocket shape. Hence, the presence of the cavity leads to vortex development.

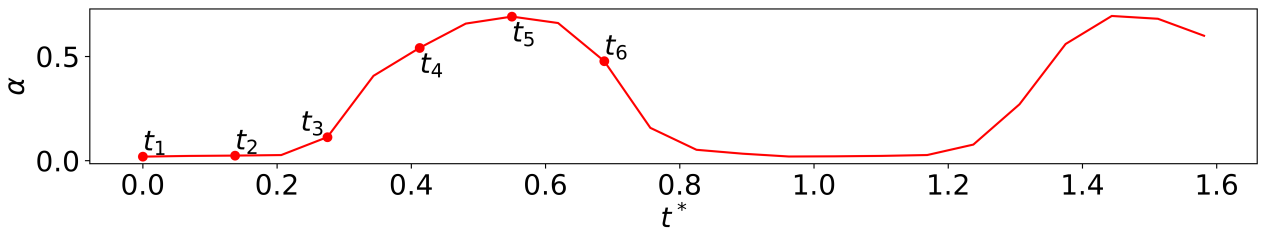

(a) Void ratio signal.

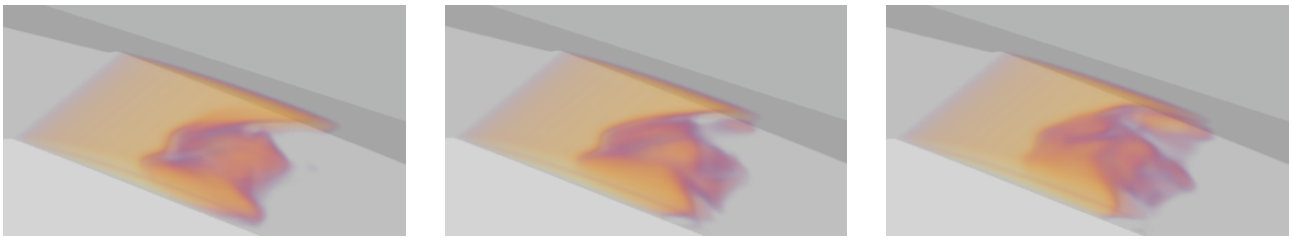

(b) t_1

(c) t_2

(d) t_3

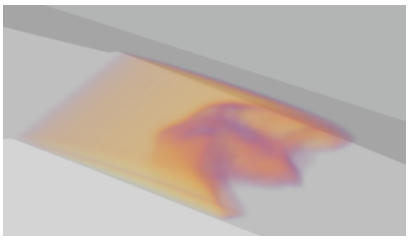

(e) t_4

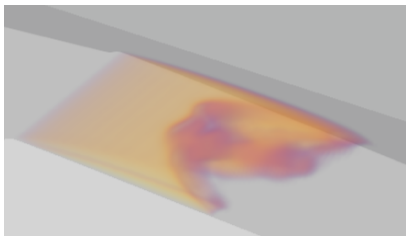

(f) t_5

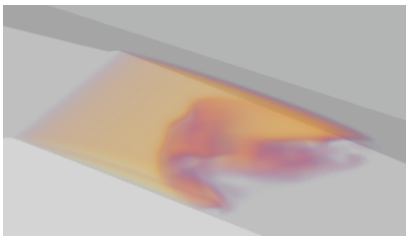

(g) t_6

Figure 4.8: Time evolution of the attached cavity with snapshots separated by $\Delta t = 4.58\ 10^{-3}\ s$ with a volume rendering; (b)-(g) Snapshots extracted at different time represented in the void ratio signal (a).

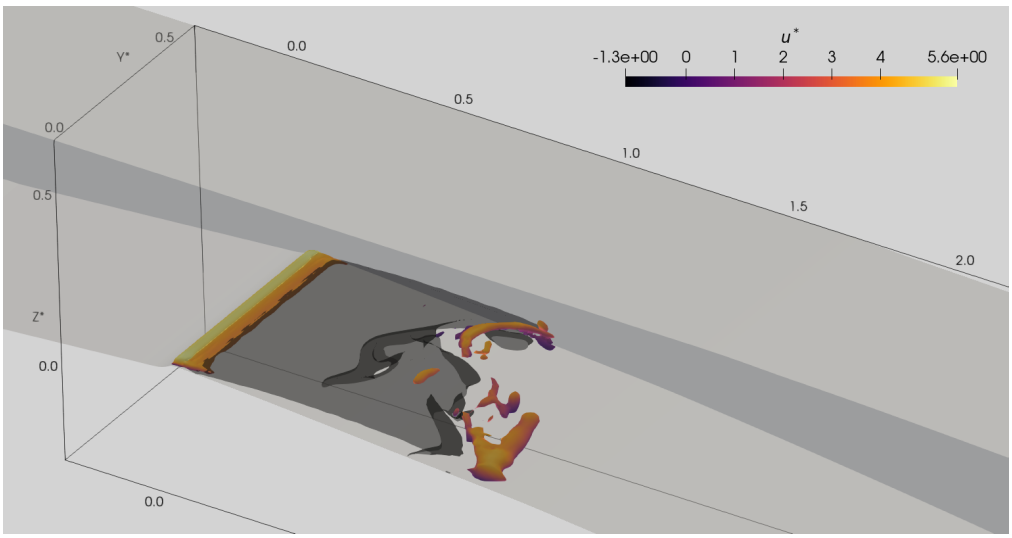

Figure 4.9: Snapshot of the Q^* criterion contour of 0.5 with flow direction velocity u^* display compared to the vapour pocket positioning suggested by the $\alpha = 0.5$ contour (dark).

Subsequently, the time evolution of flow variables is extracted for points in the flow direction and in the spanwise direction to perform Power Spectral Densities (PSD). The result is presented as a map of PSD along the longitudinal and spanwise axis. PSD maps provide information to identify any high energy frequencies and locate the associated phenomenon into the Venturi. Figure 4.11 presents the PSD map over the spanwise direction, respectively for the void ratio and the spanwise velocity, positioning at almost the two thirds of the mean cavity length. A sample of signal used for the PSD computations can be observed in Fig.4.14. It is worth to remark that no particular dynamics are detected inside the attached cavitation pocket. A dominant Strouhal number of 1.09 is highlighted around the cavity closure by detecting the highest PSD energy values. These are underlined in the mid-width of the Venturi for velocity and near sidewalls for the void ratio. Similar behaviour is observed for PSD maps downstream the cavity but with the appearance of a low frequency for the void ratio. Regarding previous remarks over snapshots of Fig. 4.8 and the RMS of the spanwise velocity, the Strouhal number $St_0 = 1.09$ seems to be linked to a spanwise oscillation of the cavitation pocket. Firsts harmonics of St_0 also emerge from the PSD map for the void ratio.

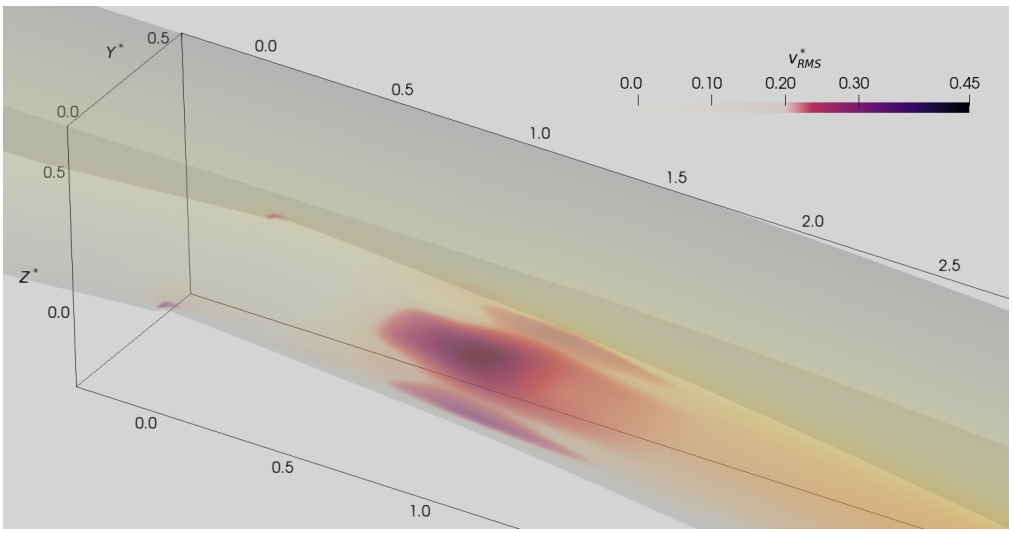

Figure 4.10: Volume rendering of the RMS fluctuation of the spanwise velocity v.

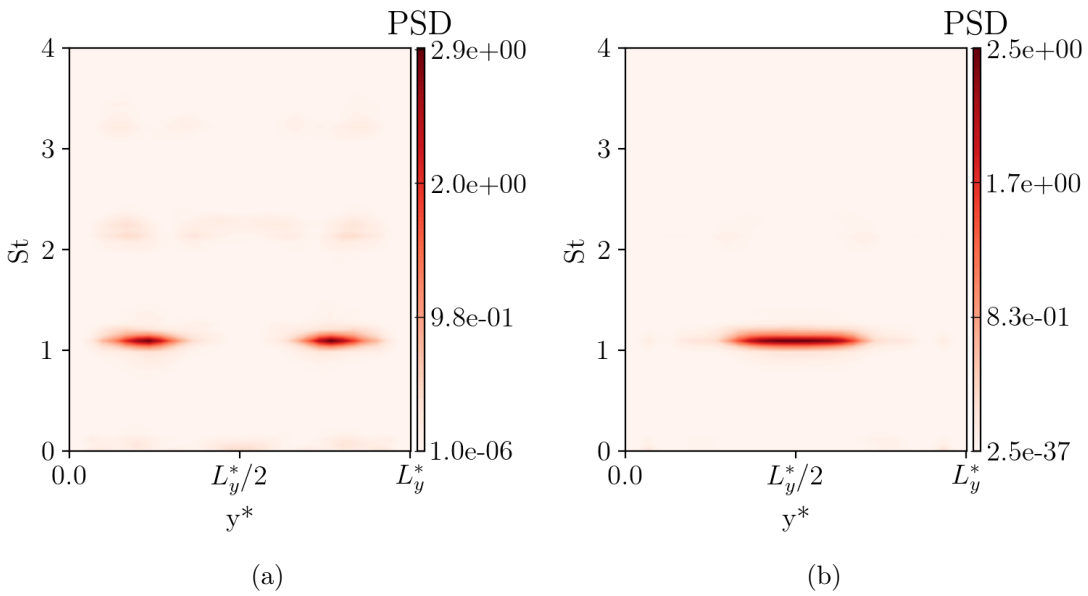

Figure 4.11: PSD maps along spanwise axis at $x^* = 0.64$ and at a vertical distance $z^*_p = 0.032$ from the bottom wall : (a) for the void ratio α; (b) for the spanwise velocity v.

Figure 4.12 shows the PSD map over the streamwise direction for the void ratio at the quarter width. As previously noticed, neither particular dynamic is detected in the mid-width for the void ratio. Nevertheless, at the quarter width, the highest values of the PSD are observed around the cavity closure at the same Strouhal number St_0.

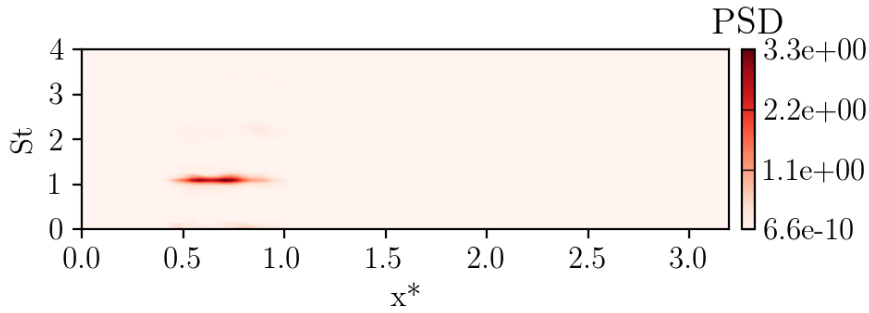

Figure 4.12: PSD map for α along longitudinal axis at $y^* = L_y^*/4$ and at a vertical distance $z_p^* = 0.032$ from the bottom wall.

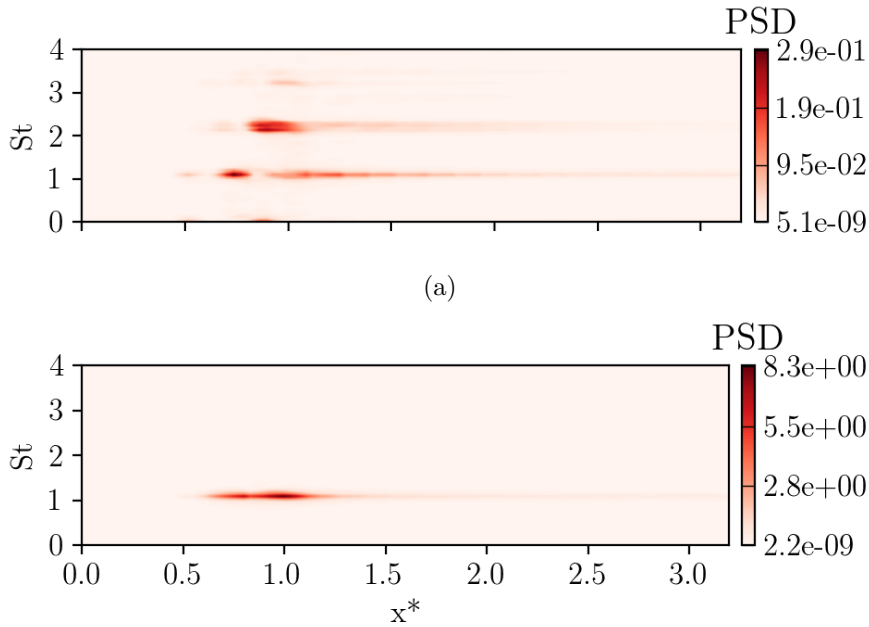

Figure 4.13: PSD maps for spanwise velocity v along longitudinal axis at a vertical distance $z_p^* = 0.032$ from the bottom wall : (a) at $y^* = L_y^*/8$; (b) at $y^* = L_y^*/2$.

Figure 4.13 presents the PSD map over the streamwise direction for the spanwise velocity, at two positions on the spanwise axis: one located in the mid-width ($y^* = L_y^*/2$) and another one in the eighth width ($y^* = L_y^*/8$). The same behaviour as for the void ratio is underlined at both positions but with also a propagation of the dynamics downstream. Furthermore, at the eighth width positioning, the two first harmonics are also detected around the cavity closure and downstream.

The PSD analysis identified a dominant dynamics at the Strouhal number St_0. This phenomenon appears nearby the cavity closure and is propagated downstream. Furthermore, a motion of the cavitation pocket has been highlighted close to sidewalls. A spanwise velocity variation also emerges at the mid-width of the Venturi. The dominant flow fluctuations and its location has been determined. However, a correlation study is carried out by extracting the flow variables over time close to both sidewalls to specify the cavity behaviour. One can remark that, in Fig. 4.14, data are in opposition of phase, which can lead to a conclusion that the cavitation pocket motion is assimilated to a periodic oscillation from one sidewall to another.

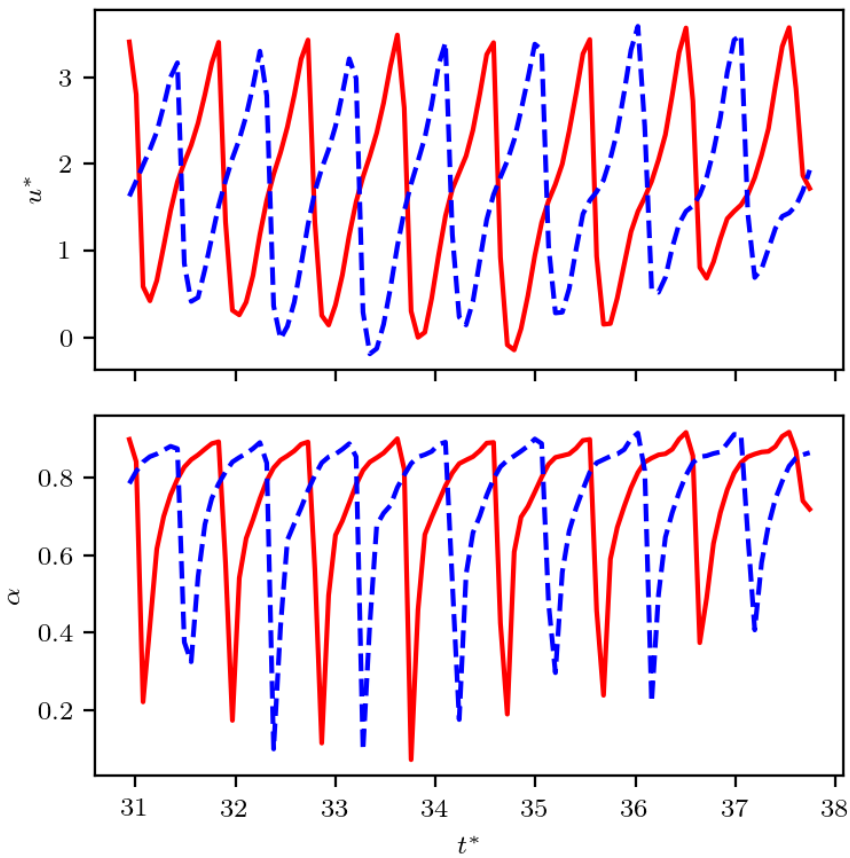

Figure 4.14: Temporal evolution of the flow direction velocity u and the void ratio α at $x^* = 0.64$ along both sidewalls (one in red, the other in blue) for the case with sidewalls.

Dynamics analysis of the case with periodic boundaries is then carried out to investigate the

sidewall effects. First observations of snapshots do not allow to identify any periodic oscillations of the cavitation pocket. However, a three-dimensional dynamic behaviour of the cavity is observed around the closure. Figure 4.15 shows PSD maps along the longitudinal axis for the void ratio and the spanwise velocity component. The same Strouhal number St_0 and its first harmonic are extracted around the cavity closure for both variables and propagated downstream for the spanwise velocity component. The same Strouhal number is obtained from PSD maps over the results of the periodic case and the case with sidewalls. Hence, it suggests that the cavitation pocket fluctuations are not dependant of the presence of sidewalls. A deepened analyse is performed in Sec. 4.4 to confirm this observation.

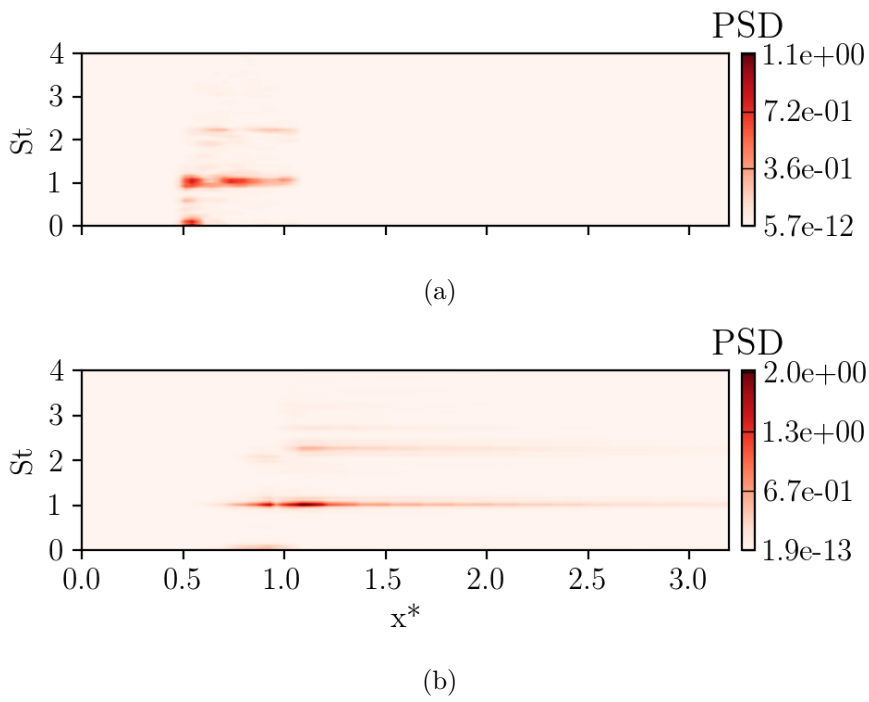

Figure 4.15: PSD maps of the periodic case along longitudinal axis at the mid-width and at a vertical distance $z_p^* = 0.032$ from the bottom wall : (a) for the void ratio α; (b) for the spanwise velocity v.

4.3 Re-entrant jet

In this section, the behaviour of the re-entrant jet is studied in regards to the cavitation pocket oscillation for the case with sidewalls. Figure 4.16 describes the re-entrant jet position in relation to the cavity position at different times over an oscillation period. As expected, the re-entrant jet

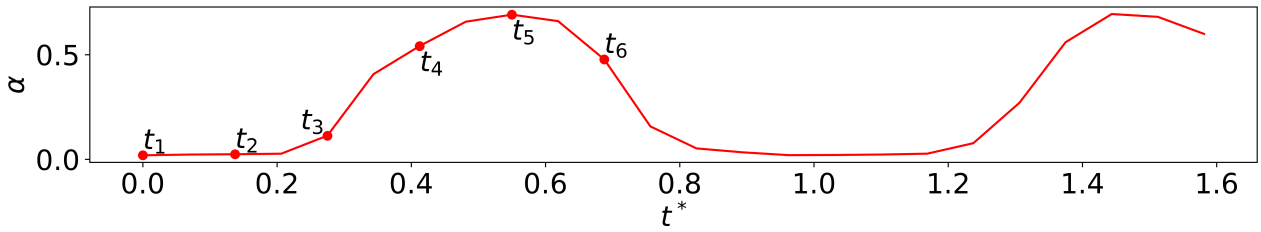

(a)

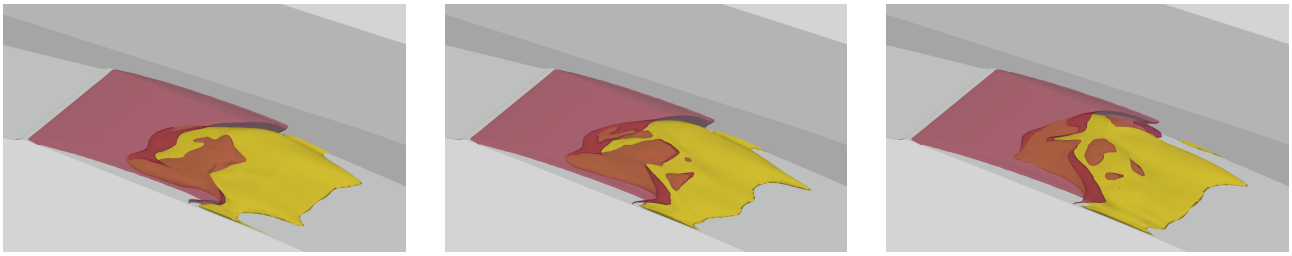

(b) t_1

(c) t_2

(d) t_3

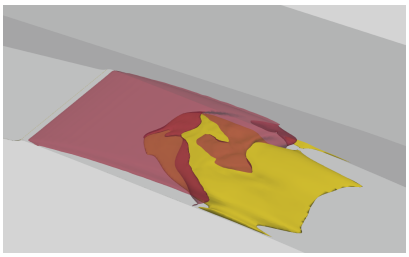

(e) t_4

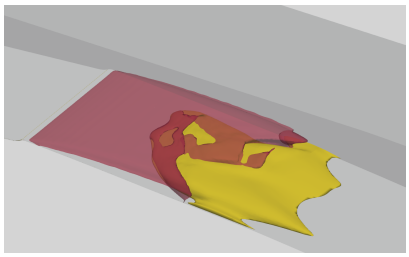

(f) t_5

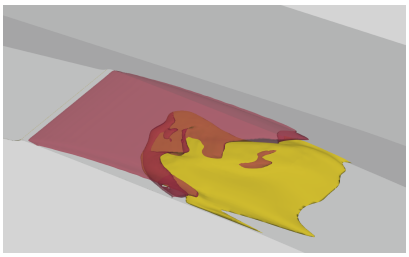

(g) t_6

Figure 4.16: Dynamics of the re-entrant jet regarding the vapour cavity : (a) void ratio over time at $x^* = 0.8$ and $y^* = 3L_y^*/4$ for the case with sidewalls; (a)-(f): Snapshots with timestep $\Delta t = 4.58\times10^{-3}s$ of $\alpha = 0.5$ (purple) and $u^* = -0.1\ m.s^{-1}$ (yellow) contours.

is located nearby the cavity closure and is time-dependent. Moreover, PSD maps of the streamwise velocity highlight a dynamics around the cavity closure based on the Strouhal number St_0. Thus, the re-entrant jet oscillates at the same frequency as the cavitation pocket from a spanwise wall to another. However, the position of the re-entrant jet compared to the cavity has to be determined. Figure 4.17 presents the time evolution of the void ratio α and the flow direction velocity u around the cavity closure at the quarter width. The negative values of the streamwise velocity component illustrate the re-entrant jet position and the highest value of the void ratio represents the cavity position. The time evolution of u and α indicates an opposition in both oscillations of the cavitation pocket and the re-entrant jet. When the pocket is asymmetric in the spanwise direction, the re-entrant jet presents

an opposite asymmetry. The cavity growth near side walls is smoother when compared to the cavity disappearance at the same position. For the re-entrant jet signal, it is the opposite behavior, high growth and a smoother decrease. Therefore, the maximum peaks of void ratio exactly correspond, in time, to the maximum ones of flow direction velocity, while both minimum ones are time-shifted. Hence, the spanwise movement is not uniform. When the cavity moves nearby sidewalls, it is pushed back with acceleration and, at the same time, the re-entrant jet motion changes its spanwise direction with an acceleration. Such behaviour indicates a possible causality effect between both phenomena.

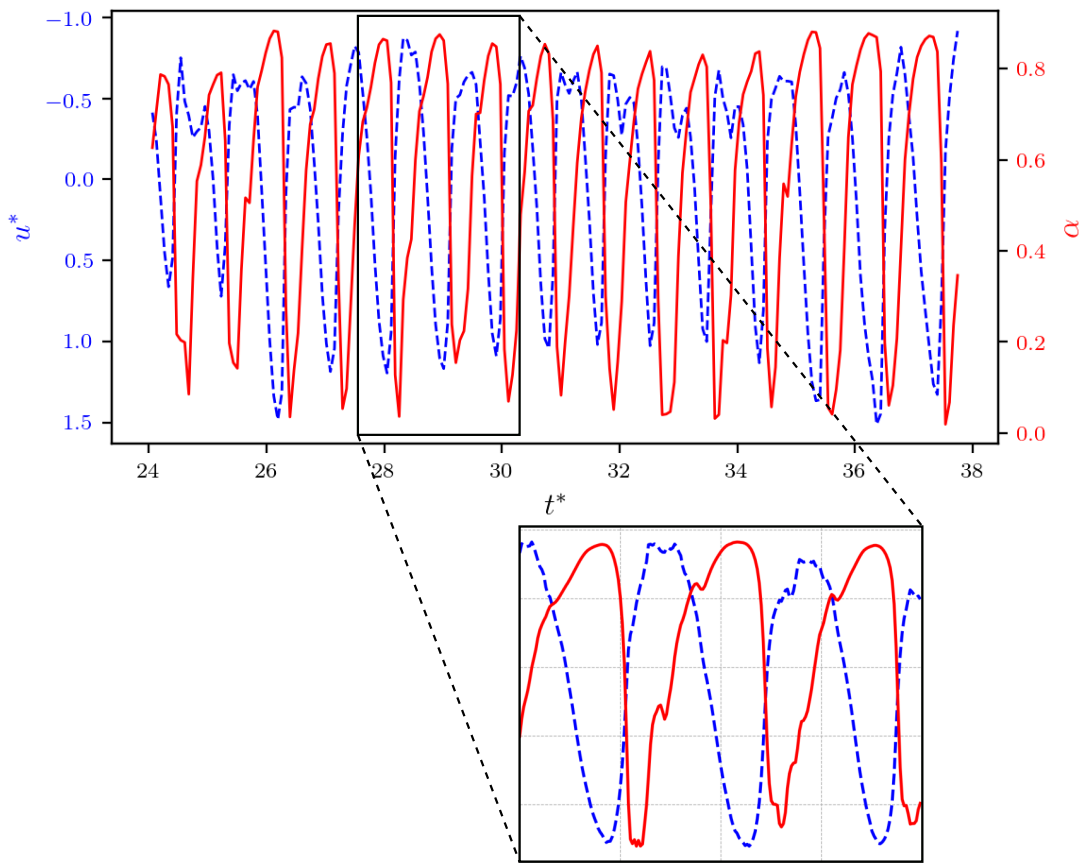

Figure 4.17: Time evolution of the flow direction velocity u and the void ratio α at $x^* = 0.64$ and $y^* = L_y/4$ for the case with sidewalls.

4.4 Modal decomposition analysis

Early results highlighted a dominant flow component at the Strouhal number St_0 probably linked to a cavitation pocket oscillation. Modal decomposition analysis are performed to corroborate pre-

vious observations. The Spectral Proper Orthogonal Decomposition (SPOD) is computed from the computational data to identify spatiotemporal mechanisms. The choice of the SPOD is motivated by the extraction of spatiotemporal modes which is the most coherent method to study unsteady flow as presented by Towne *et al.* (2018). The SPOD methodology employed, based on Schmidt & Colonius (2020) work, is described below.

Given a snapshot $\boldsymbol{q}_i' = \boldsymbol{q}_i - \bar{\boldsymbol{q}}$ which represents the fluctuation of the flow result for the density and the velocity components at a time t_i, the data matrix $\boldsymbol{Q}$ is defined as:

$$\boldsymbol{Q} = [\boldsymbol{q}_1' \ \boldsymbol{q}_2' \ \boldsymbol{q}_3' \ \dots \ \boldsymbol{q}_N'], \tag{4.4}$$

with $\bar{\boldsymbol{q}}$ the temporal mean. The cavitating flow is modelled using a compressible formulation, therefore, the instantaneous energy is defined based on the Chu norm (Chu, 1965) with the temperature fluctuation neglected. It is expressed with a spatial inner product:

$$\|\boldsymbol{q}_i'\|_E = \langle \boldsymbol{q}_i', \boldsymbol{q}_i' \rangle_E = \boldsymbol{q}_i'^T \boldsymbol{M} \boldsymbol{q}_i' = \boldsymbol{q}_i'^T \boldsymbol{R}^T \boldsymbol{R} \boldsymbol{q}_i' = \|\boldsymbol{R}\boldsymbol{q}_i'\|_2, \tag{4.5}$$

$$\boldsymbol{M} = \boldsymbol{R}^T \boldsymbol{R} = \begin{pmatrix} \frac{\bar{T}}{2\bar{\rho}\gamma M_\infty^2}\boldsymbol{A} & 0 & 0 & 0 \\ 0 & \frac{\bar{\rho}}{2}\boldsymbol{A} & 0 & 0 \\ 0 & 0 & \frac{\bar{\rho}}{2}\boldsymbol{A} & 0 \\ 0 & 0 & 0 & \frac{\bar{\rho}}{2}\boldsymbol{A} \end{pmatrix}.$$

Where $\boldsymbol{A}$ stands for the diagonal cell volume matrix, $\bar{T}$ the temporal mean temperature, $\bar{\rho}$ the temporal mean density and M_∞ the far-field Mach number. The first step of the SPOD decomposition is to apply Welch's method to the data matrix. It consists of separating the data in N_{blk} overlapping blocks of snapshots and then performed the discrete Fourier transform on each block. Thus, N_{blk} matrix of N_{freq} discrete frequency realisations are obtained. Then, the Fourier realisations of all blocks are grouped by frequency to obtain N_{freq} matrix $\hat{\boldsymbol{Q}}_{fr}$:

$$\hat{\boldsymbol{Q}}_{fr} = [\hat{\boldsymbol{q}}_{fr}^1 \ \hat{\boldsymbol{q}}_{fr}^2 \ \hat{\boldsymbol{q}}_{fr}^3 \ \dots \ \hat{\boldsymbol{q}}_{fr}^{N_{blk}}], \tag{4.6}$$

where $\hat{\boldsymbol{q}}_{fr}^i$ denotes the Fourier realisation of the ith block at the frequency fr. The second part of the SPOD decomposition is to compute the cross-spectral density matrix at each frequency:

$$\boldsymbol{S}_{fr} = \hat{\boldsymbol{Q}}_{fr} \hat{\boldsymbol{Q}}_{fr}^*, \tag{4.7}$$

$(.)^*$ denotes the complex conjugate. Thus, the SPOD modes $\boldsymbol{\Psi}_{fr}$ are generated by the eigenvalue decomposition of the cross-spectral density matrix:

$$\boldsymbol{S}_{fr}\boldsymbol{M}\boldsymbol{\Psi}_{fr}^{*} = \boldsymbol{\Psi}_{fr}\boldsymbol{\Lambda}_{fr}, \tag{4.8}$$

with $\boldsymbol{\Lambda}_{fr}$ the diagonal matrix of eigenvalues representing the mode energy from the most energetic, corresponding to the leading SPOD mode, to the less one.

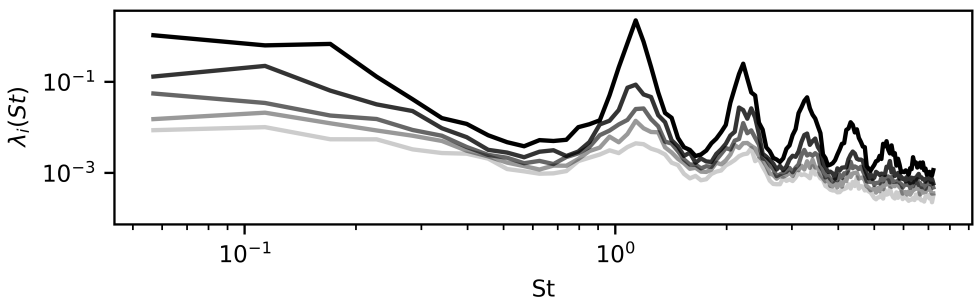

(a)

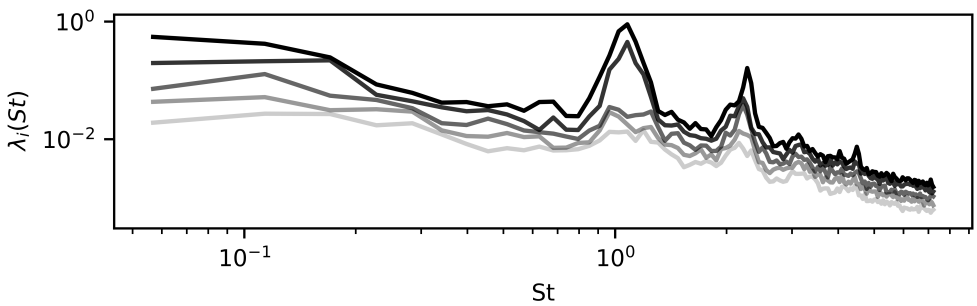

(b)

Figure 4.18: SPOD spectrums representing energy gain over Strouhal number : (a) for the sidewalls case; (b) for the periodic case. The black to grey scale represents the most energetic mode to the less energetic one for each Strouhal number.

Figure 4.18 presents the SPOD spectrum for both studied cases. The Strouhal number $St_0 = 1.09$ and its harmonics emerge from the spectrum for the simulation with sidewalls. Similarly, for the periodic sides simulation, the Strouhal number St_0 is extracted from the spectrum but with only the first harmonic. Hence, the dominant flow mechanism seems to be characterised by the Strouhal number St_0. Moreover, for the sidewalls case, the observation of the energy gain gap between the first and the second SPOD mode at the corresponding frequency proves that the associated mechanism is mostly

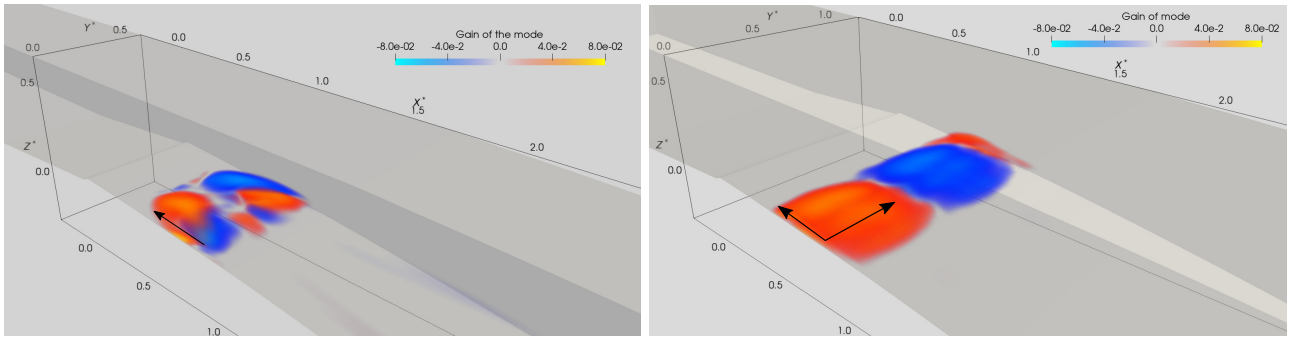

(a) (b)

Figure 4.19: Volume rendering of the dominant mode of the SPOD for ρ at $St = 1.09$; $\rightarrow$: Time evolution behavior; (a) for the case with sidewalls; (b) for the case with periodic side boundaries.

led by the first mode. Nevertheless, for the periodic sides case, the energy gap is located between the second and the third mode. The associated mechanism is then mostly driven by the two first modes.

Figures 4.19 to 4.22 show the real part of the dominant mode for density and velocity components for both cases. Arrows underline the time evolution of the mode. For the density in the simulation with sidewalls in Fig.4.19a, the mode is antisymmetric and corresponds to a spanwise oscillation coupled with a non-uniform upstream flow. It is noticed that the mid-width plane is not affected by the fluctuations. Similarly, the spanwise oscillations are observed by the antisymmetric mode for the streamwise velocity in Fig.4.20a and the vertical velocity in Fig.4.22a with the upstream behavior. Conversely, the mode of the spanwise velocity in Fig.4.21a is symmetric but also corresponds to the spanwise oscillation between sidewalls. However, in contrast with the density oscillation, the dominant mode for velocity components is also propagated downstream by the flow with a higher speed. These results substantiate the previous ones observed in the PSD analysis. By examining the harmonic modes, it is determined that, contrary to the dominant one, the first presents a symmetric behaviour for density, longitudinal velocity and vertical velocity while it illustrates an antisymmetric behaviour for the spanwise velocity. Nevertheless, the second harmonic mode shows the same symmetrical and antisymmetrical characteristics as the dominant mode. Hence, an alternation of symmetry and antisymmetry is observed in harmonic modes. The dominant SPOD mode for the case with periodic sides mainly differs from the sidewalls case for the density and the spanwise velocity component. In the first one, as observed in Fig.4.19b, a spanwise alternation of the cavitation pocket and an upstream

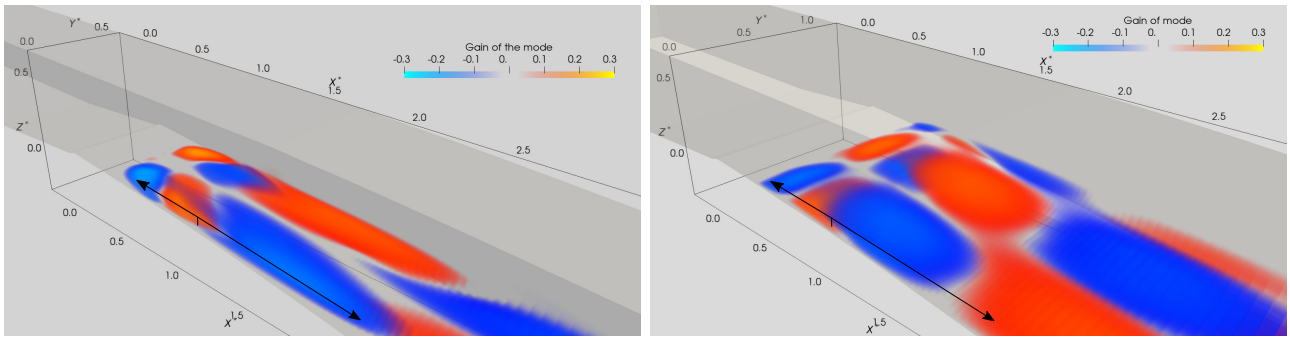

(a) (b)

Figure 4.20: Volume rendering of the dominant mode of the SPOD for u at $St = 1.09$; $\rightarrow$: Time evolution behaviour; (a) for the case with sidewalls; (b) for the case with periodic side boundaries.

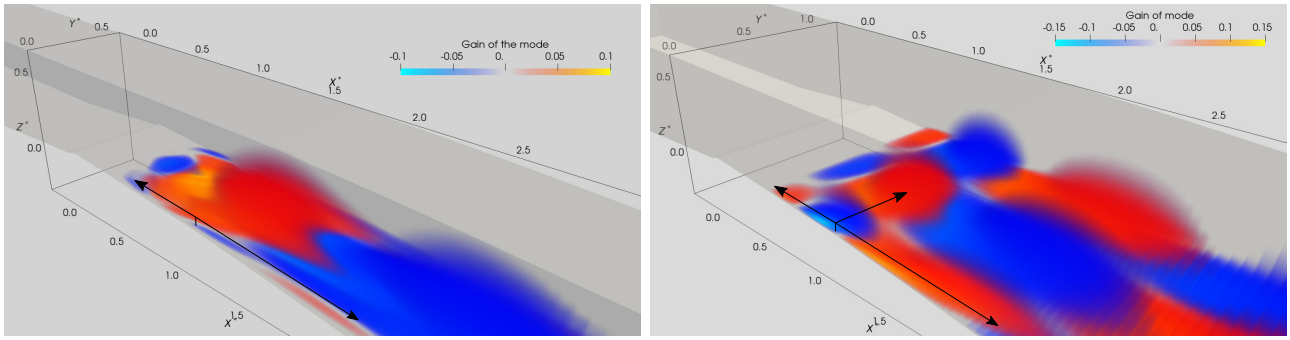

(a) (b)

Figure 4.21: Volume rendering of the dominant mode of the SPOD for v at $St = 1.09$; $\rightarrow$: Time evolution behaviour; (a) for the case with sidewalls; (b) for the case with periodic side boundaries.

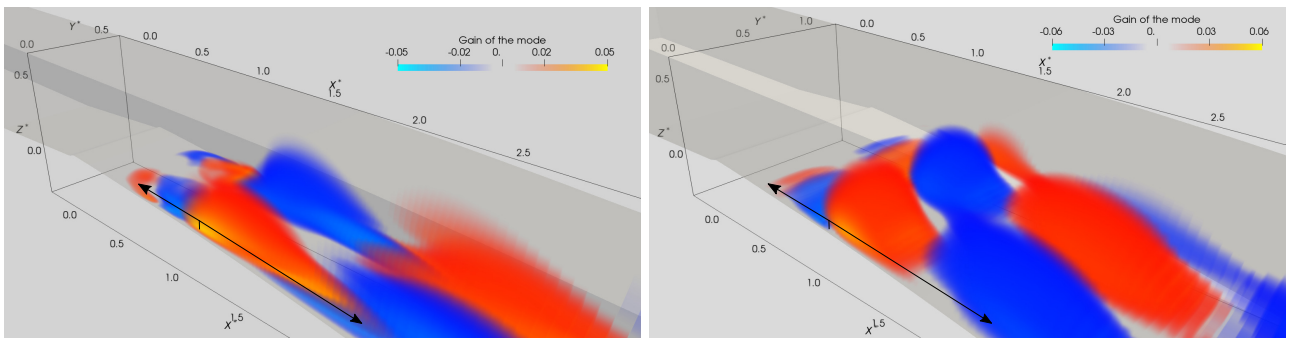

(a) (b)

Figure 4.22: Volume rendering of the dominant mode of the SPOD for w at $St = 1.09$; $\rightarrow$: Time evolution behaviour; (a) for the case with sidewalls; (b) for the case with periodic side boundaries.

flow are depicted. Then, a non-homogeneous spanwise motion is also captured around the cavity closure. It has to be noticed that the second SPOD mode, at the Strouhal number St_0, presents a similar behaviour with an opposite direction for the spanwise motion. The first two modes are theoretically equiprobable. In the dominant mode for the spanwise velocity component, Fig.4.21b, both upstream and downstream motions are detected but with also a non-homogeneous spanwise movement at the cavity closure. Unlike the case with sidewalls, this mode is not symmetric and it highlights an alternation of the spanwise velocity component along the spanwise axis. Furthermore, the second mode has an opposite movement along the spanwise axis. The SPOD mode behaviour, for the streamwise and the vertical velocity components, is similar to the ones for the case with sidewalls.

4.5 Discussion

A dominant dynamics has been highlighted by diverse analysis of the cavitating flow. It has to be noticed that a similar behaviour has been detected in computations with the turbulence model of Spalart-Allmaras. The current section offers the authors interpretation of the phenomenon.

Oblique-shape behaviours of the cavitation pocket have already been observed in two different sheet cavitation experiments. The first one is a Venturi flow experiment with 8° divergent angle carried out by Dular *et al.* (2012). In this case, vapour release into the flow appears under certain conditions and, for one of the studied geometry, the cavity presents a non-symmetrical shape. The authors suggest that it is caused by the re-entrant jet, which, besides going upstream, turns to the side. Nevertheless, due to the higher divergent angle, the pocket is cut by the re-entrant jet and leads to a vapour release. The second experiment is a flow around a guide vane profile carried out by Timoshevskiy *et al.* (2016). Under the vapour release regime, non-symmetrical cavitation pocket behaviour appears, as for the previous experiment. However, this regime is defined as non-persistent by the authors. Both experiments present a vapour release regime which could explain that the re-entrant jet bifurcation and the cavity shape do not lead to an identical spanwise oscillation. Nonetheless, it is suggested that the leading mechanism of those phenomena could be the same. The behaviour of the re-entrant jet against the cavitation pocket in both experiments and the current work is identical: when the cavity is expanded on one side, the re-entrant jet is more developed on the other side.

The SPOD analysis validates the presence of a dominant dynamics of the flow at a Strouhal number of 1.09. First, for the case with sidewalls, such a phenomenon is associated to the spanwise oscillation of the flow. The re-entrant jet is then captured as observed in the mode dynamics for density and velocity components. For this reason, it presents a significant role in the spanwise oscillation. The present study does not give enough information to ensure that the re-entrant jet is the mechanism which leads to the oscillation. Nevertheless, experiments describing the vapour release regime considered that the shedding is triggered by the re-entrant jet which "cuts" the cavity by going upward. Therefore, given the promiscuity of the physical phenomenon, it can be presumed that the re-entrant jet is the leading mechanism of the oscillation for the present case.

The spanwise oscillation is easily observed through the dominant mode dynamics for the spanwise velocity which highlights an alternation of positive and negative velocity around the cavity closure. By analysing the predominant mode dynamics for the velocity components, it is noticed that the oscillation pattern is simultaneously propagated upstream, by the re-entrant jet, and downstream by the main flow. The downstream flow is thus highly influenced by the pocket and the re-entrant jet dynamics while the oscillation seems to be self-sustained by the upstream flow suggesting the possible existence of a global mode driving this dynamic.

Fluctuations observed just downstream the cavitation pocket are interpreted as an oscillation of magnitude for the vertical and the streamwise velocity components. When the pocket is expanded near a sidewall, the magnitude of these two components is increased on the same side and decreased on the other. This information involves that the longer the cavity is, the more accelerated the downward and the downstream speeds are. When the pocket moves to the other side, the velocity effects are reversed. Hence, the cavitation pocket interferes with the flow can be seen as a dynamic fluidic obstacle.

The results of the simulation with periodic sides boundaries give relevant information about the sidewalls impact on the flow. For this case, the cavity and the re-entrant jet shapes are unchanged along the spanwise axis. Therefore, the U-shape of the cavitation pocket and the re-entrant jet shape are linked to the presence of sidewalls. However, the extraction of a dominant mode at the same Strouhal number suggests that the sidewalls do not trigger the spanwise oscillation but only amplify a phenomenon. The dominant dynamics is then led by a mechanism specific to the cavitating flow. The Strouhal number of 1.09 linked to the dominant mode is obtained by using two characteristic quan-

tities: the length of the cavitation pocket $L_c = 0.0788\ m$ and the maximum time-averaged velocity of the re-entrant jet at the midspan $u_{jet}^{max} = 2.38\ m.s^{-1}$. Hence, the mechanism highlighted by the current study seems to be inherent to the pocket development.

For the periodic case, the associated energy of the two first SPOD modes extracted at the Strouhal number St_0 are close. The impact of these modes on the flow is then almost identical. Furthermore, both present an opposite spanwise movement of the fluctuations for the density and the spanwise velocity component. The two modes could be described as a bifurcation of the flow with an equal probability of appearance. This hypothesis could be investigated by simulating the case on a much longer time.

4.6 Conclusion

The 3-D effects of cavitating flow, with a partial cavity, are studied in the case of a 4° divergent angle Venturi. Two configurations, with sidewalls and with periodic side boundaries, are computed for an identical physical time. Time-averaged data and dynamic analysis highlight flow structure differences, in particular in the cavitation pocket and re-entrant-jet shapes. Nonetheless, an identical Strouhal number of 1.09 linked to flow fluctuations is extracted in both cases. The SPOD analysis provides details about this phenomenon. A dominant mode at this Strouhal number is captured for both cases. For the simulation with sidewalls, it represents a spanwise oscillation of the flow observed through the cavitation pocket and re-entrant jet oscillation. It is noticed that the cavity and the re-entrant jet oscillations are in opposition of phase. Moreover, the flow bypassing the cavitation pocket accelerates and follows the pocket oscillation. Thus, the cavitation pocket acts as a dynamic obstacle. For the case with periodic spanwise boundaries, the dominant SPOD mode is energetically close to the second one at the same Strouhal number. Both show similar dynamics but with an opposite spanwise motion. These two modes could represent a flow bifurcation concerning spanwise fluctuations and are ideally equiprobable. Finally, the analysis of both cases involves that 3-D effects, non-related to the presence of sidewalls, appears in this cavitating flow configuration. The results also suggest that the phenomenon is linked to two characteristic variables of the flow: the cavity length and the maximum time-averaged re-entrant jet velocity at midspan. The link between the extracted Strouhal number and the two characteristic variables could be investigated. Other flow configurations presenting dis-

tinct cavity lengths could be used to attest the robustness of this conclusion. Furthermore, the use of higher resolution methods would give more information on the flow and could be useful to carry out further dynamics analyses. Hybrid RANS/LES methods could be selected as a continuation of the current work.

Chapter 5

Hybrid RANS/LES for sheet cavitation simulations

Contents

5.1 Hybrid RANS/LES method selection with NASA hump 114

5.1.1 Forcing hybrid formulation 114

5.1.2 DDES 115

5.1.3 DES $k - \ell$ 117

5.1.4 ZDES type III 118

5.1.5 Summary 120

5.2 Hybrid RANS/LES method for sheet cavitation flow within the venturi configuration 121

5.2.1 Detached Eddy Simulation with $k - \ell$ 122

5.2.2 Delayed Detached-Eddy Simulation (DDES) 123

5.2.3 Zonal Detached-Eddy Simulation (ZDES) Type III 125

5.2.4 Summary 126

Hybrid RANS/LES methods are selected to increase the flow simulation resolution while keeping an affordable computational cost. Models are generally defined with RANS formulation close to walls which is shifted to LES formulation farther. The transition is controlled by a switch depending on a turbulent length and the mesh resolution. A panel of existing or new models is investigated in the current chapter to simulate quasi-stable sheet cavitation. Particular attention is drawn to the switch zone, given that the vapour cavity is located around the same area.

5.1 Hybrid RANS/LES method selection with NASA hump

The NASA hump case is selected to investigate three hybrid RANS/LES methods and validate the use of these methods on a detached flow simulation. This study is a preamble to select appropriate hybrid methods for the computation of sheet cavitation flow. The same flow configuration as introduced in Sec. 3.3 is used in the present section. Nonetheless, meshes adapted to hybrid simulations are generated with refined area in the hump surroundings from $x^* = -1.0$ to $x = 1.5$ in the streamwise direction, uniformly in the spanwise direction and mostly close to the wall in the wall-normal direction. A first mesh is created to use the wall model with a first cell corresponding to $y^+ = 15$ on average and the next ones finer than the first one. Then, a second mesh is generated with $y^+ < 1$ for simulations without the wall model, which is sufficient considering the wall as RANS-resolved. Meshes are then composed of $480 \times 140 \times 90$ and $480 \times 160 \times 90$ cells respectively. The calculations are initialised by the RANS results previously computed. In the following calculations, the time-averaged velocity fluctuations $u'u'$ and $u'v'$, the time-averaged velocity and Cp, are extracted from the results and compared with experimental data.

5.1.1 Forcing hybrid formulation

One of the drawbacks of LES is the triggering of turbulence. In some cases, a forcing method is necessary to perturb the flow and generate turbulence. Synthetic turbulence creation methods are generally based on time-averaged data and sometimes RMS data combined with random fluctuations. A simple forcing method consists of embedding noise, applied on the time-averaged data, into the flow. Moreover, advanced methods enable the incorporation of spatially and temporally coherent structures. The Synthetic Eddy Method (SEM), developed by Lund *et al.* (1998), improved by Jarrin *et al.* (2006) and later by Pamies *et al.* (2009), is one of these methods. The formulation of the SEM considers the anisotropy of the near-wall turbulence. The boundary layer is divided into different parts in which structures are generated depending on the wall distance. The characteristics of the structures are set based on experimental observations to approach the physical behaviour of the turbulence. Another advanced method used in the literature is the Random Fourier Modes (RFM) method initiated by Kraichnan (1970), used as the Stochastic Noise Generation and Radiation method (SNGR) by Bechara *et al.* (1994) and improved later by Batten *et al.* (2002) to include the anisotropy. In this method, the

turbulent field is built as a sum of independent Fourier modes with amplitudes based on the known energy spectrum of turbulence.

The current study selects a simple noise forcing method with only a random fluctuation applied on the time-averaged velocities. This choice is justified by the short remaining time for the current study and the fact that the necessary time for developing the advanced methods was long. The noise is randomly calculated using the streamwise velocity component to perturb the three velocity components:

$$\begin{cases} u_{forcing} = u + (0.05 - 0.1\Pi)u, \\ v_{forcing} = v + (0.01 - 0.02\Pi)u, \\ w_{forcing} = w + (0.02 - 0.04\Pi)u, \end{cases} \tag{5.1}$$

with Π a random real between 0 and 1. The forcing of the streamwise, spanwise and vertical velocities are randomly perturbed respectively by 10%, 4% and 2% of the streamwise velocity. This basic forcing method is selected for the computation in case of a low turbulence rate measured into the flow. The forcing is then applied at the plan $x^* = -1.0$ with a height corresponding to the hump one.

5.1.2 DDES

The Delayed Detached-Eddy Simulation selected for the computation is presented in Sec. 2.3.1. Tests are run with both formulations using Δ_{max} of the original DDES and Δ_{new} of the Type II ZDES. Figure 5.1 highlights the distribution of RANS and LES areas for the DDES using Δ_{max}. The lower part of the boundary layer is correctly set to be solved with the RANS formulation.

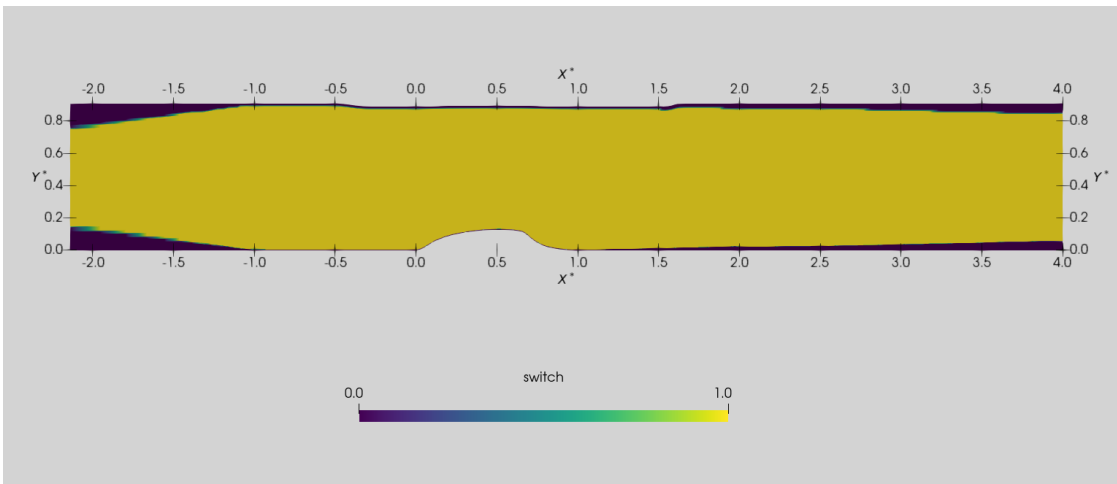

Figure 5.1: Switch of the between the RANS (= 0) and the LES (= 1) areas for the DDES model on the midspan slice of 3-D NASA hump configuration.

The time-averaged velocity profiles are depicted in Fig. 5.2. The numerical results are in good agreement with the experimental data in the five first locations and close to both the experiment and the results from CFL3D for the last three ones. Thus, the use of the DDES formulation preserves the correct time-averaged flow.

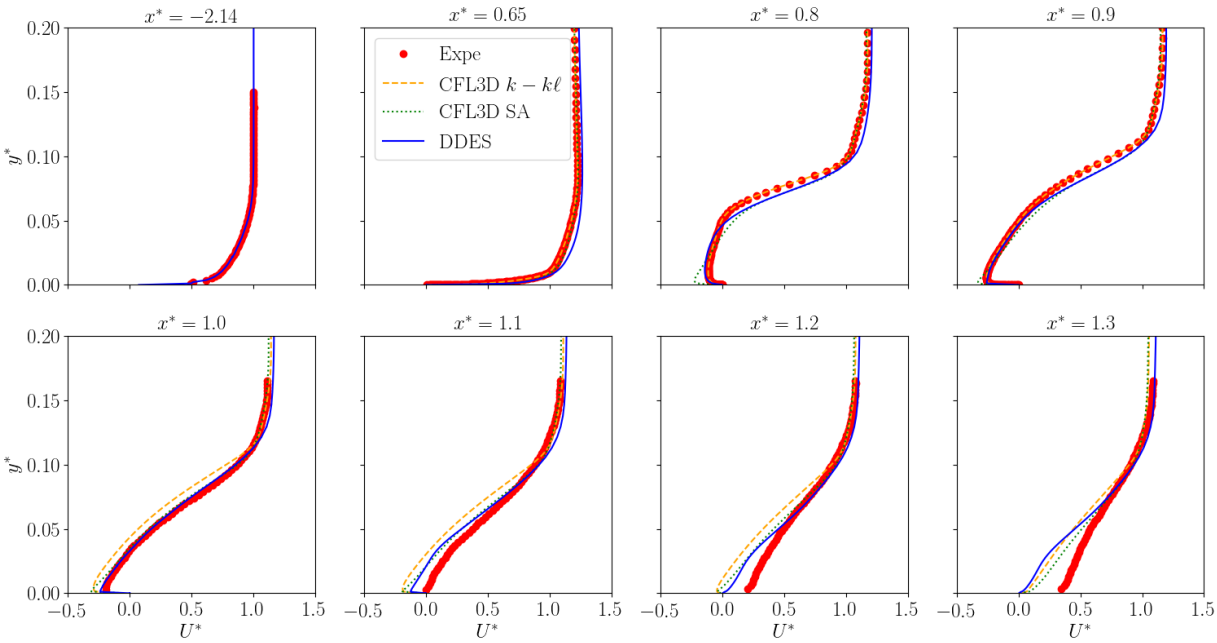

Figure 5.2: Velocity profiles extracted at eight streamwise locations of the NASA hump from the experiment and DDES computation.

Thereafter, this hybrid method should approach the velocity fluctuation experimentally observed in the flow. Figure 5.3 shows the mean velocity fluctuation defined by:

$$U'V' = \frac{1}{N}\sum_{1}^{N}(u-\bar{u})(v-\bar{v}), \tag{5.2}$$

where $\overline{(\cdot)}$ symbolises the time-averaged value and N the number of snapshots set to 940 in the present. In the two first positioning, a peak is observed close to the wall around the switch area of the hybrid method. Downstream, the numerical results highlight a correct maximum intensity of fluctuation not always captured at the right height. The triggering of this peak of fluctuations is not clearly identified since it has been detected for cases using both Δ_{max} and Δ_{ω}, using the forcing method or not and with and without wall model. Nonetheless, more realistic forcing methods (synthetic turbulence methods for example) could lead to better results and correct the discrepancy.

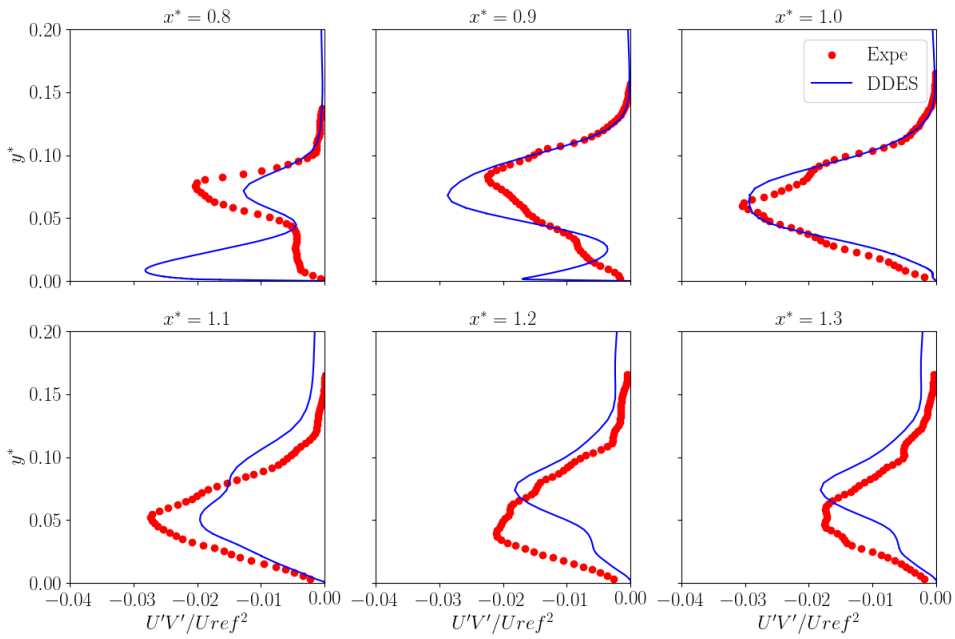

Figure 5.3: Velocity fluctuation profiles extracted at six streamwise locations of the NASA hump from the experiment and DDES computation.

5.1.3 DES $k - \ell$

The $k - \ell$ Detached-Eddy Simulation model developed in Sec. 2.3.2 is tested on the NASA hump case. Nevertheless, the computation shows close results to the ones observed in the 3-D URANS computation. The switch seems to be poorly defined for this case since the domain is almost entirely defined in RANS if the shielding functions are used. In addition, without these functions, LES areas are defined directly next to walls. The velocity fluctuations are inspected for the results from the computation with the F_1 shielding function. It turns out that the fluctuations are widely under-predicted by the model. Thus, the use of the $k - \ell$ DES methods, built with the three shielding functions, is not validated for the NASA hump case. However, the development of an adequate shielding function of the low part of the boundary layer could be investigated. The definition of the switch zone, depending only on the turbulent length and the grid size, is an asset for the reliability of the solving of LES areas. The grid size is assumed to be sufficiently small for the LES solving, contrary to the case of hybrid methods based on the wall distance. In that case, areas far from walls with a coarse grid could still be solved with LES formulation and distorted the result.

5.1.4 ZDES type III

The Type III Zonal Detached-Eddy Simulation is introduced in Sec. 2.3.3. The switch location from RANS to LES is defined around a wall distance of $d_W^{int} = 0.1\delta_{99}$ as recommended by Stich *et al.* (2018). RANS formulation is imposed upstream the location $x^* = -1.0$ and downstream $x = 2.0$, since the zone of high interest is located between these two limits. The forcing method is then applied at the RANS/LES boundary. Moreover, both the Δ_ω and the Δ_{max} are investigated, and the second one is selected for further computations. Figure 5.4 depicts the positioning of the different areas depending on the switch.

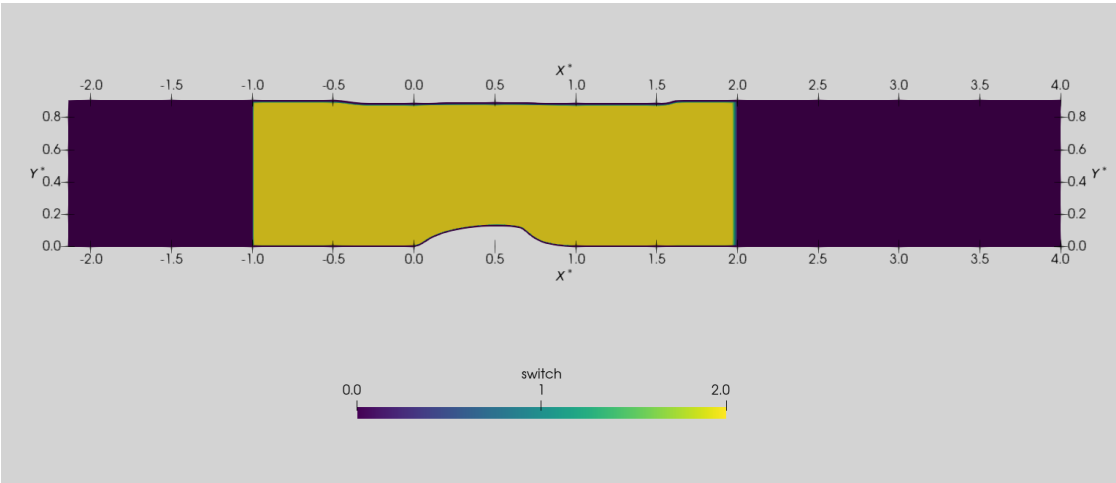

Figure 5.4: Switch between the RANS (= 0), interface (= 1) and the LES (= 2) areas for the Type III ZDES model on the midspan slice of 3-D NASA hump configuration.

The time-averaged velocity profiles are inspected in Fig. 5.5 and compared to experimental and other numerical data. The inflow profile is in perfect agreement with the experimental data at $x^* = -2.14$. Then, the three following profiles agree with the experiment, and the four last are close to both the experimental and numerical results. Hence, as observed with DDES, the correct time-averaged flow is preserved by the use of the Type III ZDES.

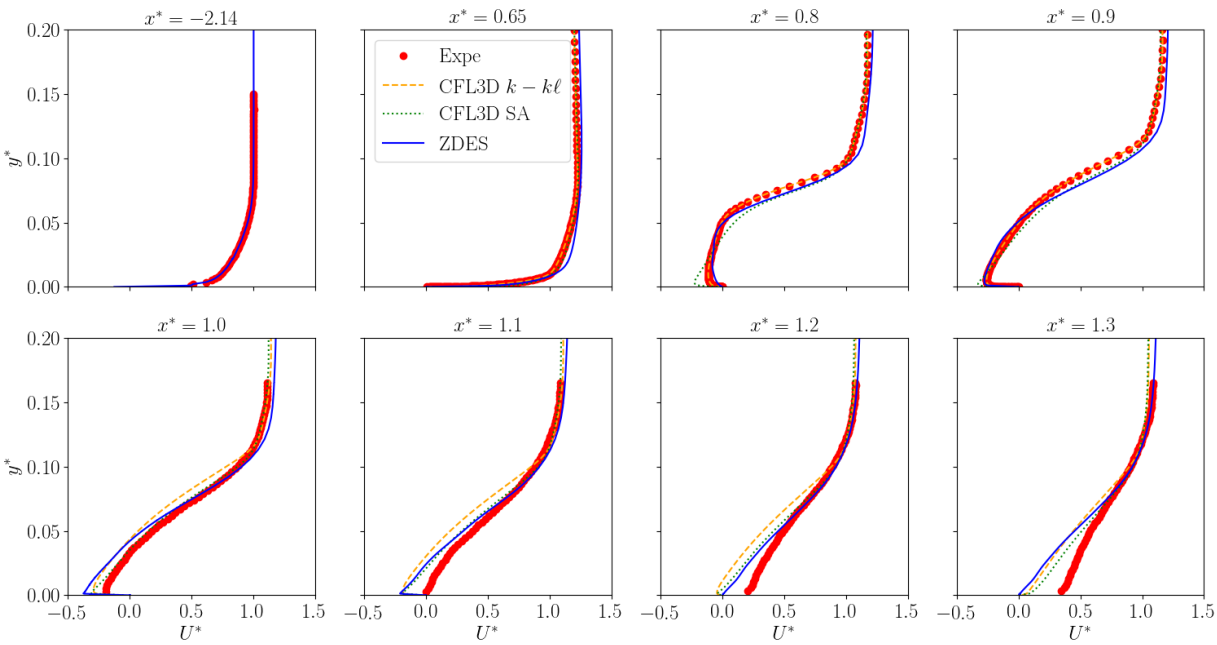

Figure 5.5: Velocity profiles extracted at eight streamwise locations of the NASA hump from the experiment and Type III ZDES computation.

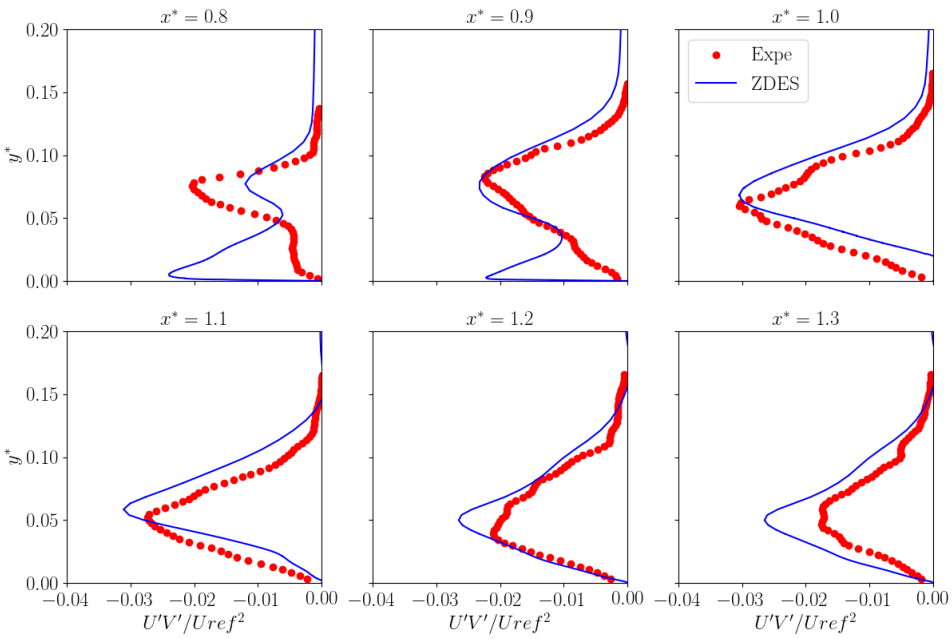

Figure 5.6: Velocity fluctuation profiles extracted at six streamwise locations of the NASA hump from the experiment and Type III ZDES computation.

Velocity fluctuations, computed with Eq. (5.2), observed from the ZDES formulation data are introduced in Fig. 5.6. At the locations $x^* = 0.8$ and $x^* = 0.9$, a peak of fluctuation is detected, as with the results based on the DDES. Nonetheless, the numerical data show a correct agreement with the experiment at the following locations, despite a slight upward shift at $x^* = 1.0$ and $x^* = 1.1$.

5.1.5 Summary

Despite the discrepancies observed with the DDES and the ZDES methods on the velocity fluctuations, encouraging results are observed. The fluctuations are poorly captured close to the wall and well estimated farther at the beginning of the recycling bubble. Nonetheless, the capture is improved downstream, especially after the re-attached location and the fluctuation intensity is correct at all locations.

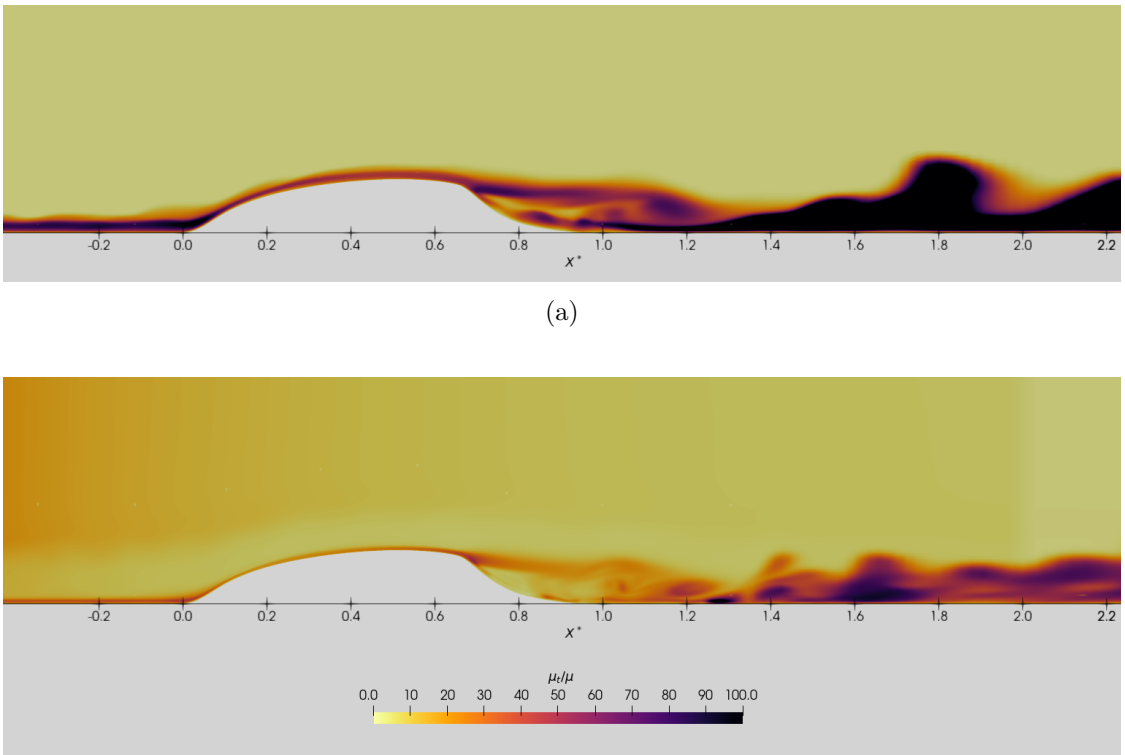

(a)

(b)

Figure 5.7: Snapshot of the turbulent viscosity over viscosity on the midspan slice of 3-D NASA hump configuration; (a) for the DDES model, (b) for the Type III ZDES model.

Figure 5.7 presents the turbulent viscosity over the viscosity μ_t/μ from the results of both DDES

and ZDES computations. Stich *et al.* (2018) observed, in their computations, a delay in the development of 3-D structures in the separated shear layer using the DDES without any forcing methods. This inaccuracy was corrected by the use of the Synthetic Eddy Method (SEM) forcing method. In the present case using the forcing method, the delay is also corrected as seen in Fig. 5.7a. However, the turbulent viscosity shows higher values than in the Stich *et al.* case. Hence, the development of the SEM method could improve the present simulations and correct the discrepancies since it is a more consistent forcing method.

For the Type III ZDES results of Fig. 5.6 more coherent values of the turbulent viscosity are observed, and no delay of 3-D structures development is identified. The use of the forcing method, not selected in the Type III ZDES in Stich *et al.* (2018), seems to improve the turbulent viscosity estimation. Nonetheless, the discrepancies in the velocity fluctuations capture could be corrected by using a coherent forcing method without deteriorating the turbulent viscosity generation.

Thus, further hybrid formulation work is required to equip the current software with a validated hybrid RANS/LES tool.

5.2 Hybrid RANS/LES method for sheet cavitation flow within the venturi configuration

Following the study of hybrid methods, the selected ones are applied to the Venturi case. It has to be noticed that the part of the geometry upstream the throat or farther downstream could also be computed using a RANS resolution. The results presented in this section are only a sketch of the computation using hybrid RANS/LES methods and deserve to be furthered to be correctly analysed. Nonetheless, this work gives an orientation for future works on quasi-stable simulation using RANS/LES hybrid methods. The Venturi configuration with a 4° divergence angle, used in Chapter 4, is selected to perform the study. The Reboud turbulent viscosity correction is applied only on the RANS part of the simulation. The mesh is built so that the first cell, in the wall-normal direction, corresponds to y^+ around 15. Then, the following cells, farther to the wall, are refined to correctly capture the flow dynamics by triggering the switch to the LES computation.

5.2.1 Detached Eddy Simulation with $k - \ell$

Regarding the results of the previous work using a URANS approach with the $k - \ell$ turbulence model, the development of a hybrid RANS/LES method based on this model seems to be a rational choice. The formulation proposed at Sec. 2.3.2 is used to perform sheet cavitation simulation within the 4° divergence angle Venturi configuration.

The use of the $k - \ell$ DES without shielding function is first studied. The results show that the switch between RANS and LES occurs too close or directly to the wall, which does not correspond to the objective of keeping a RANS type resolution at walls. Furthermore, the flow is computed at the wall using a wall model defined for the RANS formulation, which is not consistent with the LES approach. Thus, the boundary layer should be partially "protected" to be resolved with the RANS formulation.

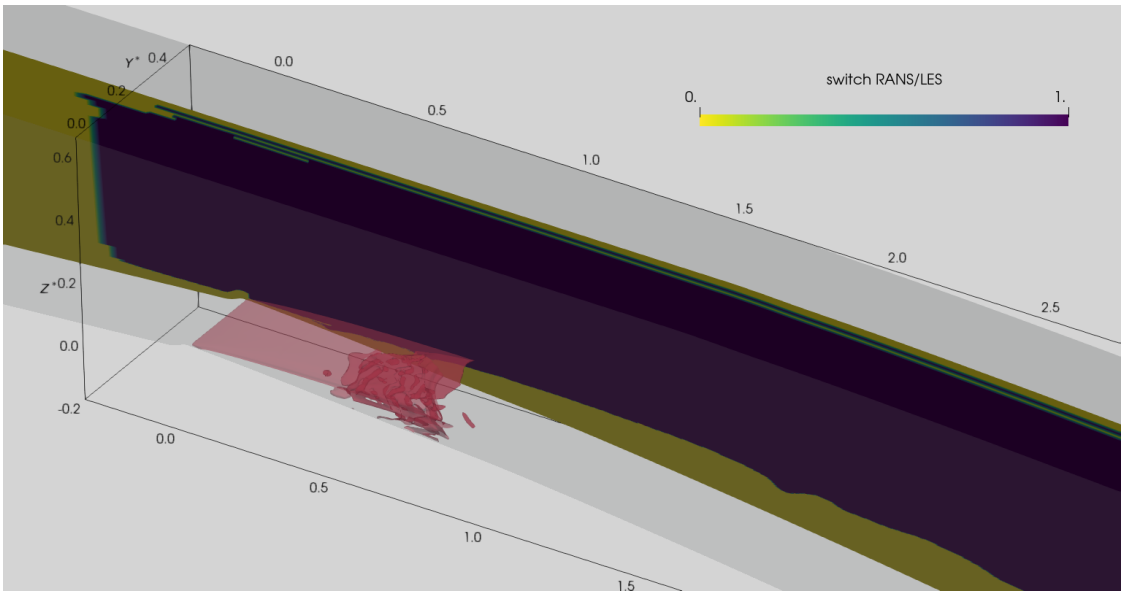

Figure 5.8: Snapshot of the Venturi flow computed with the $k - \ell$ DES model. The 0.5 α contour is depicted in transparency and the midspan slice displays the switch between the RANS ($= 0$) and the LES ($= 1$) models.

Several shielding functions are investigated to protect the boundary layer. The first one is the "delayed" function, introduced for the DDES by Spalart and symbolised by f_{DDES}. The two other ones are extracted from the formulation of the $k - \omega$ SST model and re-framed for the current model as presented in Sec. 2.3.2 as F_1 and F_2. The results of the computations based on these functions show

good protection of the boundary layer, as observed in Fig. 5.8. Nonetheless, the flow is impacted by the switch position, which distorts the results, as observed in Fig. 5.9 with F_1. The re-entrant jet is oversized, which provokes the appearance of a shear layer not observed in the experiment. Hence, the current $k - \ell$ DES formulation with the functions f_{DDES}, F_1 and F_2 do not seem to be appropriate to describe a sheet cavitating flow with a re-entrant jet. The influence of the switch on the cavitating flow is clearly demonstrated for this hybrid method.

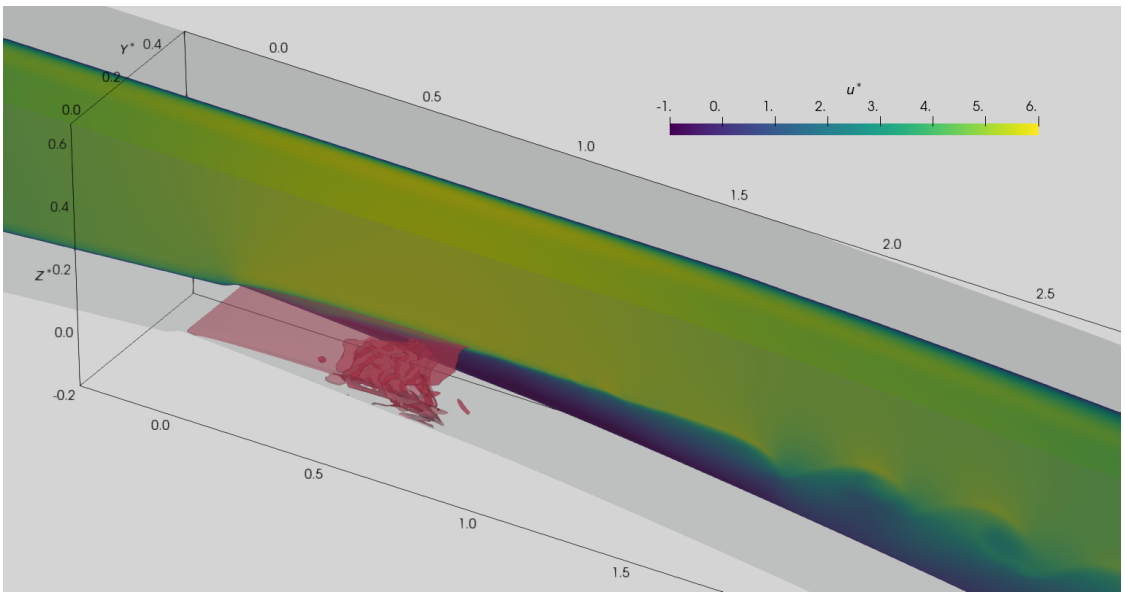

Figure 5.9: Snapshot of the Venturi flow computed with the $k - \ell$ DES model. The 0.5 α contour is depicted in transparency and the midspan slice displays the streamwise velocity u^*.

5.2.2 Delayed Detached-Eddy Simulation (DDES)

The DDES, the most commonly used hybrid RANS/LES method, is applied to the current cavitating flow. The RANS part corresponds to the Spalart-Allmaras model. URANS simulations of the cavitating flow were carried out in 2-D using this model, and a correct agreement was found with experimental data. Therefore, the use of the DDES is justified for this Venturi configuration. Figure 5.10 gives an overview of the RANS and LES areas. The switch is correctly set close to the wall.

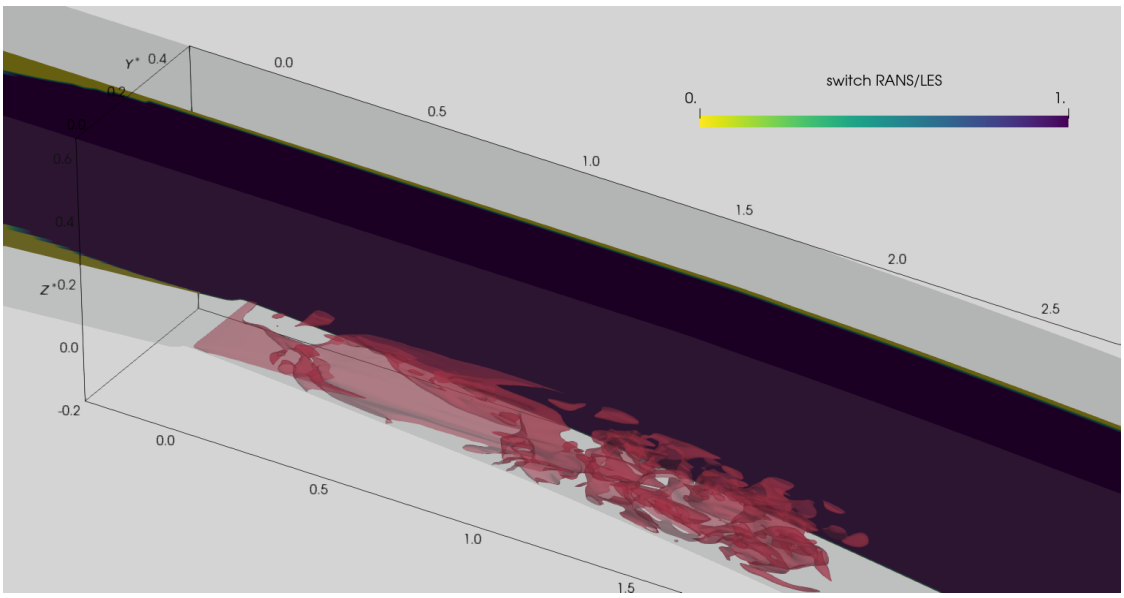

Figure 5.10: Snapshot of the Venturi flow computed with the DDES model. The 0.5 α contour is depicted in transparency and the midspan slice displays the switch between the RANS ($= 0$) and the LES ($= 1$) models.

Nevertheless, the behaviour of the vapour cavity and the re-entrant jet, depicted in Fig. 5.11, is not conformed with the experimental observations. The cavitating flow regime is modified, and large vapour sheddings appear.

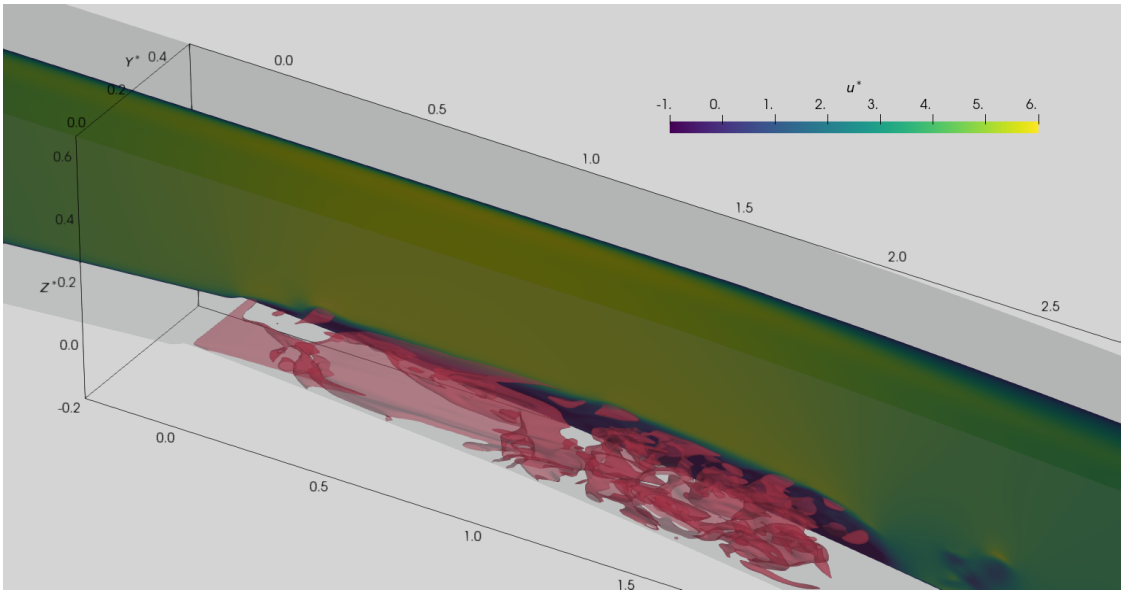

Figure 5.11: Snapshot of the Venturi flow computed with the DDES model. The 0.5 α contour is depicted in transparency and the midspan slice displays the streamwise velocity u^*.

5.2.3 Zonal Detached-Eddy Simulation (ZDES) Type III

The ZDES Type III is based, like the DDES, on the Spalart-Allmaras RANS model. The selection of this method for the computation of the sheet cavitation configuration is also justified. The flow is computed with the RANS formulation upstream $x^* = -0.5$ and downstream $x^* = 3.0$. Between these two locations, the switch takes place at $d_W = 0.1\delta_{99}$. The switch zone can be observed in Fig. 5.12.

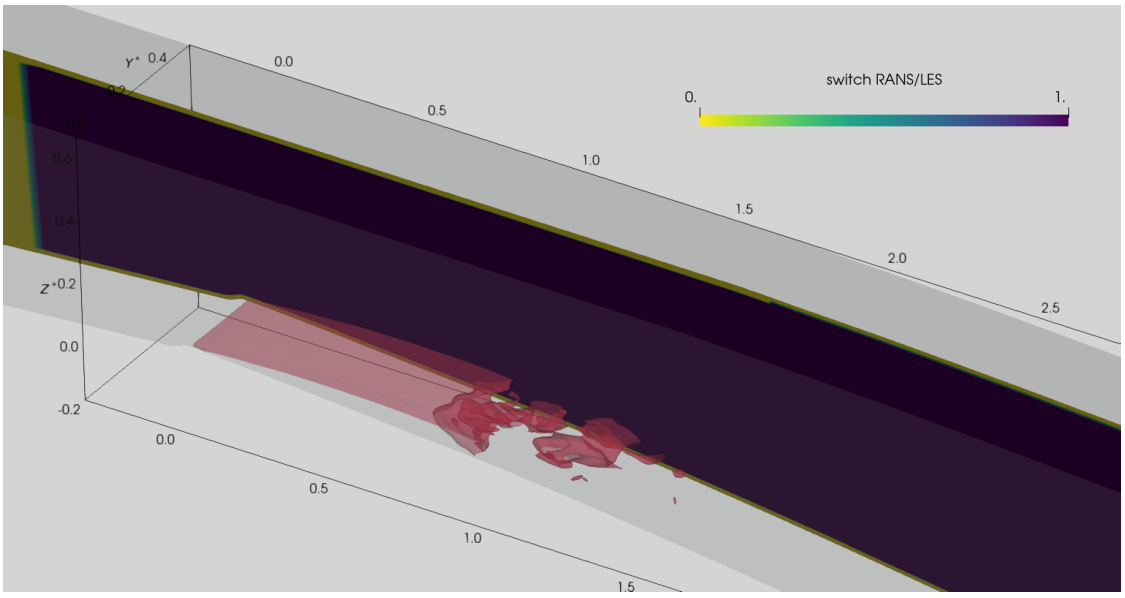

Figure 5.12: Snapshot of the Venturi flow computed with the ZDES model. The 0.5 α contour is depicted in transparency and the midspan slice displays the switch between the RANS (= 0) and the LES (= 1) models.

Moreover, Fig. 5.13 highlights the streamwise velocity and the vapour pocket. The behaviour of the pocket and the re-entrant jet corresponds, during the beginning of the computation, to experimental and numerical observations. However, once the simulation runs for a longer time, the cavitating flow regime is perturbed, and the pocket completely sheds into the flow.

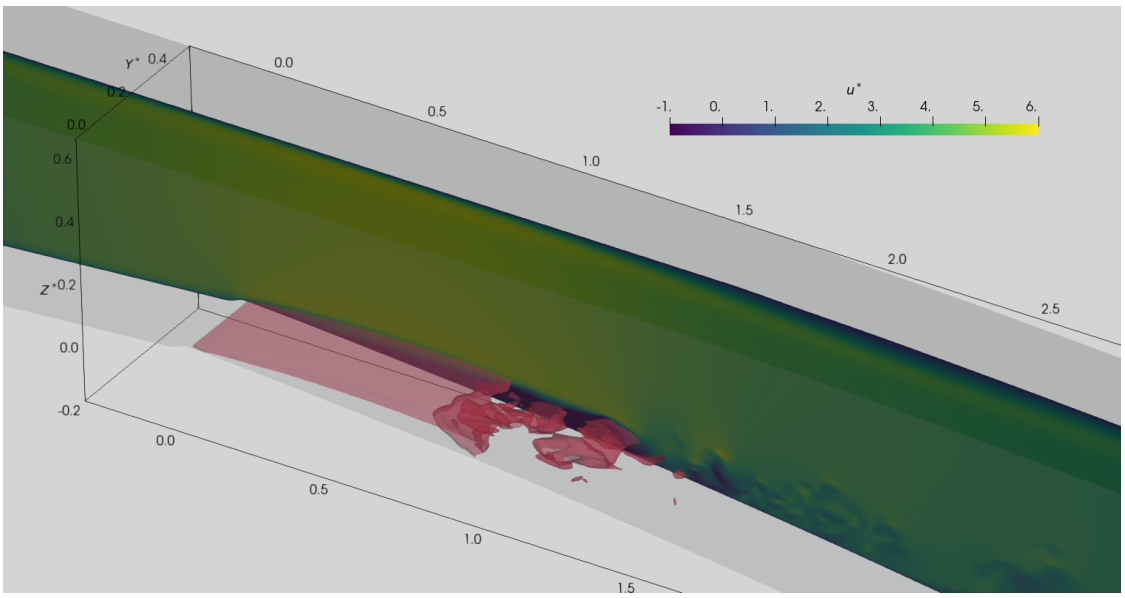

Figure 5.13: Snapshot of the Venturi flow computed with the ZDES model. The 0.5 α contour is depicted in transparency and the midspan slice displays the streamwise velocity u^*.

5.2.4 Summary

A first sketch of computations of sheet cavitation flow was proposed. The influence of the switch area on the flow was proved. Nevertheless, the modification of the flow regime could be explained by a low turbulence rate due to the use of LES methods. As seen with the NASA hump flow, the addition of a forcing method could correct this deficit of turbulence. Further works are required to add a coherent forcing method and investigate its influence on this cavitating flow.

Conclusion and Perspectives

Contents

5.3 Conclusion **127**
5.4 Perspectives **129**

5.3 Conclusion

The present PhD thesis studies the sheet cavitation through different approaches. First, the context of the study was presented with the description of this complex phenomenon based on numerous experimental studies. It was underlined that the vapour pocket behaviour depends on some key parameters such as the cavitation number or the incidence angle. The cavity dynamics is categorised into two main parts: cloud cavitation with the shedding of large clouds into the flow linked to the pocket streamwise oscillation and quasi-stable cavitation with a quasi-constant length cavity and small shedding. The first category was well studied experimentally and numerically. Moreover, a list of the main cavitation models used in the literature was introduced. Similarly, the work on the turbulence simulation was summed up with numerous methods from the inviscid one to the LES.

In the following, the system of equations and the main hypotheses were set. The two-phase flow was considered as a mixture flow with a void ratio describing the fraction of presence of both phases. Equilibrium of the velocities, pressure and temperature between vapour and liquid was essential hypotheses to build the system. Furthermore, in addition to the classical compressible Navier-Stokes equations, a transport equation of the void ratio was established, including a mass transfer source term. The system of equations was closed by two different equations of state depending the saturation vapour pressure: the stiffened gas and the sinusoidal EOS. The choice RANS and hybrid RANS/LES

turbulence modelling methods were described in detail. Thereafter, the numerical choices were described. A third-order explicit time-marching method (SSPRK3) and a third-order centered scheme with dissipation (JST) are selected for computations. The software *Caviflow* was introduced, and the performances were analysed. The software development was validated using non-cavitating and cavitating flows for the URANS approach.

Thereupon, the study of partial cavity dynamics was carried out on a Venturi flow. Two configurations were used for the study: one with sidewalls and one with periodic side boundaries. The time-averaged revealed two different cavity and re-entrant jet shapes. Nonetheless, dynamics analyses, such as SPOD, underlined a dominant mode associated with the same frequency in both cases. For the case with sidewalls, the dynamic was linked to a spanwise oscillation of the cavity and the re-entrant jet in opposition of phase, while for the periodic case, only small sheddings are observed in the cavity closure. There were two modes associated with the frequency for this last case, with opposite directions of dynamics and quasi-identical energy. The choice of the characteristic length and velocity is discussed regarding the Strouhal number. It appeared that the use of the maximum re-entrant jet time-averaged velocity combined with the mean cavity length gave a Strouhal number close to 1. Therefore, it can be concluded that the dominant flow dynamic was unrelated to the presence of sidewalls and was inherent to the sheet cavity development. The extracted frequency was similar to the ones presented in numerous works on cloud cavitation.

Finally, hybrid RANS/LES formulations were proposed and added to the software to pursue sheet cavitation dynamics study using higher-fidelity data. Simulations over non-cavitating and cavitating flows were run with questionable results. The positioning of the switch area between RANS and LES seemed to affect the cavitating flow by changing its behaviour. Thus, the closeness between the vapour pocket and the re-entrant jet with the switch zone was identified as an important concern.

5.4 Perspectives

Regarding the hybrid RANS/LES results observed in the present PhD thesis, the definition of a hybrid method adapted for sheet cavitation simulation is a challenging task. Nonetheless, the contribution of such methods would give great perspectives for sheet cavitation dynamics analyses. Since the triggering of turbulence is a recurrent problem with LES formulations, the development of consistent forcing method, as the Synthetic Eddy Method (SEM), could improve the accuracy of simulations and correct the discrepancies of the different hybrid formulations.

Innovative tools, such as SPOD, could be used on the current sheet cavitation case, using the hybrid RANS/LES approach, to study in detail the vapour pocket oscillation and the role of the re-entrant jet. Furthermore, the triggering mechanism could be identified and studied by using stability analysis methods. This deepened study would lead to a better description and understanding of the phenomenon.

Another sheet cavitation regime could be investigated, such as the complete pocket oscillation observed in the 8° divergence angle Venturi configuration. The dynamic of this unsteady flow with large vapour sheddings could be studied using the same tools as the ones selected for the 4° Venturi. The development of hybrid methods to simulate this Venturi flow is required to properly describe the flow behaviour and rely on more accurate data to study the dynamics. A link between the triggering mechanisms of the dynamic in both regimes could be explored.

Appendix

A - Development of the void ratio transport equation

The system formulation and the present development is based on the reduction of 2-fluid methods in a 5-equation homogeneous system proposed by Kapila *et al.* (2001) with the addition of thermal equilibrium and the gathering of mass conservation equation of both phases in only one equation on the mixture.

The first step of the transport equation development involve mass conservation equation of both phases with an interface mass transfer term $\dot{m}$ from vapour to liquid

$$\frac{\partial \alpha \rho_v}{\partial t} + \frac{\partial \alpha \rho_v u_{vj}}{\partial x_j} = \dot{m}, \tag{3}$$

$$\frac{\partial (1-\alpha) \rho_v}{\partial t} + \frac{\partial (1-\alpha) \rho_v u_{lj}}{\partial x_j} = -\dot{m}. \tag{4}$$

The development of these both equations and the addition of phase speed of sound give:

$$\frac{\rho_v c_v^2}{\alpha}\left(\frac{\partial \alpha}{\partial t} + u_{vj}\frac{\partial \alpha}{\partial x_j}\right) + c_v^2\left(\frac{\partial \rho_v}{\partial t} + u_{vj}\frac{\partial \rho_v}{\partial x_j}\right) + \rho_v c_v^2 \frac{\partial u_{vj}}{\partial x_j} = \frac{\dot{m} c_v^2}{\alpha}, \tag{5}$$

$$-\frac{\rho_l c_l^2}{1-\alpha}\left(\frac{\partial \alpha}{\partial t} + u_{lj}\frac{\partial \alpha}{\partial x_j}\right) + c_l^2\left(\frac{\partial \rho_l}{\partial t} + u_{lj}\frac{\partial \rho_l}{\partial x_j}\right) + \rho_l c_l^2 \frac{\partial u_{lj}}{\partial x_j} = -\frac{\dot{m} c_l^2}{1-\alpha}. \tag{6}$$

The next step is the gathering of (5) and (6) in one transport equation of void ratio. For that purpose, a mechanical equilibrium between phases is considered and the flow is supposed locally isentropic, which gives:

$$c_v^2\left(\frac{\partial \rho_v}{\partial t} + u_{vj}\frac{\partial \rho_v}{\partial x_j}\right) = c_l^2\left(\frac{\partial \rho_l}{\partial t} + u_{lj}\frac{\partial \rho_l}{\partial x_j}\right). \tag{7}$$

Moreover, the hypothesis of kinetic equilibrium is presumed:

$$u_l = u_v = u_m. \tag{8}$$

Then, by subtracting (6) to (5) and applying the previous hypothesis, the following formulation is expressed:

$$\frac{\partial \alpha}{\partial t} + u_{mj}\frac{\partial \alpha}{\partial x_j} = \frac{\rho_l c_l^2 - \rho_v c_v^2}{\frac{\rho_l c_l^2}{\alpha} + \frac{\rho_v c_v^2}{1-\alpha}}\frac{\partial u_{mj}}{\partial x_j} + \dot{m}\frac{\frac{c_l^2}{1-\alpha} + \frac{c_v^2}{\alpha}}{\frac{\rho_l c_l^2}{1-\alpha} + \frac{\rho_v c_v^2}{\alpha}}, \tag{9}$$

where the first right-hand side term is a mechanical relaxation one, describing mechanisms without mass transfer, and the second one takes into account the phase change.

Résumé des travaux de thèse

Introduction

Le terme cavitation désigne un changement de phase du liquide vers la vapeur provoqué uniquement par une baisse de pression (figure 14). Ce phénomène peut apparaître dans des écoulements lorsque le fluide accélère puis provoque une baisse de la pression localement. Alors, si la pression passe en dessous d'un certain seuil appelé la pression de vapeur saturante P_{vap}, il y a vaporisation du fluide. Cet événement engendre un certain nombre de différences dans les caractéristiques de l'écoulement qui devient diphasique. De plus, lorsque les zones de vapeur rencontrent des zones à pression plus élevée ($P > P_{vap}$), elles vont tendre à se condenser afin de revenir sous forme liquide. Ce collapse génère alors des ondes de pression à plus ou moins forte intensité qui, dans certains cas, peuvent produire des dégâts aux alentours.

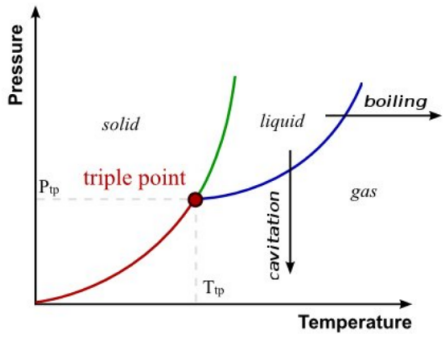

Figure 14: Phénomène de la cavitation représenté sur un diagramme pression-température pour l'eau

Les poches de cavitation apparaissent généralement le long des bords d'attaque de profils ou encore en aval d'un col de venturi et peuvent parfois s'étendre au delà du bord de fuite (supercavitation). Il s'agit d'un phénomène instationnaire qui peut, selon la configuration, générer des lâchers de structures.

Cette dynamique est reliée à la présence d'un écoulement remontant la poche, le long de la paroi, appelé jet rentrant.

Ce type d'écoulement présente un certain nombre de caractéristiques importantes qu'il est nécessaire de prendre en compte pour la simulation:

- forte réduction de la vitesse du son lors du changement de phase et donc la présence de nombre de Mach élevé,
- présence d'instationnarités en fonction des paramètres de l'écoulement,
- forts gradients de masse volumique ($\frac{\rho_l}{\rho_v} \approx 50000$ pour l'eau),
- transferts de masse et thermodynamique hors équilibre,
- interactions avec la turbulence,
- effets tridimensionnels.

Dans le cas étudié, le changement de phase sera considéré comme isotherme car le liquide utilisé n'est pas thermosensible (eau).

La cavitation est souvent identifiée comme un problème dans le domaine de l'hydraulique ou encore dans le domaine de la propulsion. En effet, des structures de vapeur apparaissent le long d'une hélice ou à l'intérieur d'une turbopompe et causent des endommagements lors de leur implosion. Ces dégradations sont principalement l'oeuvre d'ondes de pression générées ainsi que des microjets scindant les bulles de vapeur lors du collapse. Enfin, une autre nuisance engendrée par ce phénomène est le bruit. Par conséquent, les différents comportements de la cavitation font l'objet de nombreuses études afin de remédier à ces problèmes. L'objet de cette thèse se concentre sur un type particulier de la cavitation qui s'appelle la cavitation par poche.

Un moyen d'étudier la dynamique de ces poches est de simuler numériquement leur comportement. Pour étudier cette dynamique, le cas d'un écoulement dans un venturi est choisi car la géométrie est simple et des données expérimentales sont disponibles. L'activité de cette thèse s'inscrit dans la continuité des travaux menés par Goncalvès (Goncalvès, 2013; Goncalvès & Charrière, 2014; Goncalves

& Zeidan, 2018), Decaix (Decaix & Goncalves, 2012, 2013) et Charrière (Charrière, 2015; Charrière *et al.*, 2015; Charrière & Goncalvès, 2017). Dans un premier temps, une revue de l'état de l'art est introduite avec une présentation du phénomène de cavitation par poche en s'appuyant sur des observations tirées de travaux expérimentaux. Puis, une liste non-exhaustive de modèles numériques pour les écoulements cavitants puis pour la turbulence est proposée en se basant sur les principales hypothèses observées dans la litérature. Dans un deuxième temps, le système d'équations, construit pour la simulation de cavitation par poche, est détaillé, et suivi par la description des choix numériques et de l'implémentation dans le code *Caviflow*. Une étude de la dynamique d'une poche quasi-stable de cavitation est ensuite discutée pour un écoulement de type venturi avec une approche URANS. Les résultats sont étudiés et des outils d'analyse tels que des PSD ou des SPOD sont utilisés afin d'identifier les éventuels effets tridimensionnels. Pour finir, des travaux autour des méthodes hybrides RANS/LES sont développés pour une application sur les écoulements cavitants par poche afin d'identifier la contributions de ces méthodes sur les résultats numériques.

Etat de l'art

Le premier chapitre de ce manuscrit s'intéresse au phénomène de cavitation par poche dans la littérature. Un nombre sans dimension très important est introduit : le nombre de cavitation σ, construit comme le rapport de la différence de pression entre la pression statique et la pression de vapeur saturante sur la pression dynamique. Il permet ensuite de catégoriser les différents types d'écoulement cavitant.

Pour commencer, une revue des observations expérimentales permet de décrire en détail ce phénomène complexe. Une poche de cavitation est en générale attachée à un bord d'attaque, ou a un col, et se développe dans le sens de l'écoulement. Deux catégories de poches sont distinguées, les poches quasi-stables qui gardent une taille quasiment identique au cours du temps, et les poches oscillantes avec de gros lâchers de structures de vapeur dans l'écoulement. Dans une majorité des cas, on détecte un autre phénomène très important appelé le jet re-entrant qui est décrit comme un jet principalement liquide remontant l'écoulement sous la poche de vapeur. L'influence du changement de phase sur la vitesse du son est également mesuré : la vitesse du son chute brutalement au niveau de l'interface

liquide-vapeur. D'importantes fluctuations de pression sont observées au niveau de la fermeture de poche ou des lâchers de vapeur. Des ondes de pression sont générées lors du collapse de ces structures.

La description des différents régimes de cavitation par poche est ensuite approfondie en lien avec le nombre de cavitation et l'angle d'incidence de l'écoulement. Plus le nombre de cavitation diminue plus la poche de cavitation tend à osciller et lâcher de grosses structures de vapeur dans l'écoulement et inversement pour l'angle d'incidence. La différence de régime d'écoulement s'exprime également à travers l'épaisseur de la poche et du jet re-entrant, qui est faible dans le cas quasi-stable et plus large dans le cas des lâchers de vapeur, l'intensité du jet y est également plus forte.

Le mécanisme de lâchers de structures de vapeur et de l'oscillation de poche semblent être déclenché par diverse phénomènes. De premières analyses montrent qu'un fort jet re-entrant remonte l'écoulement et à un instant coupe la poche plus ou moins proche, ou au niveau, du bord d'attaque. D'autres études montrent que le collapse des structures de vapeurs génère des ondes de shock qui remontent le long de la paroi, interagissent avec la poche de vapeur et déclenchent le mécanisme. Plus récemment, dans le cas de micro-configurations, des instabilités de Kelvin Helmholtz, localisées à l'interface supérieure de la poche de vapeur, ont été indentifiées comme le mécanisme déclencheur de lâchers de structures et d'oscillation de poche.

De nombreuses études décrivent les caractéristiques principales de la poche de vapeur ainsi que du jet re-entrant en fonction de l'environement et des paramètres de l'écoulement. Le lien entre ces deux mécanismes est prouvé et semble lié au déclenchement d'effets tridimensionnels dans l'écoulement. Certains auteurs identifient une composante non nulle de la vitesse transverse dans le cas d'écoulement par poche de cavitation. Néanmoins, des analyses plus poussées seront nécessaire pour améliorer les connaissances sur ce type d'effet.

L'analyse spectrale de multiples cas d'étude prouve que le mécanisme d'osillation de poche avec lâchers est lié à une fréquence caratéristique (nombre de Strouhal) particulière. Le choix des grandeurs caratéristiques reste à discuter car diffère en fonction des auteurs. Pour finir, les effets de la cavitation et notemment du collapse aux alentours sont listés en fonction des observations expérimentales.

Une revue des orientations numériques est ensuite présentée avec une énumération de différents modèles d'écoulements cavitant relevés dans la littérature suivi d'un bilan des travaux numériques

en fonction du choix de modélisation de la turbulence. La méthode la plus directe pour simuler un écoulement cavitant serait une méthode diphasique. Néanmoins, dû à des problèmes de coût de calcul et de difficulté de capture d'interface avec la création et la destruction d'une phase, la grande majorité des études numériques font le choix d'une méthode dites "1-fluide" dans laquelle l'écoulement est considéré comme un mélange. Deux approches différentes sont alors basées sur cette méthode. La première est un modèle d'équilibre homogène (HEM) dans lequel les équations de mécanique des fluides, couplées à des équations d'états appropriées, sont résolues sans explicitement calculer le transfert de masse entre les phases. La seconde approche est la plus utilisée et se nomme modèle d'équation de transport (TEM). Une équation supplémentaire de transport du taux de présence d'une des phases (ou taux de vide) est ajoutée au système. L'état de l'art du manuscrit énumère un certain nombre de modèles basés sur cette approche.

Par la suite, les méthodes de modélisation de la turbulence dans le cas d'écoulement cavitant par poche sont présentées en partant des modèles non visqueux et en allant jusqu'à la simulation à grandes échelles (LES). L'ensemble de ces approches sont comparées selon divers critères en s'appuyant sur de nombreux travaux numériques.

Système d'équation

La cavitation est un phénomène complexe qui est un cas particulier d'écoulement diphasique avec un changement de phase entre le liquide et la vapeur. En effet, il est possible de voir apparaître et disparaître une phase au cours du temps. Lorsqu'on simule un écoulement compressible avec deux fluides possédant des propriétés physiques et thermodynamiques différentes, on résout généralement les équations d'Euler ou de Navier-Stokes pour chaque fluide, couplés à une équation de suivi d'interface. Il existe plusieurs méthodes permettant de traquer cette interface, mais cela représente un coup de calcul important qui s'ajoute à la complexité de gérer numériquement la création et la disparition d'interface. C'est pourquoi les méthodes dites de mélange sont majoritairement utilisées dans la modélisation d'écoulements cavitants. L'écoulement diphasique y est considéré comme une zone de mélange composée d'une phase vapeur dispersée dans la phase liquide. Le suivi d'interface entre ces deux phases n'est donc plus possible. Afin de simplifier la résolution des équations de conservation, une méthode utilisant un mélange homogène est apparue. La dynamique diphasique est alors apparentée à celle d'un unique fluide. Le coût de calcul en est fortement diminuée, mais des hypothèses

d'équilibre de vitesse, de pression ou encore de température entre les phases sont nécessaires. Les quantités conservatives sont donc dépendantes d'un taux de présence de chacune des phases dans le mélange.

Le taux de présence de chaque phase k est donné par une variable α_k comprise entre 0 et 1 et telle que $\sum_k \alpha_k = 1$. De plus, il est souhaité, dans une première partie de la thèse, une approche basée sur une décomposition des variables de l'écoulement en une moyenne et une fluctuation:

$$u = \overline{u} + u',$$

afin de résoudre seulement les équations pour la moyenne. Les équations obtenues se nomment RANS (Reynolds Averaging Navier-Stokes). Cependant, dans le cas d'écoulements compressibles, ce qui est le cas pour les écoulements cavitants, il est commode d'utiliser une moyenne temporelle (moyenne de Reynolds) pour la densité et la pression, et une moyenne pondérée par la masse (moyenne de Favre) ajoutée à la moyenne temporelle pour les autres variables, soit

$$\tilde{u}_i = \frac{\overline{\rho u_i}}{\overline{\rho}} \ ; \ \tilde{T} = \frac{\overline{\rho T}}{\overline{\rho}} \ ; \ \tilde{e} = \frac{\overline{\rho e}}{\overline{\rho}} \ ; \ \tilde{E} = \frac{\overline{\rho E}}{\overline{\rho}} = \tilde{e} + \frac{\tilde{u}_i \tilde{u}_i}{2} + \frac{\widetilde{u_i'' u_i''}}{2}.$$

Ce qui permet de définir les décompositions suivantes:

$$u_i = \tilde{u}_i + u_i'' \ ; \ \rho = \overline{\rho} + \rho' \ ; \ p = \overline{p} + p' \ ;$$
$$T = \tilde{T} + T'' \ ; \ e = \tilde{e} + e''.$$

Lorsqu'on considère un cas diphasique, une autre moyenne temporelle est nécessaire pour s'appliquer aux variables de chaque phase k. Celle-ci s'applique sur le temps de présence T_k de la phase k et non plus sur le temps global T, d'où :

$$\rho_k = \overline{\overline{\rho}}_k + \rho_k'' \ ; \ u_{k,i} = \tilde{u}_{k,i} + u_{k,i}'' = \frac{\overline{\overline{\rho_k u_{k,i}}}}{\overline{\overline{\rho_k}}} + u_{k,i}''.$$

Et de même pour toute les variables de chaque phase k. On considère maintenant les variables du mélange comme définies à partir des variables phasiques et du taux de présence α_k. On obtient alors:

- une masse volumique du mélange $\rho_m = \sum_k \alpha_k \overline{\overline{\rho}}_k$,
- une pression du mélange $p_m = \sum_k \alpha_k \overline{\overline{p}}_k$,

- une énergie interne du mélange $\rho_m e_m = \sum_k \alpha_k \overline{\overline{\rho_k e_k}}$,
- la vitesse du mélange étant la vitesse du centre de masse $\rho_m u_{m,i} = \sum_k \alpha_k \overline{\overline{\rho}}_k \tilde{u}_{k,i}$,
- la viscosité dynamique du mélange $\nu_m = \sum_k \alpha_k \nu_k$
- le tenseur des contraintes visqueuses du mélange $\sigma_{m,ij} = \overline{\overline{\mu}}_m \left[\frac{\partial \tilde{u}_{m,i}}{\partial x_j} + \frac{\partial \tilde{u}_{m,j}}{\partial x_i} - \frac{2}{3} \frac{\partial u_{m,n}}{\partial x_n} \delta_{ij} \right]$,
- la conductivité thermique du mélange $\lambda_m = \sum_k \alpha_k \lambda_k$,
- la température du mélange à l'interface, en négligeant les fluctuations de température à l'interface soit en supposant l'équilibre thermique à l'interface, $T_m = \overline{\overline{T}}_k$,
- le flux de chaleur du mélange $q_{m,i} = \lambda_m \frac{\partial T_m}{\partial x_i}$.

Par la suite, le choix de considérer un mélange homogène suppose de faire plusieurs hypothèses simplifiant le problème :

- hypothèse de l'équilibre thermique du mélange, soit

$$T_l = T_v = T_m$$

- hypothèse de l'équilibre mécanique, soit

$$p_l = p_v = p_m$$

- hypothèse de mélange homogène qui suppose qu'il n'y a pas de glissement entre les phases ainsi qu'une égalité des vitesses normales à l'interface, soit

$$u_l = u_v = u_m$$

Ces hypothèses permettent de simplifier le système des équations de conservation pour mélange homogène. Tout d'abord, l'égalité des vitesses au sein du mélange permet de faire disparaître le terme d'échange de masse à l'interface. De même pour les échanges de quantité de mouvement à l'interface par les hypothèses d'équilibre cinématique et mécanique. Enfin, les hypothèses d'équilibre thermique,

cinématique et mécanique annulent les termes de transfert d'énergie à l'interface.

Finalement, les équations de conservation moyennées pour un mélange homogène sont

$$\left\{\begin{array}{l}\dfrac{\partial \rho_m}{\partial t}+\dfrac{\partial \rho_m u_{m,j}}{\partial x_j}=0\\ \dfrac{\partial \rho_m u_{m,i}}{\partial t}+\dfrac{\partial \rho_m\, u_{m,i}u_{m,j}}{\partial x_j}=-\dfrac{\partial p_m}{\partial x_i}+\dfrac{\partial \sigma_{m,ij}+\tau_{m,ij}}{\partial x_j}\\ \dfrac{\partial \rho_m\left(E_m+k_m\right)}{\partial t}+\dfrac{\partial\left[\rho_m\left(E_m+k_m\right)+p_m\right]u_{m,j}}{\partial x_j}=\dfrac{\partial\left(\sigma_{m,ij}+\tau_{m,ij}\right)u_{m,j}}{\partial x_j}\\ \qquad\qquad\qquad\qquad\qquad\qquad\qquad\qquad -\dfrac{\partial q_{m,j}}{\partial x_j}-\dfrac{\partial q^t_{m,j}}{\partial x_j}\end{array}\right. \tag{10}$$

avec $\tau_{m,ij}$ le tenseur des contraintes turbulentes, E_m l'énergie du mélange, k_m l'énergie cinétique turbulente du mélange et $q^t_{m,i}$ le flux de chaleur turbulent du mélange:

$$\begin{aligned}\tau_{m,ij} &= \sum_k \alpha_k \tau_{k,ij}=\sum_k -\alpha_k \overline{\overline{\rho_k u''_{k,i}u''_{k,j}}},\\ \rho_m E_m &= \rho_m e_m+\rho_m\frac{u_{m,i}u_{m,i}}{2}\\ \rho_m k_m &= \sum_k \alpha_k\rho_k\frac{\overline{\overline{u''_{k,i}u''_{k,i}}}}{2}\\ q^t_{m,j} &= \sum_k \alpha_k\left(\overline{\overline{\rho_k e''_k u''_{k,j}}}+\frac{1}{2}\overline{\overline{\rho_k u''_{k,i}u''_{k,i}u''_{k,j}}}-\overline{\overline{(p_k-\sigma_{k,ij})u''_{k,j}}}\right)\end{aligned}$$

Modèles de turbulence de type RANS

L'écriture des équations de conservation a fait apparaître deux termes supplémentaires qui sont le tenseur des contraintes visqueuses turbulentes du mélange $\tau_{m,ij}$ et le flux de chaleur turbulent du mélange $q^t_{m,i}$. Afin de fermer le système, il est donc nécessaire d'introduire une modélisation de ces deux quantités.

L'approche au premier ordre propose d'estimer les corrélations doubles des fluctuations de vitesse apparaissant dans les équations de Navier-Stokes moyennées par l'introduction d'une relation algébrique entre contraintes turbulentes et grandeurs physiques moyennes. Par analogie avec la loi de Newton pour les contraintes d'agitation moléculaire, Boussinesq a proposé une relation linéaire pour la

modélisation du tenseur des containtes turbulentes :

$$\tau_{m,ij} = \mu_{tm}\left[\frac{\partial u_{m,i}}{\partial x_j} + \frac{\partial u_{m,j}}{\partial x_i} - \frac{2}{3}\frac{\partial u_{m,n}}{\partial x_n}\delta_{ij}\right] - \frac{2}{3}\rho_m k_m \delta_{ij} \tag{11}$$

avec k_m l'énergie cinétique turbulente. La modélisation du flux de chaleur turbulente suit également une relation linéaire par rapport aux variations de température, analogue à une loi de Fourier :

$$q^t_{m,j} = \lambda_{tm}\frac{\partial T_m}{\partial x_j} \approx \frac{\mu_{tm}C_{pm}}{Pr_t}\frac{\partial T_m}{\partial x_j} \tag{12}$$

Ces fermetures d'équations permettent, à partir d'une relation simple, de calculer des moments d'ordre deux en fonction de variables résolues d'ordre un. Toutes les inconnues sont remplacées par une seule inconnue scalaire : la viscosité turbulente de mélange μ_{tm}. Cette approche implique néanmoins plusieurs hypothèses.

- La turbulence est isotrope aux petites échelles.
- Le tenseur des contraintes turbulentes apparaît dans les équations de Navier Stokes en raison de la non linéarité du terme convectif. Or, la relation de Boussinesq confère à ce tenseur un caractère linéaire et diffusif en contradiction avec son origine.
- La relation de Boussinesq inhibe tous les effets de mémoire propres à la turbulence.

Afin d'obtenir la viscosité turbulente du mélange, il existe diverses modèles à une ou plusieurs équations. Les modèles sélectionnés dans l'étude sont le modèle Spalart-Allmaras (Spalart & Allmaras, 1992) et le modèle $k - \ell$ (Smith, 1990, 1994).

Les modèles de turbulence, développés en majeure partie pour des applications monophasiques, ont tendance à surestimer la valeur de la viscosité turbulente en zone diphasique. Afin d'intégrer le modèle $k - \epsilon$ à un code de cavitation, Reboud *et al.* (1998*b*) propose d'ajouter un limiteur de la viscosité turbulente. Il remplace pour cela la masse volumique ρ_m du mélange par une fonction $f(\rho_m)$ qui modifie l'expression de la viscosité turbulente :

$$\mu_t = f(\rho_m)C_\mu^{1/4}\sqrt{k_m}\ell_m \tag{13}$$

$$f(\rho_m) = \rho_v + \left(\frac{\rho_v - \rho_m}{\rho_v - \rho_l}\right)^n (\rho_l - \rho_v) \tag{14}$$

Cette modification a été appliquée avec succès à d'autres modèles (Coutier-Delgosha *et al.*, 2003; Chen *et al.*, 2006) pour des géométries de type venturi ou hydrofoil en fixant la valeur de $n = 10$ en 2-D et $n = 19$ en 3-D. Decaix et Goncalves ont largement étudié l'influence de cette correction à travers différents travaux (Decaix & Goncalves, 2012, 2013). Ils présentent notamment des études paramétriques de n et témoignent d'une nette amélioration dans la reproduction d'instationnarités caractéristiques des écoulements cavitants. Ce limiteur a donc été utilisé dans ces travaux de thèses pour les modèles $k - \ell$ de Smith et Spalart-Allmaras.

Modèles de turbulence de type Hybride RANS/LES

L'utilisation de méthodes Hybrides permet d'augmenter la résolution de notre problème tout en gardant un coût de calcul abordable. C'est pourquoi le choix s'est vite porté sur celle-ci afin d'améliorer les résultats des simulations RANS dans le cas d'écoulement cavitant. Trois modèles différents sont utilisée dans l'approche Hybride RANS/LES étudiée et décrits en détail dans ce manuscrit. La première s'appelle la DDES, qui est une des méthodes les plus utilisées dans la communauté pour ce type d'approche. La zone de passage entre la résolution RANS et celle LES est imposée en fonction de la distance à la paroi et du rafinement du maillage tout en prenant en compte la couche limite en utilisant une fonction de protection.

Une autre méthode, appelée ZDES, permet de définir directement les zones de passage. Trois types de définition sont proposées. Dans la présente étude la troisième est sélectionnée, permettant de définir manuellement la position de la zone de passage. De plus, afin d'éviter l'apparation de discontinuités au niveau de cette zone, une fonction d'interface est construite pour lisser la transition entre RANS et ZDES.

Les deux méthodes précédentes sont construites à partir du modèle RANS Spalart-Allmaras. Or, de bons résultats sont obtenus avec le modèle $k - \ell$ dans les simulations RANS. C'est pourquoi un modèle Hybride est construit à partir des équations $k - \ell$. Le passage entre RANS et LES se réalise donc en fonction du rafinement du maillage et de la longueur caractéristique locale de la turbulence. Le principal avantage de cette méthode est que le passage en LES est possible uniquement si le maillage est suffisamment rafiné. Une fonction de protection de la couche limite est nécessaire pour maintenir cette zone avec une résolution RANS.

Modèle de cavitation : modèle à 4 équations

La fermeture thermodynamique du système (10) est réalisée à partir d'équations d'état. Afin de modéliser au mieux le changement d'état, il est nécessaire de considérer le fluide selon ses différents états (liquide, vapeur et mélange). Néanmoins, les hypothèses d'équilibre mécanique et thermodynamique permette de rapporter le mélange diphasique à un problème monophasique exprimé à partir des variables de mélange. Prenant en compte ces informations, il sera donc formulé une loi spécifique à une phase pure et une autre au mélange. On définit, pour la suite, le taux de vide α tel que:

$$\begin{cases} \alpha = 0 & \text{si pur liquide} \\ \alpha = 1 & \text{si pur gaz} \end{cases}$$

Dans le modèle utilisé, une quatrième équation est ajoutée au système (10) permettant de calculer directement le taux de vide du mélange qui est considéré comme une quantité convectée par l'écoulement et dont les phénomènes de production et de destruction sont modélisé par le terme source. En combinant les équations de conservation de la masse pour la phase vapeur

$$\frac{\partial \alpha \rho_v}{\partial t} + \frac{\partial \alpha \rho_v u_{v,j}}{\partial x_j} = \dot{m},$$

et pour la phase liquide

$$\frac{\partial (1-\alpha)\rho_l}{\partial t} + \frac{\partial (1-\alpha)\rho_l u_{l,j}}{\partial x_j} = -\dot{m}, \tag{15}$$

avec $\dot{m}$ le débit massique de la phase liquide vers la phase vapeur, il est obtenu l'équation de transport simplifiée par les hypothèses d'équilibre mécanique et cinétique :

$$\frac{\partial \alpha}{\partial t} + u_{m,j}\frac{\partial \alpha}{\partial x_j} = K\frac{\partial u_{m,j}}{\partial x_j} + \frac{\dot{m}}{\rho_I}. \tag{16}$$

Le coefficient K et la masse volumique à l'interface ρ_I sont introduits tels que

$$K = \frac{\rho_l c_l^2 - \rho_v c_v^2}{\dfrac{\rho_v c_v^2}{\alpha} + \dfrac{\rho_l c_l^2}{1-\alpha}} \quad \text{et} \quad \rho_I = \frac{\dfrac{\rho_l c_l^2}{1-\alpha} + \dfrac{\rho_v c_v^2}{\alpha}}{\dfrac{c_l^2}{1-\alpha} + \dfrac{c_v^2}{\alpha}}.$$

Le système complet du modèle à 4 équations est donc la réunion du système (10) et de l'équation de transport (16).

Méthodes numériques

CAVIFLOW est un code de calcul parallèle adimensionné qui utilise les équations de Navier-Stokes compressibles en volume fini et disposant de modèles spécifiques pour modéliser la cavitation. Le système d'équation résolu correspond au système de cavitation à 4 équations auxquelles est ajouté les équations de transport des quantités turbulentes (l'énergie cinétique k et la deuxième quantité dépendant du modèle ψ), soit :

$$\frac{\partial w}{\partial t} + \frac{\partial}{\partial x_j}\left(F_c(w) - F_v(w, w_n)\right) = S(w), \tag{17}$$

où w représente le vecteur des variables conservatives, F_c le vecteur des flux convectifs, F_v le vecteur des flux visqueux et S le vecteur des termes sources comme explicités ci-après.

$$w = \begin{pmatrix} \rho_m \\ \rho_m u_{m,i} \\ \rho_m\left(e_m + k_m\right) \\ \alpha \\ \rho_m k \\ \rho_m \psi \end{pmatrix} \qquad F_c = \begin{pmatrix} \rho_m u_{m,j} \\ \rho_m u_{m,i} u_{m,j} + p_m \\ \rho_m\left(e_m + k_m\right) + p_m \\ \alpha u_{m,j} \\ \rho_m k u_{m,j} \\ \rho_m \psi u_{m,j} \end{pmatrix}$$

$$F_v = \begin{pmatrix} 0 \\ \sigma_{m,ij} + \tau_{m,ij} \\ (\sigma_{m,ij} + \tau_{m,ij}) u_{m,j} - q_{m,j} - q^t_{m,j} \\ 0 \\ \left(\mu_m + \dfrac{\mu^t_m}{\sigma_k}\right)\dfrac{\partial k}{\partial x_j} \\ \left(\mu_m + \dfrac{\mu^t_m}{\sigma_\psi}\right)\dfrac{\partial \psi}{\partial x_j} \end{pmatrix} \qquad S = \begin{pmatrix} 0 \\ 0 \\ 0 \\ (K+\alpha)\dfrac{\partial u_{m,j}}{\partial x_j} + \dfrac{\dot{m}}{\rho_I} \\ \rho_m P_k - \rho_m \psi \\ C_{\psi 1}\rho_m \dfrac{\psi}{k} P_k - C_{\psi 2}\rho_m \dfrac{\psi^2}{k} \end{pmatrix}$$

Méthode de résolution

Les écoulements cavitants associent des zones quasiment incompressibles ($M < 0.1$) de phase liquide et des zones de mélange liquide/vapeur fortement compressibles ($M > 1$). Il a donc été choisi, dans le cadre de la cavitation, de mettre en place une extension d'un solveur compressible vers les écoulements bas Mach afin de résoudre les écoulements avec un tel éventail de nombre de Mach. La solution adoptée se base sur les travaux de Turkel (1987), qui propose de multiplier par une matrice de préconditionnement les termes de dérivées temporelles pour un jeu de variables primitives. Pour le code Caviflow, le vecteur de variables primitives est $W = (p, u, e, \alpha)$. En utilisant une relation de

passage, il est ensuite possible de revenir au vecteur de variables conservatives. Il est présenté, pour une raison de simplicité, les équations d'Euler 1D préconditionnées:

$$P_e^{-1}\frac{\partial W}{\partial t} + A_e\frac{\partial W}{\partial x} = 0, \tag{18}$$

avec A_e la matrice jacobienne des flux convectifs par rapport aux variables primitives,

$$P_e^{-1} = \begin{pmatrix} \frac{1}{\beta^2} & 0 & 0 & 0 \\ 0 & 1 & 0 & 0 \\ 0 & 0 & 1 & 0 \\ 0 & 0 & 0 & 1 \end{pmatrix},$$

et β un paramètre proportionnel au nombre de Mach. La formulation proposée par Choi et Merkle Choi & Merkle (1993) s'écrit :

$$\beta^2 = \min[\max(M^2, \theta M_\infty^2), 1].$$

Ainsi, lorsque le nombre de Mach est supérieur à 1, aucun préconditionnement est appliqué (car $\beta^2 = 1$). Par contre, dans les zones à faible Mach, le préconditionnement est appliqué et peut être contrôlé en utilisant le limiteur θ. Dans les calculs réalisés par la suite θ est pris égal à 3.

Discrétisation temporelle

Un schéma numérique SSPRK 3 (Spiteri & Ruuth, 2002; Gottlieb, 2005) est principalement utilisé pour l'intégration temporelle. C'est un schéma à trois étages est d'ordre trois :

$$\boldsymbol{w}^{n+1} = \boldsymbol{w}^n + h\left(\frac{1}{6}\boldsymbol{k}_1 + \frac{1}{6}\boldsymbol{k}_2 + \frac{2}{3}\boldsymbol{k}_3\right), \tag{19}$$

avec

$$\begin{cases} \boldsymbol{k}_1 &= \boldsymbol{F}(t_n, \boldsymbol{w}_n), \\ \boldsymbol{k}_2 &= \boldsymbol{F}(t_n + h, \boldsymbol{w}_n + h\boldsymbol{k}_1), \\ \boldsymbol{k}_3 &= \boldsymbol{F}(t_n + \frac{h}{2}, \boldsymbol{w}_n + \frac{h}{4}(\boldsymbol{k}_1 + \boldsymbol{k}_2)), \end{cases}$$

où h est le pas de temps et $\boldsymbol{F}$ représente le flux numérique te le terme source de l'équation (17).

Discrétisation spatiale

Le schéma Jameson Schmidt Turkel à l'ordre 2 est composé de deux parties: une partie schéma centré d'ordre 2 et une autre correspondant à la dissipation numérique d'ordre 3. Par exemple, dans le cas de la direction x, sur l'interface $i + \frac{1}{2}$, le flux s'écrit:

$$F_{c_{i+\frac{1}{2},j}} = \frac{1}{2}(F_{c_{i+1,j}} + F_{c_{i,j}}) - D_{1_{i+\frac{1}{2},j}}(w_{i+1,j} - w_{i,j}), \tag{20}$$

où D_1 est un coefficient introduit pour stabiliser le schéma.
Le schéma consiste à ajouter un terme en dérivée première du vecteur w avec un coefficient $\epsilon^{(2)}$ et un terme en dérivée troisième du vecteur w avec un coefficient $\epsilon^{(4)}$. Ces deux termes sont "pilotés" respectivement par des coefficients $k^{(2)}$ et $k^{(4)}$ qui peuvent être ajustés pendant la simulation. Ainsi

$$\begin{aligned} D_{i+1/2,j}(w_{i+1,j} - w_{i,j}) &= \epsilon^{(2)}_{i+1/2,j}\rho(A_{i+1/2,j})(w_{i+1,j} - w_{i,j}) \\ &\quad - \epsilon^{(4)}_{i+1/2,j}\rho(A_{i+1/2,j})(w_{i+2,j} - 3w_{i+1,j} + 3w_{i,j} - w_{i-1,j}), \end{aligned} \quad (21)$$

Le coefficient $\epsilon^{(2)}$ est défini par :

$$\begin{aligned} {\epsilon^{(2)}}_{i+\frac{1}{2},j} &= k^{(2)}\max[\nu_i;\nu_{i+1}] \\ \nu_i &= \frac{|p_{i+1} - 2p_i + p_{i-1}|}{p_{i+1} + 2p_i + p_{i-1}} \end{aligned}$$

$k^{(2)}$ étant un paramètre qui peut être fixé entre 0 et 1. Pour les écoulements cavitants le senseur ν peut être construit sur la masse volumique ρ tel que :

$$\nu_i = \frac{|\rho_{i+1} - 2\rho_i + \rho_{i-1}|}{\rho_{i+1} + 2\rho_i + \rho_{i-1}}$$

Enfin le coefficient $\epsilon^{(4)}$ a pour but d'amortir les oscillations de faibles amplitudes qui empêchent le schéma de converger vers un état stationnaire. Ce terme n'est activé que loin des chocs par la formule :

$${\epsilon^{(4)}}_{i+\frac{1}{2},j} = \max\left[0, k^{(4)} - \epsilon^2_{i+\frac{1}{2},j}\right]$$

avec $k^{(4)}$ un paramètre compris entre $0,008$ et $0,064$.

Le schéma Jameson Schmidt Turkel à l'ordre 3 est une extension du schéma Jameson Schmidt Turkel par rapport à la partie centrée. En effet, la dissipation (21) reste inchangée, et la partie flux centré s'écrit à l'ordre 4, soit

$$F_{c_{i+\frac{1}{2},j}} = \frac{1}{12}(-F_{c_{i+2,j}} + 7F_{c_{i+1,j}} + 7F_{c_{i,j}} - F_{c_{i-1,j}}) - D_{1_{i+\frac{1}{2},j}}(w_{i+1,j} - w_{i,j}), \quad (22)$$

Il est possible de réécrire la dissipation à partir de l'équation (21) en modifiant le terme $\epsilon^{(2)}$. Dans le cas d'écoulements cavitants, il est possible d'intégrer un senseur d'interface à partir de la masse volumique, soit

$$\nu_i^{(I)} = \frac{|\rho_{i+1} - 2\rho_i + \rho_{i-1}|}{\rho_{i+1} + 2\rho_i + \rho_{i-1}}. \quad (23)$$

Le terme $\epsilon^{(2)}_{i+1/2,j}$ se réécrit donc comme une dissipation autour des chocs plus une dissipation autour des interfaces:

$$\epsilon^{(2)}_{i+1/2,j} = \epsilon^{(2)\ shock}_{i+1/2,j} + \epsilon^{(2)\ interface}_{i+1/2,j},$$

avec,

$$\begin{aligned} \epsilon^{(2)\ shock}_{i+1/2,j} &= k^{(2)} \max[\nu_i, \nu_{i+1}], \\ \epsilon^{2\ interface}_{i+1/2,j} &= k^{(2a)} \max[\nu^{(I)}_i, \nu^{(I)}_{i+1}]. \end{aligned}$$

La constante $k^{(2a)}$ est également à choisir et est indépendante du choix de $k^{(2)}$. Cette modification de $\epsilon^{(2)}_{i+1/2,j}$ n'impacte pas $\epsilon^{(4)}_{i+1/2,j}$, c'est-à-dire qu'il s'écrit

$$\epsilon^{(4)}_{i+1/2,j} = \max[0; k^{(4)} - \epsilon^{(2)\ shock}_{i+1/2,j}].$$

Pour conclure cette partie, une étude de scalabilité est présentée pour mesurer les performances du code, suivi de deux cas de validation : le NASA Hump en écoulement non cavitant et un venturi pour le cas cavitant.

Simulation RANS de cavitation par poche dans une configuration de venturi

Le chapitre suivant présente les travaux de simulation d'un écoulement cavitant par poche dans une géométrie d'un venturi utilisée dans les travaux de Barre *et al.* (2009). Les conditions de l'écoulement sont telles que la poche de vapeur est dans une configuration quasi-stable. Des relevés de données expérimentales sont réalisés dans le sens de l'écoulement au milieu de la largeur de la géométrie, ce qui correspond à la position de la poche. Ces données vont servir de comparaisons aux simulations conduites dans cette partie. Le choix des grandeurs caractéristiques est ensuite discuté et la longueur moyenne de la poche ainsi que le maximum de la vitesse moyenne du jet re-entrant sont sélectionnées comme longueur caractéristique et vitesse caractéristique respectivement.

Deux configurations 3-D sont utilisés afin d'étudier les éventuels effets tridimensionnels, la première correspondant à celle de l'expérience, et une autre deux fois plus large ainsi que des conditions périodiques dans la direction transverse. La comparaison des résultats moyennés montre des différences

importantes dans la forme de la poche et du jet. Avec paroi on retrouve une forme symmétrique en U et un jet re-entrant plus développé au milieu du venturi alors que pour le cas périodique leur forme semble être 2-D. La visualisation des images semble montrer une oscillation transverse de la poche pour le cas avec paroi alors que pour le cas périodique il n'est pas possible d'identifier directement une fréquence de dynamique. Une première analyse de la dynamique est ensuite conduite avec des RMS et des cartographies PSD. Un nombre de Strouhal aux alentours de 1 est extrait pour les deux configurations ainsi que les premières harmoniques. La dynamique est identifier au niveau de la fermeture de la poche pour la masse volumique. Pour les vitesses également mais avec une fluctuation propagée dans l'écoulement.

Le comportement du jet re-entrant par rapport à la poche de vapeur est étudié par la suite. Une étude de corrélation montre une opposition de phase dans l'oscillation transverse de la poche dans le cas avec paroi. De plus, le mouvement d'oscillation est identifié comme non homogène. En effet, lorsque la poche se rapproche de la paroi, elle est repoussée rapidement dans l'autre direction, créant une accélération ponctuelle du mouvement.

Pour continuer, une SPOD sur les deux cas d'études est analysée. On retrouve le nombre de Strouhal proche de 1 pour les deux configurations ainsi que les harmoniques. L'analyse des spectres obtenus permet d'identifier clairement le mode dominant associé à l'oscillation pour le cas avec parois latérales. Néanmoins, pour le cas périodique, deux modes semblent partager la même énergie associée. En les regardant de plus près, ils sont identiques mis à part un déplacement transverse dans le sens opposé. Il est alors possible d'assumer ces deux modes comme équiprobables et liés aux effets tridimensionnels.

Enfin, l'identification d'effets tridimentionnels dans la littérature est discutée et et les résultats sont comparés avec ceux obtenus durant les travaux de thèse. Certains auteurs assument que la déformation de la poche déclenche la composante transverse du jet alors que d'autres parlent de l'inverse. Du point de vu de l'auteur il n'est pas possible de conclure sur ce point au vu des informations disponibles. Néanmoins, les travaux réalisés on permis d'identifier des effets tridimensionnels indépendants de la présence de parois. Cela combiné à un Strouhal associé proche de 1 amène à penser que les effets tridimensionnels sont inhérents au développement de la poche de cavitation. Cependant, les parois ont clairement un effet sur la topologie de l'écoulement.

Approche hybryde RANS/LES pour la cavitation par poche

Afin d'étudier l'implémentation des méthodes Hybrides RANS/LES, de premiers tests sont conduits sur la configuration NASA Hump non cavitante. Des résultats encourageants sont identifiés pour les approches DDES et ZDES type III concernant les valeurs moyennes et les fluctuations de vitesse. Néanmoins, sur deux des extractions, au niveau de la bosse, un pic de fluctuation est détecté à tord. Ce pic pourrait être lié à la définition de la zone de passage. Pour l'approche DES $k-\ell$, des difficultés sont observées par rapport à la définition de la fonction de protection. L'étude autour de la définition du modèle mérite d'être approfondie pour la calibrer correctement.

Dans un deuxième temps, des essais de calcul sont réalisés pour un écoulement cavitant dans la configuration du venturi précédemment étudiée. Les résultats DDES montrent une définition correcte des différentes zones mais l'écoulement est fortement modifié avec une poche de cavitation sur-développée. La ZDES de type III donne des résultats proches de ce qui est observé dans les précédents calculs. Cependent, après un certain temps le régime de cavitation est modifié et la poche est totallment relâchée dans l'écoulement. Pour le modèle DES $k-\ell$, la zone de passage n'est pas correctement définie et semble fortement influencer l'écoulement en créant de nouveaux phénomènes non détectés dans l'expérience. L'ensemble de ces observations prouvent qu'un travail plus approfondi sur ces métodes est nécessaire. Il est également possible que l'approche Hybride ne soit pas appropriée pour les écoulements cavitants basés sur un modèle de mélange. En effet, la zone de passage est située dans une zone critique de l'écoulement qui est diphasique avec une dynamique particulière. Les répercutions de cette localisation sont importantes au vu des résultats obtenus.

Conclusion

Les travaux de thèse ont permis dans un premier temps de développer et de valider un outils numérique approprié à la simulation d'écoulement cavitant par poche. De nombreux calculs 2-D et 3-D ont été mené avec les approches RANS et Hybride RANS/LES. Une analyse approfondie d'un écoulement de type venturi a été conduite. Celle-ci a permis d'identifier des effets tridimensionnels déclenchés par l'apparition d'une poche de cavitation dans l'écoulement. Une fréquence liée à ses effets a été relevée et correspond aux fréquences d'oscillation de poche extraites de la littérature. Ces travaux ont abouti à une publication dans un journal de référence. Enfin, une étude de différents

modèles Hybrides RANS/LES a été conduite. Elle a permis d'identifier les points critiques de ce type d'approche pour les écoulements cavitants par poche. Des résultats encourageants ont été trouvé pour le modèle ZDES de type III.

Bibliography

Aeschlimann, V., Barre, S. & Djeridi, H. 2013 Unsteady cavitation analysis using phase averaging and conditional approaches in a 2D Venturi flow. *Open Journal of Fluid Dynamics* **3**, 171–183.

Arabnejad, M.H., Amini, A., Farhat, M. & Bensow, R.E. 2019 Numerical and experimental investigation of shedding mechanisms from leading-edge cavitation. *International Journal of Multiphase Flow* **119**, 123–143.

Arndt, R. A. E., Song, C. C. S., He, M. Kjeldsen J. & Keller, A. 2000 Instability of partial cavitation: A numerical/experimental approach. In *Twenty-Third Symposium on Naval Hydrodynamics*. National Academies Press.

Avellan, F. & Dupont, P. 1988 Etude du sillage d'une poche de cavitation partielle se développant sur un profil hydraulique bi-dimensionnel. *La Houille Blanche* .

Barre, S., Rolland, J., Boitel, G., Goncalves, E. & Patella, R. Fortes 2009 Experiments and modeling of cavitating flows in Venturi: attached sheet cavitation. *European Journal of Mechanics B/Fluids* **28**, 444–464.

Batten, P., Goldberg, U. & Chakravarthy, S. 2002 Reconstructed sub-grid methods for acoustics predictions at all reynolds numbers .

Bechara, W., Bailly, C., Lafon, P. & Candel, S.M. 1994 Stochastic approach to noise modeling for free turbulent flows. *AIAA Journal* **32** (3), 455–463.

Bensow, R. E. 2011 Simulation of the unsteady cavitation on the the Delft Twist11 foil using RANS, DES and LES. In *Second International Symposium on Marine Propulsors*. Hamburg, Germany.

Bhatt, M. & Mahesh, K. 2020 Numerical investigation of partial cavitation regimes over a wedge using large eddy simulation. *International Journal of Multiphase Flow* **122**, 103155.

Brandao, F.L., Bhatt, M. & Mahesh, K. 2019 Numerical study of cavitation regimes in flow over a circular cylinder. *Journal of Fluid Mechanics* **885**.

Brandner, P. A., Walker, G. J., Niekamp, P. N. & Anderson, B. 2010 An experimental investigation of cloud cavitation about a sphere. *Journal of Fluid Mechanics* **656**, 147–176.

Brennen, C.E. 1995 *Cavitation and Bubble Dynamics*. Oxford University Press.

Budich, B., Schmidt, S. J. & Adams, N. A. 2018 Numerical simulation and analysis of condensation shock in cavitating flow. *Journal of Fluid Mechanics* **838**, 759–813.

Callenaere, M., Franc, J.-P., Michel, J.-M. & Riondet, M. 2001 The cavitation instability induced by the development of a re-entrant jet. *Journal of Fluid Mechanics* **444**, 223–256.

Chaouat, B. & Schiestel, R. 2007 From single-scale turbulence mmodel to multiple-scale and subgrid-scale mmodel by fourier transform. *Theoretical and Computational Fluid Dynamics* **21**, 201–229.

Charrière, B. 2015 Modélisation et simulation d'écoulements turbulents cavitants avec un modèle de transport de taux de vide. PhD thesis, Laboratoire des Écoulements Géophysiques et Industrielles.

Charrière, B., Decaix, J. & Goncalvès, E. 2015 A comparative study of cavitation model in a venturi flow. *European Journal of Mechanics B/Fluids* **49**, 287–297.

Charrière, B. & Goncalvès, E. 2017 Numerical investigation of periodic cavitation shedding in a venturi. *International Journal of Heat and Fluid Flow* **64**, 41–54.

Che, Bangxiang, Cao, Linlin, Chu, Ning, Likhachev, Dmitriy & Wu, Dazhuan 2019 Dynamic behaviors of re-entrant jet and cavity shedding during transitional cavity oscillation on NACA0015 hydrofoil. *Journal of Fluids Engineering* **141** (6), 061101.

Chen, Y., Li, J., Gong, Z., Chen, X. & Lu, C. 2019 Large eddy simulation and investigation on the laminar-turbulent transition and turbulence-cavitation interaction in the cavitating flow around hydrofoil. *International Journal of Multiphase Flow* **112**, 300–322.

Chen, Y., Lu, C-J. & Wu, L. 2006 Modelling and computation of unsteady turbulent cavitation flows. *Journal of Hydrodynamics* **18**, 559–566.

Cheng, X., Shao, X. & Zhang, L. 2019 The characteristics of unsteady cavitation around a sphere. *Physics of Fluids* **31**.

Choi, Y.H. & Merkle, C.L. 1993 The application of preconditioning to viscous flows. *Journal of Computational Physics* **105** (2), 207–223.

Chu, B.T. 1965 On the energy transfer to small disturbances in fluid flow (part i). *Acta Mechanica* **1**, 215–234.

Coutier-Delgosha, O., Devillers, J-F. & Pichon, T. 2006 Internal structure and dynamics of sheet cavitation. *Physics of Fluids* **18**.

Coutier-Delgosha, O., Fortes-Patella, R. & Reboud, J. L. 2003 Evaluation of the turbulence model influence on the numerical simulations of unsteady cavitation. *Journal of Fluids Engineering* **125**, 38–45.

Coutier-Delgosha, O., Stutz, B., Vabre, A. & Legoupil, S. 2007 Analysis of cavitating flow structure by experimental and numerical investigations. *Journal of Fluid Mechanics* **578**, 171–222.

Dandois, J. 2014 Improvement of corner flow prediction using the quadratic constitutive relation. *AIAA Journal* **52** (12).

Decaix, J. 2012 Modélisation et simulation de la turbulence compressible en milieu diphasique : application aux écoulements cavitants instationnaires. PhD thesis, Université Grenoble.

Decaix, J. & Goncalves, E. 2012 Time-dependent simulation of cavitating flow with $k - \ell$ turbulence models. *Int. Journal for Numerical Methods in Fluids* **68** (8), 1053–1072.

Decaix, J. & Goncalves, E. 2013 Investigation of three-dimensional effects on a cavitating Venturi flow. *International Journal of Heat and Fluid Flow* **44**, 576–595.

Deck, S. 2011 Recent improvements in the zonal detached eddy simulation (zdes) formulation. *Theoretical and Computational Fluid Dynamics* **26**, 523–550.

Dittakavi, N., Chunekar, A. & Frankel, S. 2010 Large eddy simulation of turbulent-cavitation interactions in a Venturi nozzle. *Journal of Fluids Engineering* **132**.

Downar-Zapolski, P., Bilicki, Z., Bolle, L. & Franco, J. 1996 The non-equilibrium relaxation model for one-dimensional flashing liquid flow. *International Journal of Multiphase Flow* **22** (3), 473–483.

Ducoin, A., Huang, B. & Young, Y.L. 2012 Numerical modeling of unsteady cavitating flows around a stationary hydrofoil. *International Journal of Rotating Machinery* p. 215678.

Dular, M. & Bachert, R. 2009 The issue of Strouhal number definition in cavitating flow. *Journal of Mechanical Engineering* **55** (11), 666–674.

Dular, M., Bachert, R., Schaad, C. & Stoffel, B. 2007 Investigation of a re-entrant jet reflection at an inclined cavity closure line. *European Journal of Mechanics - B/Fluids* **26**, 688–705.

Dular, M., Khlifa, I., Fuzier, S., Maiga, M. Adama & Coutier-Delgosha, O. 2012 Scale effect on unsteady cloud cavitation. *Experiments in Fluids* **53**, 1233–1250.

Dumond, J., Magagnato, F. & Class, A. 2013 Stochastic-field cavitation model. *Physics of Fluids* **25**.

Egerer, C.P., Hickel, S., Schmidt, S.J. & Adams, N.A 2014 Large-eddy simulation of turbulent cavitating flow in a micro channel. *Physics of Fluids* **26**, 085102.

Foeth, E. J., van Doorne, C. W. H., van Terwisga, T. & Wieneke, B. 2006 Time resolved PIV and flow visualization of 3D sheet cavitation. *Experiments in Fluids volume* **40**, 503–513.

Ganesh, H. 2015 Bubbly shock propagation as a cause of sheet to cloud transition of partial cavitation and stationary cavitation bubbles forming on a delta wing vortex. PhD thesis, University of Michigan.

Ganesh, H., Mäkiharju, S. A. & Ceccio, S. L. 2016 Bubbly shock propagation as a mechanism for sheet-to-cloud transition of partial cavities. *Journal of Fluid Mechanics* **802**, 37–78.

Garnier, E., Adams, N. & Sagaut, P. 2009 *Large Eddy Simulation for Compressible Flows*. Springer.

Ge, M., Petkovsek, M., Zhang, G., Jacobs, D. & Coutier-Delgosha, O. 2021 Cavitation dynamics and thermodynamic effects at elevated temperatures in a small Venturi channel. *International Journal of Heat and Mass Transfer* **170**, 120970.

Geng, L. & Escaler, X. 2018 Assessment of RANS turbulence models and Zwart cavitation model empirical coefficients for the simulation of unsteady cloud cavitation. *International Journal of Multiphase Flow* .

Gnanaskandan, A. & Mahesh, K. 2015 A numerical method to simulate turbulent cavitating flows. *International Journal of Multiphase Flow* **70**, 22–34.

Gnanaskandan, A. & Mahesh, K. 2016*a* Large eddy simulation of the transition from sheet to cloud cavitation over a wedge. *International Journal of Multiphase Flow* **83**, 86–102.

Gnanaskandan, A. & Mahesh, K. 2016*b* Numerical investigation of near-wake characteristics of cavitating flow over a circular cylinder. *Journal of Fluid Mechanics* **790**, 453–491.

Goncalves, E. 2015 Modélisation et simulation de la cavitation. In *14e Ecole de Mécanique des Fluides Numérique*. Porquerolles, France.

Goncalves, E. & Patella, R. Fortes 2009 Numerical simulation of cavitating flows with homogeneous models. *Computers & Fluids* **38**, 1682–1696.

Goncalves, E. & Zeidan, D. 2017 Numerical simulation of unsteady cavitation in liquid hydrogen flows. *International Journal of Engineering Systems Modelling and Simulation* **9** (1).

Goncalves, E. & Zeidan, D. 2018 Simulation of compressible two-phase flows using a void ratio transport equation. *Computational Physics* **24**, 167–203.

Goncalvès, E. 2013 Numerical study of expansion tube problems: Towards the simulation of cavitation. *Computers & Fluids* **72**, 1–19.

Goncalvès, E. & Charrière, B. 2014 Modelling for isothermal cavitation with a four-equation model. *International Journal of Multiphase Flow* **59**, 54–72.

Goncalvès, E. & Decaix, J. 2012 Wall model and mesh influence study for partial cavities. *European Journal of Mechanics B/Fluids* **31**, 12–29.

Gopalan, S. & Katz, J. 2000 Flow structure and modeling issues in the closure region of attached cavitation. *Physics of Fluids* **12**, 895.

Gottlieb, S. 2005 On high order strong stability preservingrunge-kutta and multi step time discretizations. *Journal of Scientific Computing* **25**, 105–128.

Greenblatt, D., Paschal, K.B., Yao, C.S. & Harris, J. 2006 Experimental investigation of separation control part 1: Baseline and steady suction. *AIAA Journal* **44** (12).

Hammond, D.A. & Redekopp, L.G. 1998 Local and global instability properties of separation bubbles. *European Journal of Mechanics B/Fluids* **17** (2), 145–164.

Hayashi, S. & Sato, K. 2014 Unsteady behavior of cavitating waterjet in an axisymmetric convergent-divergent nozzle: High speed observation and image analysis based on frame difference method. *Journal of Flow Control, Measurement & Visualization* **2** (3), 94–104.

Hickel, S., Mihatsch, M. & Schmidt, S.J. 2011 Implicit large eddy simulation of cavitation in micro channel flows. *WIMRC 3rd International Cavitation Forum* .

Hidalgo, V., Escaler, X., Valencia, E., Peng, X., Erazo, J., Puga, D. & Luo, X. 2019 Scale-adaptive simulation of unsteady cavitation around a NACA66 hydrofoil. *Applied Science* **9** (18), 3696.

Hirsch, C. 1988 Numerical computation of internal and external flows - fundamentals of numerical discretization, volume I. John Wiley & Sons.

Hirsch, C. 1990 Numerical computation of internal and external flows, volume II. John Wiley & Sons.

Huang, B., Zhao, Y. & Wang, G. 2014 Large eddy simulation of turbulent vortex-cavitation interactionsin transient sheet/cloud cavitating flows. *Computers & Fluids* **92**, 113–124.

Jahangir, S., Hogendoorn, W. & Poelma, C. 2018 Dynamics of partial cavitation in an axisymmetric converging-diverging nozzle. *International Journal of Multiphase Flow* **106**, 34–45.

Jameson, A., Schmidt, W. & Turkel, E. 1981 Numerical solutions of the Euler equations by finite volume methods using Runge-Kutta time-stepping schemes. In *ALAA 14th Fluid and Plasma Dynamics Conference* (ed. AIAA).

Jarrin, N., Benhamadouche, S., Laurence, D. & Prosser, R. 2006 A synthetic-eddy-method for generating inflow conditions for large-eddy simulations. *International Journal of Heat and Fluid Flow* **27** (4), 585–593, special Issue of The Fourth International Symposium on Turbulence and Shear Flow Phenomena - 2005.

Ji, B., Luo, X., Arndt, R.E.A. & Wu, Y. 2014 Numerical simulation of three dimensional cavitation shedding dynamics with special emphasis on cavitation-vortex interaction. *Ocean Engineering* **87**, 65–77.

Ji, B., Luo, X., Peng, X. & Wu, Y. 2013*a* Three-dimensional large eddy simulation and vorticity analysis of unsteady cavitating flow around a twisted hydrofoil. *Journal of Hydrodynamics* **25**, 510–519.

Ji, B., Luo, X., Wu, Y., Peng, X. & Duan, Y. 2013*b* Numerical analysis of unsteady cavitating turbulent flow and shedding horse-shoe vortex structure around a twisted hydrofoil. *International Journal of Multiphase Flow* **51**, 33–43.

Kadivar, Ebrahim, el Moctar, Ould & Javadi, Khodayar 2019 Stabilization of cloud cavitation instabilities using cylindrical cavitating-bubble generators (ccgs). *International Journal of Multiphase Flow* **115**, 108–125.

Kapila, A.K., Menikoff, R., Bdzil, J.B., Son, S.F. & Stewart, D.S. 2001 Two-phase modeling of deflagration-to-detonation transition in granular materials: reduced equations. *Physics of Fluids* **13** (10), 3002–3024.

Kawakami, D.T., Fuji, A., Tsujimoto, Y. & Arndt, R.E.A. 2008 An assessment of the influence of environmental factors on cavitation instabilities. *Journal of Fluids Engineering* **130**, 031303.

Kawanami, Y., Kato, H., Yamaguchi, H., Tanimura, M. & Tagaya, Y. 1997 Mechanism and control of cloud cavitation. *J. Fluids Eng.* **119** (4), 788–794.

Kinzel, M. P., Lindau, J. W., Peltier, L. J. & Kunz, R. F. 2007 Detached-eddy simulations for cavitating flows. In *18th AIAA Computational Fluid Dynamics Conference*. Miami, USA.

Knapp, R.T. 1955 Recent investigations of the mechanics of cavitation and cavitation damage. *Transactions of the ASME* **77**, 1045–1054.

Kraichnan, R.H. 1970 Diffusion by a random velocity field. *The Physics of Fluids* **13** (1), 22–31.

Kubota, A., Kato, H., Yamaguchi, H. & Maeda, M. 1989 Unsteady structure measurement of cloud cavitation on a foil section using conditional sampling technique. *Journal of Fluids Engineering* **111** (2), 204–210.

Kunz, R.F., Boger, D.A., Stinebring, D.R., Chyczewski, T.S., Lindau, J.W., Gibeling, H.J., Venkateswaran, S. & Govindan, T.R. 2000 A preconditioned Navier-Stokes method for two-phase flows with application to cavitation prediction. *Computers & Fluids* **29**, 849–875.

Laberteaux, K. R. & Ceccio, S. L. 2001 Partial cavity flows. part 1. cavities forming onmodels without spanwise variation. *Journal of Fluid Mechanics* **431**, 1–41.

Lakehal, D., Smith, B. L. & Milelli, M. 2002 Large-eddy simulation of bubbly turbulent shear flows. *Journal of Turbulence* **3**, N25.

de Lange, D.K. 1996 Observation and modelling of cloud formation behind a sheet cavity. PhD thesis, University of Twente.

de Lange, D. & de Bruin, G. 1997 Sheet cavitation and cloud cavitation. *Flow, Turbulence and Combustion* **58**, 91–114.

de Lange, D.F., de Bruin, G.J. & van Wijngaarden, L. 1994 *Bubble Dynamics and Interface Phenomena. Fluid Mechanics and Its Applications*, , vol. 23, chap. Observations of cloud cavitation on a stationary 2D profile, pp. 241–246. Springer.

Le, Q., Franc, J-P & Michel, J-M. 1993*a* Partial cavities: Global behavior and mean pressure distribution. *Journal of Fluids Engineering* **115** (2), 243–248.

Le, Q., Franc, J-P & Michel, J-M. 1993*b* Partial cavities: Pressure pulse distribution around cavity closure. *Journal of Fluids Engineering* **115** (2), 249–254.

Lindau, J.W., Kunz, R.F., Boger, D.A., Stinebring, D.R. & Gibeling, H.J. 2002 High Reynolds number, unsteady, multiphase CFD modeling of cavitating flows. *Journal of Fluids Engineering* **124**.

Liu, Y., Fan, H., Wu, D., Chen, H., Feng, K., Zhao, C. & Wu, D. 2020 Experimental investigation of the dynamic cavitation behavior and wall static pressure characteristics through convergence-divergence Venturis with various divergence angles. *Nature - Scientific Reports* **10** (14172).

Long, X., Cheng, H., Ji, B., Arndt, R.E.A. & Peng, X. 2018 Large eddy simulation and Euler-Lagrangian coupling investigation of the transient cavitating turbulent flow around a twisted hydrofoil. *International Journal of Multiphase Flow* **100**, 41–56.

Lund, T.S., Wu, X. & Squires, K.D. 1998 Generation of turbulent inflow data for spatially-developing boundary layer simulations. *Journal of Computational Physics* **140** (2), 233–258.

Menter, F.R. & Kuntz, M. 2004 *The Aerodynamics of Heavy Vehicles: Trucks, Buses, and Trains*, , vol. 19, chap. Adaptation of Eddy-Viscosity Turbulence Models to Unsteady Separated Flow Behind Vehicles, pp. 339–352. Springer, Berlin, Heidelberg.

Merkle, C.L., Feng, J.Z. & Buelow, P.E.O. 1998 Computational modeling of the dynamics of sheet cavitation. In *Third International Symposium on Cavitation*. Grenoble, France.

Mockett, C. 2009 A comprehensive study of detached-eddy simulation. PhD thesis, Technischen Universität Berlin.

Orley, F., Trummler, T., Hickel, S., Mihatsch, M. S., Schmidt, S. J. & Adams, N. A. 2015 Large-eddy simulation of cavitating nozzle flow and primary jet break-up. *Physics ofs Fluids* **27** (086101).

Pamies, M., Weiss, P-E., Garnier, E., Deck, S. & Sagaut, P. 2009 Generation of synthetic turbulent inflow data for large eddy simulation of spatially evolving wall-bounded flows. *Physics of Fluids* **21**, 045103.

Park, S. & Rhee, S.H. 2013 Numerical analysis of the three-dimensional cloudcavitating flow around a twisted hydrofoil. *Fluid Dynamics Research* **45**, 015502.

Peng, X.X., Ji, Bin, Cao, Yantao, Xu, Lianghao, Zhang, Guoping, Luo, Xianwu & Long, Xinping 2016 Combined experimental observation and numerical simulation of the cloud cavitation with U-type flow structures on hydrofoils. *International Journal of Multiphase Flow* **79**, 10–22.

Pipp, P., Hocevar, M. & Dular, M. 2021 Numerical insight into the kelvin-helmholtz instability appearance in cavitating flow. *Applied Sciences* **11**, 2644.

Podbevsek, D., Petkovsek, M., Ohl, C.D. & Dular, M. 2021 Kelvin-helmholtz instability governs the cavitation cloud shedding in Venturi microchannel. *International Journal of Multiphase Flow* .

Prothin, S., Billard, J.-Y. & Djeridi, H. 2016 Image processing using proper orthogonal and dynamic mode decompositions for the study of cavitation developing on a NACA0015 foil. *Experiments in Fluids* **57** (10), 157–182.

Reboud, J-L., Stutz, B. & Coutier, O. 1998*a* Two-phase flow structure of cavitation: experiment and modelling of unsteady effects. In *3rd International Symposium on Cavitation CAV1998*. Grenoble, France.

Reboud, J-L., Stutz, B. & Coutier, O. 1998*b* Two-phase flow structure of cavitation: experiment and modelling of unsteady effects. In *3rd International Symposium on Cavitation CAV1998*. Grenoble, France.

Reisman, G.E., Wang, Y.-C. & Brennen, C.E. 1998 Observations of shock waves in cloud cavitation. *Journal of Fluids Mechanics* **355**, 255–283.

Renard, N. & Deck, S. 2015 Improvements in zonal detached eddy simulation for wall modeled large eddy simulation. *AIAA Journal* **53** (11).

Rist, U. & Maucher, U. 2002 Investigations of time-growing instabilities in laminar separation bubbles. *European Journal of Mechanics B/Fluids* **21**, 495–509.

Sagaut, P., Deck, S. & Terracol, M. 2013 *Multiscale and Multiresolution Approaches in Turbulence - LES, DES and Hybrid RANS/LES Methods: Applications and Guidelines*. Imperial College Press.

Saito, Y., Takami, R., Nakamori, I. & Ikohagi, T. 2007 Dynamic behaviors of re-entrant jet and cavity shedding during transitional cavity oscillation on NACA0015 hydrofoil. *Computational Mechanics volume* **40** (85).

Saurel, R., Boivin, P. & Metayer, O. Le 2016 A general formulation for cavitating, boiling and evaporating flows. *Computers and Fluids* **128**, 53–64.

Saurel, R., Petitpas, F. & Abgrall, R. 2008 Modelling phase transition in metastable liquids: Application to cavitating and flashing flows. *Journal of Fluid Mechanics* **607**, 313–350.

Schmidt, Oliver T. & Colonius, Tim 2020 Guide to spectral proper orthogonal decomposition. *AIAA Journal* **58** (3).

Schnerr, G.H. & Sauer, J. 2001 Physical and numerical modeling of unsteady cavitation dynamics. In *4th International Conference on Multiphase Flow ICMF01*. New Orleans, USA.

Schnerr, G.H., Sezal, I.H. & Schmidt, S.J. 2008 Numerical investigation of three-dimensional cloud cavitationwith special emphasis on collapse induced shock dynamics. *Physics of Fluids* **20**, 040703.

Sedlar, M., Ji, B., Kratky, T., Rebok, T. & Huzlik, R. 2016 Numerical and experimental investigation of three-dimensional cavitating flow around the straight NACA2412 hydrofoil. *Ocean Engineering* **123**, 357–382.

Senocak, I. & Shyy, W. 2004 Interfacial dynamics-based modelling of turbulent cavitating flows, part-1: Model development and steady-state computations. *International Journal for Numerical Methods in Fluids* **44**, 975–995.

Shin, Byeong Rog, Yamamoto, Satoru & Yuan, Xin 2004 Application of preconditioning method to gas-liquid two-phase flow computations. *Journal of Fluids Engineering* **126**.

Singhal, A.K., Athavale, M.M., Li, H. & Jiang, Y. 2002 Mathematical basis and validation of the full cavitation model. *Journal of Fluids Engineering* **124**, 617–624.

Smith, B.R. 1990 The k-kl turbulence model and wall layer model for compressible flows. In *AIM 21st Fluid Dynamics, Plasma Dynamics and Lasers Conference*, , vol. 1483. American Institute of Acronautics and Astronautics, Seattle.

Smith, B. R. 1994 A near wall model for the k-l two equation turbulence model. In *25th AlAA Fluid Dynamics Conference*. American Institute of Aeronautics and Astronautics.

Spalart, P.R. & Allmaras, S.R. 1992 A one-equation turbulence model for aerodynamic flows. In *AIAA 92–0439,* 30th *Aerospace Sciences Meeting – Reno, Nevada.*

Spalart, P.R. & Allmaras, S.R. 1994 A one-equation turbulence model for aerodynamic flows. *La Recherche Aérospatiale* pp. 5–21.

Spalart, P. R. 2000 Strategies for turbulence modelling and simulations. *International Journal of Heat and Fluid Flow* **21**, 252–263.

Spalart, P. R., Deck, S., Shur, M. L., Squires, K. D., Strelets, M. Kh. & Travin, A. 2006 A new version of detached-eddy simulation, resistant to ambiguous grid densities. *Theoretical and Computational Fluid Dynamics* **20**, 181–195.

Spalart, P. R., Jou, W-H, Strelets, M. & Allmaras, S. R. 1997 Comments on the feasibility of les for wings, and on a hybrid rans/les approach. In *Advances in DNS/LES* (ed. C. Liu & Z. Liu), pp. 137–147. Columbus: Greyden Press.

Spiteri, R. J. & Ruuth, S. J. 2002 A new class of optimal high-order strong-stability-preserving time discretization methods. *SIAM Journal on Numerical Analysis* **40** (2), 469–491.

Stanley, C., Barber, T., Milton, B. & Rosengarten, G. 2011 Periodic cavitation shedding in a cylindrical orifice. *Experiments in Fluids* **51**, 1189–1200.

Stanley, C., Barber, T. & Rosengarten, G. 2014 Re-entrant jet mechanism for periodic cavitation shedding in a cylindrical orifice. *International Journal of Heat and Fluid Flow* **50**, 169–176.

Stich, G.-D., Housman, J.A., Kocheemoolayil, J.G., Barad, M.F. & Kiris, C.C. 2018 Application of Lattice Boltzmann and Navier-Stokes methods to NASA's wall mounted hump. In *AIAA 2018-3855*. American Institute of Aeronautics and Astronautics.

Strelets, M. 2001 Detached eddy simulation of massively separated flows. In *39th AIAA Aerospace Sciences Meeting and Exhibit*. American Institute of Aeronautics & Astronautics, Reno.

Stutz, B. & Reboud, J. L. 1997 Experiments on unsteady cavitation. *Experiments in Fluids* **22** (3), 191–198.

Sun, T., Wang, Z., Zou, L. & Wang, H. 2020 Numerical investigation of positive effects of ventilated cavitation around a NACA66 hydrofoil. *Ocean Engineering* **197**, 106831.

Sun, T., Zhang, X., Xu, C., Zhang, G. & Jiang, S. 2019*a* Numerical modeling and simulation of the shedding mechanism and vortex structures at the development stage of ventilated partial cavitating flows. *European Journal of Mechanics/B Fluids* **76**, 223–232.

Sun, T., Zhang, X., Xu, C., Zhang, G., Wang, C. & Zong, Z. 2019*b* Experimental investigation on the cavity evolution and dynamics with special emphasis on the development stage of ventilated partial cavitating flow. *Ocean Engineering* **187**, 106140.

Timoshevskiy, M.V., Churkin, S.A., Kravtsova, A.Y., Pervunin, K.S., Markovich, D.M. & Hanjalic, K. 2016 Cavitating flow around a scaled-down model of guide vanes of a high-pressure turbine. *International Journal of Multiphase Flow* **78**, 75–87.

Towne, A., Schmidt, O. T. & Colonius, T. 2018 Spectral proper orthogonal decomposition and its relationship to dynamic mode decomposition and resolvent analysis. *Journal of Fluid Mechanics* **847**, 821–867.

Trummler, T., Rahn, D., Schmidt, S.J. & Adams, N.A. 2021 Large eddy simulations of cavitating flow in a step nozzle with injection into gas. *Atomization and Sprays* .

Trummler, T., Schmidt, S. J. & Adams, N. A. 2020 Investigation of condensation shocks and re-entrant jet dynamics in a cavitating nozzle flow by large-eddy simulation. *International Journal of Multiphase Flow* .

Turkel, E. 1987 Preconditioned methods for solving the incompressible and low speed compressible equations. *Journal of Computational Physics* **72** (2), 277–298.

Vaquero, J., Renard, N. & Deck, S. 2021 Assessment of zdes for wmles of turbulent boundary layers with pressure gradient and mild flow separation. In *AIAA SCITECH 2021*. United States.

Vreman, Bert, Geurts, Bernard & Kuerten, Hans 1995 A priori tests of large eddy simulation of the compressible plane mixing layer. *Journal of engineering mathematics* **29** (4), 299–327.

Wallis, G. 1967 One-dimensional two-phase flow. New York: McGraw-Hill.

Watanabe, S., Tsujimoto, Y. & Furukawa, A. 2001 Theoretical analysis of transitional and partial cavity instabilities. *Journal of Fluids Engineering* **123** (3), 692–697.

Wu, J., Ganesh, H. & Ceccio, S. 2019 Multimodal partial cavity shedding on a two-dimensional hydrofoil and its relation to the presence of bubbly shocks. *Experiments in Fluids* **60** (66).

Yoshizawa, A. & Horiuti, K. 1985 A statistically derived subgrid scale kinetic model for the large-eddy simulation of turbulent flows. *Journal of Physical Society of Japan* **54** (8), 2834–2839.

Zhang, X.-L., Ge, M.-M., Zhang, G.-J. & Coutier-Delgosha, O. 2021 Compressible effects modeling for turbulent cavitating flow in a small Venturi channel: An empirical turbulent eddy viscosity correction. *Physics of Fluids* **33**, 035148.

Zhou, L. & Wang, Z. 2008 Numerical simulation of cavitation around a hydrofoil and evaluation of a rng k-epsilon model. *Journal of Fluids Engineering* **130** (1), 011302.

Zwart, P.J., Gerber, A.G. & Belamri, T. 2004 A two-phase flow model for predicting cavitation dynamics. In *CMF 2004 International Conference on Multiphase Flow*.

Camille GOUIN

Numerical investigation of sheet cavitation dynamics on a Venturi configuration

Résumé : Le présent manuscrit de thèse propose une étude de la dynamique de poche de cavitation par la réalisation de simulations numériques. La cavitation est un phénomène qui apparaît dans de nombreuses applications et peut entraîner des problèmes conséquents tels que la détérioration des matériaux, une baisse de rendements ou encore la génération de bruits. Un certain nombre de caractéristiques importantes de l'écoulement, telles que la topologie complexe de la poche de vapeur ainsi que sa dynamique, nécessitent d'être étudiées minutieusement. C'est pourquoi, la dynamique de l'écoulement cavitant, observée dans la géométrie d'un Venturi 3-D, et ses interactions avec les parois latérales sont étudiées numériquement. Dans un premier temps, une validation du code est proposée à partir de cas non-cavitant et cavitant. Puis, des simulations sont conduites en utilisant un solveur mono-fluide compressible de type RANS associé à un modèle non linéaire de turbulence ainsi qu'une équation de transport du taux de présence de la phase vapeur. Une analyse détaillée de l'écoulement cavitant est menée à partir d'outils innovants tels qu'une SPOD (*spectral proper orthogonal decomposition*). Une attention particulière est apportée à l'étude des effets tridimensionnels en comparant les résultats de calculs menés avec et sans parois latérales. Une dynamique tridimensionnelle de la poche de cavitation, non reliée à la présence de parois latérales, est identifiée. Son lien avec les mécanismes fondamentaux impliqués dans la cavitation par poche est discuté.
Par la suite, plusieurs méthodes hybrides RANS/LES sont étudiées sur un cas non cavitant possédant une configuration se rapprochant de celle du Venturi. Cette étude a pour but de sélectionner la méthode hybride RANS/LES la plus adéquate à la simulation de la cavitation par poches.

Mots clés : cavitation, modèle RANS, modèle RANS/LES, mélange 1-fluide, écoulement compressible, SPOD

Abstract : The present PhD thesis aims at studying sheet cavitation dynamics by carrying out numerical simulations. This phenomenon appears in many hydraulic applications and can lead to technical issues, such as material degradations, performance reduction or noise generation. Some significant outcomes, such as the complex topology of three-dimensional cavitation pockets and their associated dynamics, need to be carefully visited. Therefore, the dynamics of partial cavitation developing in a 3-D Venturi geometry and the interaction with sidewalls are numerically investigated. In the first instance, software validation is proposed on non-cavitating and cavitating cases. Then, simulations are performed using a one-fluid compressible Reynolds-Averaged Navier–Stokes (RANS) solver associated with a non-linear turbulence model and a void ratio transport-equation model. A detailed analysis of this cavitating flow is carried out using innovative tools such as Spectral Proper Orthogonal Decompositions (SPOD). Particular attention is paid to the study of 3-D effects by comparing numerical results obtained with sidewalls and periodic conditions. A three-dimensional dynamics of the sheet cavitation, unrelated to the presence of sidewalls, is identified. The link between the mechanisms involved in sheet cavitation, such as the re-entrant jet and the vapour pocket behaviour, is discussed. The effects of the cavity dynamics on the flow are also identified.
Thereafter, a range of Hybrid RANS/LES methods is investigated on a non-cavitating case with a similar configuration to the cavitating Venturi flow one. This study intends to select an acceptable hybrid RANS/LES method for sheet cavitation simulation using a better-resolved approach.

Keywords : cavitation, RANS model, RANS/LES model, 1-fluid mixture, compressible flow, SPOD